Infrared ellipsometry on mixed functional polymer brushes designed to control surface characteristics

vorgelegt von
M. Sc. Chemie
Annika Kroning
geb. in Diepholz

von der Fakultät II – Mathematik und Naturwissenschaften
der Technischen Universität Berlin
zur Erlangung des akademischen Grades

Doktor der Naturwissenschaften
- Dr. rer. nat -

genehmigte Dissertation

Promotionsausschuss:

Vorsitzender: Prof. Dr. Peter Hildebrandt
Gutachter: Prof. Dr. Norbert Esser
Gutachter: PD Dr. Karsten Hinrichs
Gutachter: Prof. Dr. Klaus Rademann

Tag der wissenschaftlichen Aussprache: 29.08.2017

Berlin 2017

List of publications

- A. Kroning, A. Furchner, D. Aulich, E. Bittrich, S. Rauch, P. Uhlmann, K.-J. Eichhorn, M. Seeber, I. Luzinov, S. M. Kilbey II, B. S. Lokitz, S. Minko, K. Hinrichs, "In Situ Infrared Ellipsometry for Protein Adsorption Studies on Ultrathin Smart Polymer Brushes in Aqueous Environment", *ACS Applied Materials & Interfaces* **2015**, *7*, 12430–12439. doi: 10.1021/am5075997

- A. Kroning, A. Furchner, S. Adam, P. Uhlmann, K. Hinrichs, "Probing carbonyl–water hydrogen bond interactions in thin polyoxazoline brushes", *Biointerphases* **2016**, *11* (1), 019005. doi: 10.1116/1.4939249

- A. Furchner, A. Kroning, S. Rauch, P. Uhlmann, K.-J. Eichhorn, K. Hinrichs, "Molecular Interactions and Hydration States of Ultrathin Functional Films at the Solid–Liquid Interface", *Analytical Chemistry* **2017**, *89* (6), 3240–3244. doi: 10.1021/acs.analchem.7b00208

List of contributions at academic conferences and meetings

- A. Furchner, A. Kroning, E. Bittrich, S. Rauch, M. König, P. Uhlmann, K.-J. Eichhorn, K. Hinrichs, "Studies on the Swelling Behavior of Thin Polymer Brush Films with In Situ Infrared Spectroscopic Ellipsometry", Poster presentation on the **245th ACS National Meeting**, PMSE (Polymeric Materials: Science and Engineering), April 7–11, 2013, New Orleans, USA.

- A. Kroning, A. Furchner, M. Seeber, I. Luzinov, K. Hinrichs, "IR spectroscopy on mixed functional polymer interfaces to characterize their switching behavior", Poster presentation at the **Forschungsforum Adlershof**, November 12, 2013, Berlin-Adlershof, Germany.

- A. Kroning, A. Furchner, M. Seeber, I. Luzinov, K. Hinrichs, "In Situ Infrared Spectroscopic Ellipsometry on Temperature-Responsive Copolymer Brushes", Poster presentation on the **8th Workshop Ellipsometry**, March 10–12, 2014, Dresden, Germany.

- A. Kroning, A. Furchner, M. Seeber, I. Luzinov, S. Minko, K. Hinrichs, "Poly(*N*-isopropyl acrylamide) in mixed polymer brushes: Temperature-responsive behavior studied with infrared spectroscopy" Poster presentation on the **248th ACS National Meeting**, PMSE (Polymeric Materials: Science and Engineering), August 10–14, 2014, San Francisco, USA.

- A. Kroning, A. Furchner, M. Seeber, I. Luzinov, S. Minko, S. M. Kilbey II, B. S. Lokitz, K. Hinrichs, "Temperature-responsive behavior of poly(*N*-isopropyl acrylamide) in mixed polymer brushes studied with in-situ infrared ellipsometry", Poster presentation at the **Forschungsforum Adlershof**, November 11, 2014, Berlin-Adlershof, Germany.

- A. Kroning, A. Furchner, E. Bittrich, M. Seeber, I. Luzinov, S. M. Kilbey II, B. S. Lokitz, O. Trotsenko, S. Minko, K. Hinrichs, "In-situ infrared ellipsometric studies on temperature-responsive polymer brushes", Poster presentation on the **9th Workshop Ellipsometry**, February 23–25, 2015, Twente, Netherlands.

- A. Kroning, A. Furchner, M. Seeber, I. Luzinov, S. M. Kilbey II, B. S. Lokitz, O. Trotsenko, S. Minko, K. Hinrichs, "In-situ infrared ellipsometric studies on the thermoresponsive behavior of copolymer brushes and their interaction with proteins", Oral presentation at the **E-MRS Spring Meeting**, May 11–15, 2015, Lille, France.

To my running shoes...

Contents

List of Figures

List of Tables

List of Abbreviations and Symbols

AFM	Atomic Force Microscopy
AR-XPS	Angle-Resolved X-ray Photon Spectroscopy
copolymer10	poly(2-(methyl-[stat]-cyclopropyl)-2-oxazoline) with 10% MeOx
copolymer25	poly(2-(methyl-[stat]-cyclopropyl)-2-oxazoline) with 25% MeOx
*c*PrOx	2-cyclopropyl-2-oxazoline
CROP	Cationic Ring-Opening Polymerization
$\vec{D}$	dielectric displacement
d(dry)	dry layer thickness
d(T)	swollen layer thickness at temperature T
$\vec{E}$	electric field
EMA	effective medium approximation
EsterOx	methyl-3-(oxazol-2-yl) propionate
f_i	volume fraction of substance i
FIB	fibrinogen
GMA	glycidyl methacrylate
h	layer thickness (brush height)
H-bond	hydrogen bond
IPF	Leibniz-Institut für Polymerforschung
IR	infrared
IR-SE	Infrared Spectroscopic Ellipsometry
k	absorption coefficient
LCST	lower critical solution temperature
meas	measured
MEK	methyl ether ketone
MeOx	2-methyl-2-oxazoline
n	real refractive index
N	complex refractive index
N_A	Avogadro's number (6.022 x 10^{23} mol^{-1})
NIPAAm	N-isopropyl acrylamide
ORNL	Oak Ridge National Laboratory
PAA	poly(acrylic acid)
P*c*PrOx	poly(2-cyclopropyl-2-oxazoline)
PEEK	polyether ether ketone
PEtOx	poly(2-ethyl-2-oxazoline)
PGMA	poly(glycidyl methacrylate)
PID controller	proportional-integral-derivative controller
P*i*PrOx	poly(2-isopropyl-2-oxazoline)
PMeOx	poly(2-methyl-2-oxazoline)
PNI-40	PNIPAAm-*b*-PGMA copolymer brush with 40.8% PNIPAAm content

PNI-70	PNIPAAm-*b*-PGMA copolymer brush with 70.6% PNIPAAm content
PNIPAAm	poly(*N*-isopropylacrylamide)
PNIPAAm-*b*-PGMA	[Poly(*N*-isopropylacrylamide)]-*block*-[poly(glycidyl methacrylate)]
POx	poly(2-alkyl-2-oxazoline)
QNM^{TM}	quantitative nanomechanical mapping
R	reflectance
RAFT	reversible addition fragmentaion chain transfer
ref	reference
rms	root mean square
$r_{p,s}$	reflection coefficient in p- and s-polarization
sim	simulated
STM	scanning tunneling microscope
T_{cp}	cloud point temperature
$t_{p,s}$	transmission coefficient in p- and s-polarization
UCST	upper critical solution temperature
VIS	visible
XPS	X-ray Photoelectron Spectroscopy
Γ	surface coverage
$\delta_{p,s}$	phase of p- and s-polarization
ϵ	dielectric function
λ	wavelength
ρ	complex reflectance ratio
ϱ	polymer bulk density
σ	grafting density
ϕ_0	angle of incidence
ϕ_B	Brewster angle
ω	frequency

Chapter 1

Introduction

Materials science on the nanoscale has become very important in the past decades. With surfaces and interfaces being the central area where electric, catalytic or biological processes take place, a suitable modification of these interfaces is of great value. The surface properties of a material can be modified by coating it with a thin layer without altering its bulk properties. An example for biological applications of such coatings are antifouling layers on medical implants [1, 2]. Other applications are thin layers not to *protect* a material from interaction with its environment but to *induce* a special interaction, e. g. antibody recognition, controlled protein adsorption, or cell adhesion/detachment and proliferation [3–9].

This thesis focuses on such special interactions. It is part of a joint DFG-NSF project with partners from the USA and Germany within the materials world network called "Switchable polymer interfaces for bottom-up stimulation of mammalian cells“. The long-term goal of the project is to design a material that can be used for the controlled attachment, proliferation, and detachment of cells. Functional polymer films are suitable coatings for these applications, because of their biocompatibility and chemical stability. Their functionality is based on an external stimulus, for example a variation of pH value [10–12], salinity [12, 13], temperature [14–17], or magnetic field [18, 19], that induces a profound change of surface properties of the film. Using temperature as stimulus is very useful for the design of bioactive surfaces, since biological samples are very sensitive to changes in pH or ion concentrations [20]. The polymers poly(*N*-isopropyl acrylamide) [PNIPAAm] and poly(2-alkyl-2-oxazoline)s [POx] are such temperature-responsive polymers, which is why they were studied in this work.

The polymers were used as a special kind of nanometer-thin functional coating, called polymer brushes. Such brushes consist of polymers densely grafted to a substrate at one chain end, resulting in a thin layer of chains protruding from the surface like bristles on a brush [21, 22]. Due to the high grafting density the polymer chains are in close contact and forced to unidirectionally stretch away from the substrate. By that a uniform responsive behavior upon application of the stimulus is achieved [23].

PNIPAAm is a widely studied polymer with temperature-responsive behavior [24–29]. It is hydrophilic and undergoes a transition to a more hydrophobic state in water when the temperature is raised. The temperature around which this transition takes place is called lower critical solution temperature (LCST). The other polymer class studied in this work are POx. They show temperature-responsive behavior when the alkyl side group is an ethyl ($–C_2H_5$) or propyl ($–C_3H_7$) group [17, 30–33]. Both PNIPAAm and POx contain amide groups that can interact with water via hydrogen bonds. The current work focuses on the temperature-responsive switching behavior of PNIPAAm and POx between a hydrophilic and a hydrophobic state. The characterization is done by probing the solid–liquid interface in situ to examine the interactions between the polymer's functional groups and water molecules. Since the functional behavior could

possibly enable controlled attachment and detachment of proteins or cells, which is the overall goal of the project, protein adsorption experiments were also performed on some of the brushes.

Studying the interface between a material and its environment means being sensitive to the interface or a thin layer at the interface, ideally without disturbing the nature of the layer. Ellipsometry is such a surface-sensitive and non-destructive method [34–37]. It is an optical technique providing valuable information about a material via the reflection of polarized light at the interface of interest. This can be done without the need of a label like isotopes or fluorescencent markers [38]. Measurement of organic materials is often done with infrared (IR) light, since the spectral features are correlated with molecular vibrations. The frequency of a vibration is characteristic for molecular bonds and functional groups, therefore it is useful for a qualitative analysis. Infrared spectroscopic ellipsometry (IR-SE) delivers absolute spectra that allow for identification of spectral changes due to changes of interaction or aging [39–41].

Because of these advantages, in situ IR-SE was chosen to study the polymer brushes in aqueous solution. An in situ cell was utilized that enables to probe the brush layer while it is in contact with solution [10, 42]. We were interested in the in situ behavior of polymer brushes of PNIPAAm and POx upon application of the stimuli as well as their interaction with biological macromolecules. IR-SE spectra of these brushes were mainly evaluated qualitatively. Optical modeling was applied to extract semi-quantitative information about the optical characteristics of the layers in different states. Also, simulations of some IR bands that contain several components have been performed. Our aim was to interpret the ellipsometric spectra with respect to the interactions within the polymer brushes themselves as well as the interactions between polymer and solution.

The two polymers PNIPAAm and POx were chosen, because both are temperature-responsive with an LCST in the physiologically relevant temperature range. Based on these polymers, two different brush systems have been prepared: On the one hand, POx brushes were studied. The POx polymer chains used for brush preparation contained two different alkyl side chains, either in their pure form or as statistical copolymers containing both types of side chain. Copolymerization shifted the LCST of POx into the same temperature range as the LCST of PNIPAAm, and therefore it was possible to compare the switching behavior of POx and PNIPAAm brushes. On the other hand, PNIPAAm brushes were prepared by a modified grafting-to procedure using a block-copolymer of PNIPAAm and the anchoring polymer PGMA. Our measurements were focused on the switching behavior of these block-copolymer brushes, their interaction with proteins, and comparison to the traditionally prepared PNIPAAm brushes. PNIPAAm has been reported protein-repellent in many cases [7, 43–46] and previous studies in our group have shown the same behavior [47]. PGMA on the other hand has a high affinity to proteins [48], so we used this different polymer–protein interaction in protein adsorption experiments as inidcator for the presence of PGMA blocks at the brush surface.

This thesis is structured as follows: First, an introduction to functional polymer brushes, particularly temperature-responsive ones, is given in chapter 2. In chapter 3 the theoretical background about optics and its use in ellipsometry is explained. The setup of the IR-SE instrument is described, including the special case of in situ measurements. Sample preparation will be described in chapter 4 which is divided into two sections. First, the preparation of the two kinds of polymer brushes is described. Grafting of the

block-copolymer brushes was done on a research visit to the group of Igor Luzinov at Clemson University, USA. The preparation of polyoxazoline brushes included polymer synthesis and was done by Stefan Adam at IPF in Dresden. The second section of the chapter deals with the data analysis. It contains the spectral correction as well as the use of layer modeling to extract optical constants and quantitative data from the measurements.

Chapter 5 is about the results of this work. It contains three sections: The first two sections are about the block-copolymer brushes and POx. They each describe a characterization of the brushes in dry state followed by the in situ swelling experiments in aqueous solution. The switching behavior was evalutated mainly with IR-SE but also complementary methods like visible ellipsometry (VIS-SE) and atomic force microscopy (AFM) were used. Finally, the interaction of polymer brushes with proteins is adressed in the third section. Adsorption experiments with the protein fibrinogen were conducted on the block copolymer brushes containing PNIPAAm. The results were compared to findings on the interaction between proteins and PNIPAAm from previous experiments in our group as well as from literature. A summary of the work is given at the end, including a short outlook on future possibilities.

Chapter 2

Functional Polymer Brushes

2.1 General Properties

Functional organic interfaces are promising systems for a wide variety of biological and medical applications [3]. They can be useful in drug delivery, as synthetic membranes, biosensors, or as biomimetic surfaces to control e. g. protein adsorption and cell growth [4, 7, 49–52].

Polymers are ideal candidates in this matter, because they can be designed according to a desired function. There are many biocompatible, non-toxic polymers available that exhibit functional behavior. Their functionality relies on a change in the environment (external stimulus), inducing a change of the polymer properties [4]. Several different environmental changes can induce such functional behavior, depending on the chemical structure of the polymer. For example, a change of pH triggers the response of polyelectrolytes, e.g. poly(acrylic acid) [PAA] (figure 2.1b), that change between a charged and a less charged or neutral state [10]. Another example is a change of temperature or solvent that can induce the response in uncharged polymers because it relies on hydrophobic/hydrophilic interactions between polymer and solvent [29, 53–55]. The temperature-responsive transition takes place around the critical solution temperature. A transformation from hydrophobic to hydrophilic at increasing temperature is called upper critical solution temperature (UCST), while the opposite behavior—from hydrophilic to hydrophobic—is called lower critical solution temperature (LCST) [26]. The latter is the case for the two polymers studied in this work, PNIPAAm and POx. The LCST of PNIPAAm (figure 2.1c) takes place around 31 °C [24]. Free PNIPAAm chains in aqueous solution transform from an extended coil below the LCST to a globule above the LCST followed by aggregation and phase separation. Thin PNIPAAm layers such as brushes respond in a cumulative way to the stimulus due to strong interaction with each other. They switch from a highly swollen to a collapsed state.

POx (figure 2.1d) is another temperature-responsive polymer with LCST behavior, that has recently been used to fabricate biocompatible switchable surfaces [17, 56]. Both PNIPAAm and POx have been of interest as potential alternatives to poly(ethylene glycol) [PEG] [54, 57]. PEG is being commercially used due to its biocompatibility and antifouling characteristics, but has been reported to be sensitive towards oxidation [2, 57–59].

Preparation of polymer brushes depends on the substrate as well as the desired brush architecture. On gold they can be readily prepared via the reaction of thiol end groups of polymer chains with the gold surface [4]. Gold is a highly reflective substrate, which is an advantage in ellipsometry to obtain a good signal-to-noise ratio. However, in situ IR-SE measurements require to direct the IR beam through the substrate, because the penetration depth of IR light in water is too low. Unfortunately, gold is not transparent

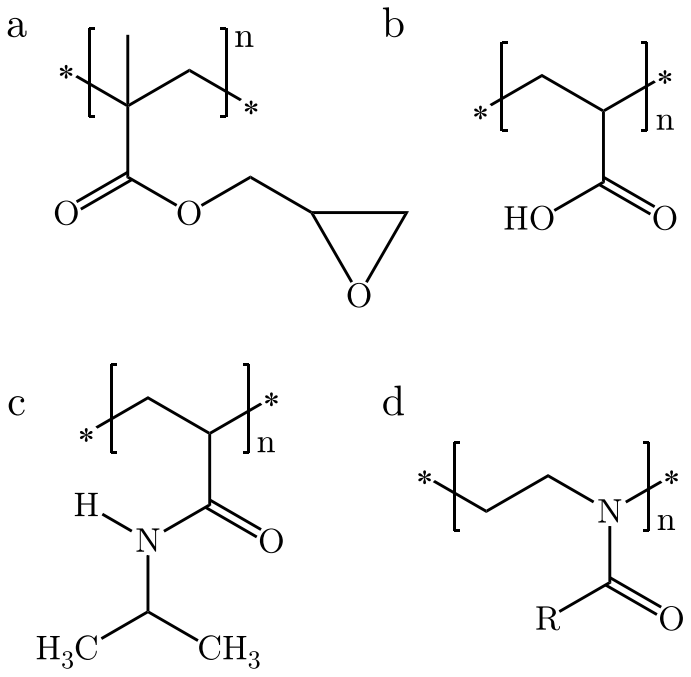

FIGURE 2.1: Structures of the anchoring polymer PGMA (a) and the polymers PAA (b), PNIPAAm (c), and POx (d) used to fabricate polymer brushes.

in the IR and therefore it can not be used as substrate. However, for reference layers, that are prepared to evaluate the dry state bands of the polymers, gold served as a well-defined and highly reflecting substrate.

Undoped silicon is IR transparent and therefore suitable for in situ IR-SE measurements. In this case, an anchoring layer is needed to graft the brush polymer to the substrate. This anchoring layer can form covalent bonds both with the surface as well as the polymer. It can be either a (self-assembled) monolayer or a thin layer of a polymer with reactive end groups. Poly(glycidyl methacrylate) [PGMA] (figure 2.1a) is a suitable anchoring polymer that has been used in our studies. It contains epoxy groups in the side chains that can react with e. g. –OH, –COOH, and $–NH_2$ groups. Attachment of PGMA to silicon takes place via thermal reaction of the epoxy groups with silanol groups on the activated silicon surface. After this reaction there is still a sufficient number of epoxy groups present in the layer for the subsequent reaction with polymer chains [60].

The procedure of using pre-formed polymer chains with reactive end groups for brush preparation is called 'grafting-to'. It is a relatively quick and easy procedure. Its main advantage is the possibility to achieve a good reproducibility of thickness and grafting density and the ability to use polymers with known chain length and polydispersity index (PDI). However, the grafting density of this preparation method is fairly low, because diffusion of reactive chain ends to the substrate surface is limited by chains that are already attached. With increasing molecular weight of the polymer the maximum grafting density that can be achieved decreases [61].

Higher grafting densities are possible if the brushes are prepared via the 'grafting-from' method. In this procedure, a thin layer of initiator molecules is attached to the substrate and the polymerization carried out directly on the surface by reaction in a

monomer solution of the desired brush polymer units. With this method higher grafting densities can be achieved and very long chains can be produced, which in turn results in thicker brushes [46, 62]. This procedure is more complicated and the resulting brushes contain chains with an unknown, and probably very high, PDI value. Due to these drawbacks the 'grafting-from' method has not been used for brushes studied in this work.

Although the traditional brushes studied in our group are prepared via 'grafting-to', the synthesis still contains several steps [16, 43]. These include two separate grafting steps of the PGMA anchoring layer and the polymer brush layer. For applications demanding a high-throughput preparation, a faster procedure is advantageous. This could be obtained by using a pre-formed block-copolymer of the anchoring polymer PGMA and the brush polymer. In that way, one-step grafting of the block-copolymer chains onto the silicon substrate is possible, because only PGMA can covalently attach to the silicon surface, while the brush polymer chains remain mobile [63, 64].

2.2 Temperature-responsive brushes

Amongst the possible triggers of smart polymer brushes, temperature is the most interesting one. It has been intensely focused on in the last two decades, in particular for potential biotechnological applications like bioactive surfaces and drug-delivery systems due to its ease of operation [20, 49, 65]. PNIPAAm and POx, the latter with a propyl group in the side chain, are the temperature-responsive polymers used here. They show LCST behavior in the physiological temperature range, being soluble in aqueous solutions at low temperatures and becoming insoluble when the temperature is increased. The responsive behavior is based upon a thermodynamically driven change of polymer–polymer and polymer–water interactions in the form of hydrogen bonds.

Both PNIPAAm and POx are amides, containing a carbonyl group (C=O) next to a nitrogen atom (see figure 2.1 c and d). PNIPAAm is a secondary amide, meaning the nitrogen atom is bonded to two alkyl chains and one hydrogen atom. POx is a tertiary amide, because its nitrogen atom is contained in the polymer backbone at the anchoring point of the side chain. Therefore, in POx the nitrogen atom is bonded to three alkyl groups and there is no $\mathrm{N{-}H}$ group. Characteristic vibrational bands of amide groups are the amide I and amide II, which occur at 1700–1600 $\mathrm{cm^{-1}}$ and 1600–1500 $\mathrm{cm^{-1}}$, respectively. Amide I is contained of about 76% C=O stretching mode and amide II comprises mainly the $\mathrm{N{-}H}$ bending (43%) and $\mathrm{C{-}N}$ stretching (29%) modes [66].

The C=O and $\mathrm{N{-}H}$ groups of amides can take part in hydrogen bonding, either with each other or with polar solvents, for example water. An overview of the possible interactions of PNIPAAm and POx in water is given in figure 2.2. Hydrogen bonding influences the IR frequencies of the amide bands in different ways. The C=O mode in amide I describes a stretching vibration with a high electron density due to the double bond and the two free electron pairs on the oxygen atom. When the oxygen atom takes part in a hydrogen bond, some of this electron density is shifted towards the hydrogen atom, leaving the C=O bond with less electron density and therefore less energy. This results in a lower force constant of the oscillation and a shift of the infrared mode to lower frequencies. Formation of a second hydrogen bond at the same oxygen atom shifts the frequency even more. Calculations reported in literature describe that one hydrogen bond shifts the C=O mode by approximately 20 $\mathrm{cm^{-1}}$ [67, 68]. Amide II on the other hand contains the $\mathrm{C{-}N{-}H}$ bending mode which usually shifts to higher frequencies

when the N−H group takes part in a hydrogen bond. The bond restricts the vibrational bending mode and increases the force constant of the oscillation [28].

With the C−N bond having a small double-bond character due to mesomeric structures (see figure 2.3), the amide group is planar and rotation around the C−N bond is restricted [69, 70]. This limits the mobility of the amide group towards pairing with other amide groups or water molecules for hydrogen bonding. The C−N stretching mode is also sensitive to conformational changes in the main chain, therefore the temperature-responsive switching of amide I can differ from that of amide II [25].

PNIPAAm is a very common and the most widely studied temperature-responsive polymer. Its response in water takes place around 31 °C with an abrupt transition both in solution [24, 71–73] and as a thin film [15, 16, 28, 74]. The C=O and N−H bonds of the amide group can take part in hydrogen bonding with water in the form of C=O $\cdots$ H_2O and N−H $\cdots$ OH_2. In the swollen, strongly hydrated state, this kind of hydrogen bonding (amide–water) dominates, depicted with numbers 3 and 4 in figure 2.2. Above the LCST the brush layer is in its collapsed, less hydrated state. In this state, amide–amide hydrogen bonding in the form of C=O $\cdots$ H−N is increased due to the release of water molecules from the brush (numbers 1 and 2 in figure 2.2) [28, 75]. A C=O group can form two hydrogen bonds with its two free electron pairs, giving rise to several possible combinations of interactions (see figure 2.2). These interactions have different vibrational frequencies and generate several band components in the IR spectra, which overlap within the amide I band.

POx were first synthesized in the 1960s [76–79] but their potential use in surface modification has been explored only recently [17, 56, 80–84]. Their LCST behavior is based on interactions between polymer and water similar to those in PNIPAAm, the main difference between the polymers is that in POx the nitrogen atom of the amide group is part of the polymer backbone (see figures 2.1d and 2.2). As mentioned before, this tertiary amide has no N−H group, thereby POx cannot form C=O $\cdots$ H−N hydrogen bonds. In fact, the C=O groups are the only group within the POx chains that can form hydrogen bonds with water. This results in less possibilities of interactions in POx brushes than in PNIPAAm brushes (see figure 2.2).

The hydrophilicity of POx depends on the specific side-chain chemistry. Different alkyl groups lead to more hydrophilic or more hydrophobic polymers, or to an LCST behavior that is often tunable via parameters like molecular weight. Poly(2-methyl-2-oxazoline) [PMeOx], for example, is hydrophilic but not temperature-responsive, whereas poly(2-*n*-propyl-2-oxazoline) [P*n*PrOx] as well as its isomers are temperature-responsive with a reversible transition from hydrophilic to hydrophobic in a certain temperature range [31, 32, 65, 85]. Additionally, the transition can be tuned via copolymerization with either a more hydrophilic or more hydrophobic oxazoline, thereby increasing or decreasing the LCST, respectively [30, 85].

Many studies on temperature-responsive polyoxazolines include poly(2-isopropyl-2-oxazoline) [P*i*PrOx], the structural isomer of PNIPAAm. With an LCST around 36–39 °C its response is close to body temperature [86, 87]. Katsumoto et al. [32] showed that P*i*PrOx in solution undergoes a gradual reversible dehydration between 20–40 °C. However, a drawback is its irreversible crystallization when the polymer is kept above 40 °C for longer periods of time, inhibiting the switching behavior [86]. Other temperature-responsive polyoxazolines like P*n*PrOx are amorphous, but they have a quite low glass transition temperature ($T_g < 45$°C), which is a disadvantage in sample handling and storage [31, 85].

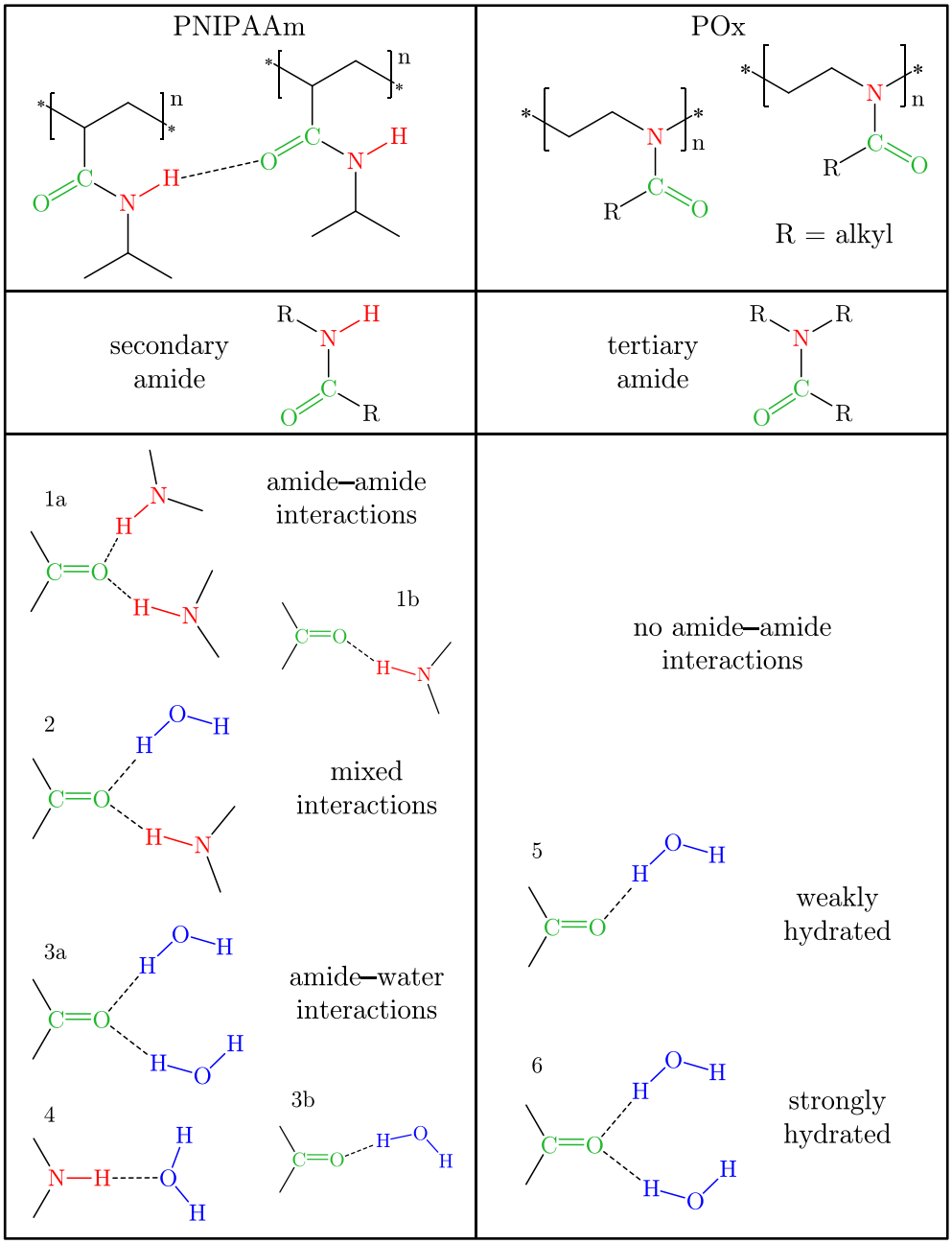

FIGURE 2.2: Scheme of the possible interactions of PNIPAAm (left) and POx (right) in water. The top and middle panels show the chemical structure of the polymers and their classification. Note, that POx with R=isopropyl is a structural isomer of PNIPAAm. The bottom panels illustrate the possible polymer–polymer and polymer–water interactions, with the polymer hydration state increasing from top (dry state) to bottom (fully hydrated).

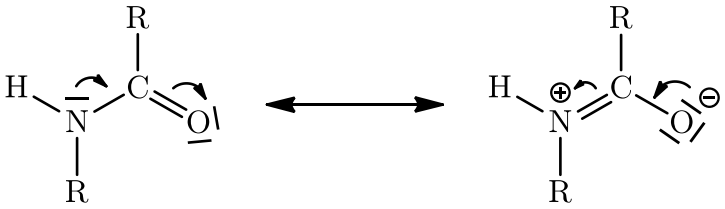

FIGURE 2.3: Mesomeric structures of an amide group. The structure on the right shows the partial double-bond character of the C–N bond, resulting in the H–N–C–O atoms being in the same plane.

For this reason, Bloksma et al. [31] introduced poly(2-cyclopropyl-2-oxazoline) [P*c*PrOx]. It is amorphous and has a sufficiently high glass transition temperature (T_g ~80°C). However, their studies on P*c*PrOx only focus on the polymer chains in solution. For the switching behavior of thin polyoxazoline films or brushes several publications can be found [17, 56, 80, 82, 83], but these only involve non-cyclic polyoxazolines like P*i*PrOx. Therefore polymer brushes of P*c*PrOx were the focus of this project.

In this work, the two different polymers described above, PNIPAAm and POx, were studied as thin layers in the form of brushes. In both cases PGMA was used as anchoring polymer to attach the brush polymer to the silicon substrate.

First, the results on POx brushes with cyclopropyl and methyl groups in the side chain are described: P*c*PrOx is temperature-responsive with an LCST close to room temperature, depending on its molecular weight. PMeOx is hydrophilic and shows no LCST behavior. It is included in the study because two statistical copolymers were prepared from MeOx and *c*PrOx monomers to obtain temperature-dependent POx with increased LCST compared to the pure P*c*PrOx. [17]

Second, PNIPAAm-*block*-PGMA copolymer brushes were characterized and compared to the well-studied 'traditional' PNIPAAm brushes. [16, 43, 45] The aim of these block copolymer brushes was to prepare temperature-responsive PNIPAAm brushes via a procedure with reduced brush preparation steps. The temperature-responsive properties of these brushes were compared to those of traditionally prepared PNIPAAm brushes. According to Joseph et al. [9] the incorporation of PGMA in the PNIPAAm-based brushes lowers the LCST due to an increased hydrophobicity.

Both functional polymers, PNIPAAm and POx, are biocompatible and have been found to be protein-repellent [7, 43–46, 82, 88], therefore they could be suitable alternatives to the widely used bioinert PEG [33, 83, 89]. Thin films of PMeOx have been reported protein-resistant [82] and have also shown a better resistance to oxidative degradation compared to PEG [57], which is important for long-term stability. Concerning protein adsorption on PNIPAAm, some publications present successful adsorption and desorption of proteins on PNIPAAm surfaces, but these results were obtained on brushes with low grafting densities [6, 8] or on a different kind of PNIPAAm layer [90].

Contrary to the brush polymers, the anchoring polymer PGMA has a high affinity towards protein adsorption [48]. This different behavior of PGMA and PNIPAAm towards proteins could be used in this work as indicator for the presence of PGMA sections at the brush–solution interface of PNIPAAm-*b*-PGMA brushes in swollen and collapsed state. For this reason, protein adsorption experiments were performed on these brushes.

Chapter 3

Methods and Experimental Settings

Optical spectroscopy in general is the study of interactions of electromagnetic radiation with matter. For example, spectroscopic measurement techniques are based on measurement of absorption, emission, reflection, or scattering of light. The electromagnetic spectrum spans a wide range, from low-energetic radiowaves to high-energetic X-rays, and can excite very different processes in a material. For example, visible (VIS) and ultraviolet (UV) light excites electronic states in atoms or molecules while the infrared (IR) light excites molecular vibrations. Therefore the respective spectroscopic techniques provide different information about the sample [91].

Spectroscopic Ellipsometry (SE) is a non-invasive optical technique that employs polarized light to characterize surfaces and thin layers. Very common is its application in the UV and VIS ranges due to high intensity light sources, enabling fast measurements down to the level of seconds or milliseconds [34, 36]. Due to its sensitivity to changes in refractive index n and thickness d it is commercially used to examine thin layers and layer stacks, for example in the semiconductor industry [92]. Organic layers often show similar refractive indices in the UV-VIS which results in a low optical contrast between the layers. In these cases, IR radiation is advantageous, as it excites molecular vibrations that show characteristic spectral signals of functional groups and their orientation [93], and thereby results in a high optical contrast when applied to SE. This enables to evaluate the molecular structure, composition, and anisotropy of the material as well as its interactions with the environment. The drawback of lower intensity of IR light sources compared to the VIS range is overcome in FTIR by the use of an interferometer. Every scan of the recorded interferogram contains the full spectral range, thereby no intensity is lost (throughput advantage) and no monochromator is needed (multiplex advantage) [94]. Even though the signal-to-noise ratio is lower than in the UV and VIS ranges, information about molecular interactions provided by IR-SE is highly valuable for the study of organic layers and sensitive biological samples [40]. With the development of in situ setups for ellipsometry the technique has gained increasing attention for studies at the solid–liquid interface. For example, surfaces and thin layers can be probed in contact with liquids under different environmental conditions to evaluate interactions with the liquid, the degree of swelling, and changes in conformation. Additionally, adsorption processes of e.g. proteins and cells can be monitored [38].

Another method to study surfaces or interfaces is AFM. It is a surface scanning technique providing information about the topography and roughness on a sub-nanometer scale. This can be used to examine sample homogeneity and impurities. In some cases it is also applied to determine layer thickness by scanning the edge of a layer.

In this chapter a summary of the above mentioned techniques will be given. The first section deals with the principle of ellipsometry and its use for thin layer characterization. It will be explained which quantities are measured and how they are connected to the sample parameters. This is followed by the arrangement of the instrumental setups for ex situ and in situ measurements, as these differ especially for measurements in the IR. In the second section a brief summary about atomic force microscopy (AFM) is given, which was performed on the brushes both in air and in water as a complementary technique.

3.1 Spectroscopic Ellipsometry

Ellipsometry measures the polarization change of light upon reflection on a sample. It identifies the ellipse of polarized light after interaction with a sample, as shown in figure 3.1, and thus can be classified as a type of polarimetry [37, 95]. Measured parameters in ellipsometry are the amplitude ratio $\tan\Psi$ and phase difference Δ between the s- and p-polarized component of the reflected light. From these values the sample parameters, such as dielectric function and layer thickness, can be determined [93, 96, 97]. The technique is very useful for measurements of thin films. This is due to its surface sensitivity combined with general advantages of being a contact-free, label-free, and non-destructive method [98]. For example, film thickness can be determined via optical modeling with sensitivity down to submonolayer thickness. Additionally ellipsometry offers the possibility to probe surfaces ex situ as well as solid–liquid interfaces in situ, which enables live (on-line) process monitoring [36, 98, 99].

The scheme in figure 3.1 shows the general setup of an ellipsometric measurement and visualization of the polarization properties. Light from the source is directed through a linear polarizer before it hits the sample under an oblique angle of incidence Φ_0. The reflected beam passes through a second polarizer—which is called analyzer—and the intensity is detected.

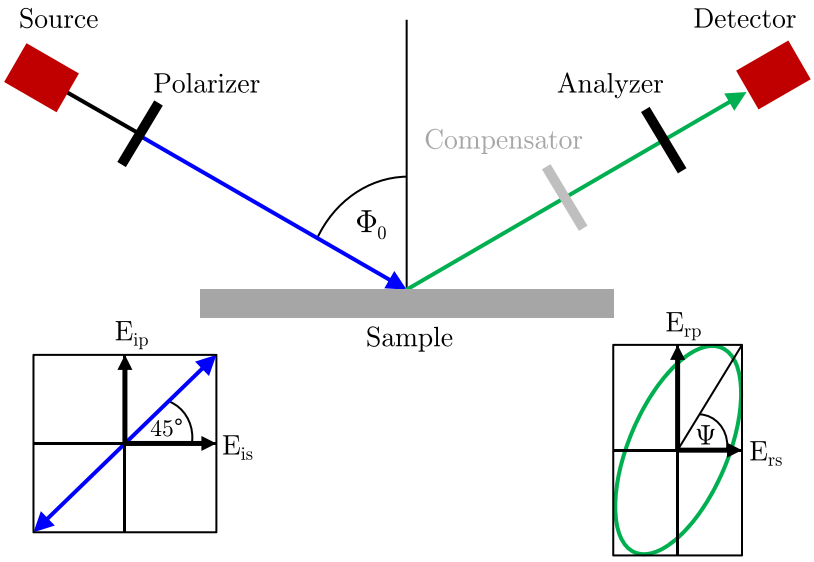

FIGURE 3.1: Scheme of a simple ellipsometric setup with polarizer, sample, analyzer, and optional compensator.

3.1.1 Basic principles

The propagation of electromagnetic radiation and its interaction with matter is described by Maxwell's equations. One relation derived from these equations is the dielectric displacement $\vec{D}$, that describes the dielectric function ϵ of the material acting on the electric field $\vec{E}$ [36, 100].

$$\vec{D} = \epsilon \vec{E} \tag{3.1}$$

The dielectric function is a function of frequency and connected to the complex refractive index N via equation 3.2. Both optical parameters comprised within—the real refractive index n and absorption coefficient k—are also dependent on frequency [92, 97].

$$\begin{aligned} \epsilon &= N^2 \\ \text{with} \quad N &= n + ik \end{aligned} \tag{3.2}$$

In the case of polarized light, the reflected and transmitted part of the electromagnetic wave can be described by Fresnel's equations, which are a result of Maxwell's equations. They describe the polarization of light as a superposition of two linearly oscillating wave vectors oriented orthogonally to each other (equation 3.3) [35, 36]. One is defined parallel (p) and the other one perpendicular (s) to the plane of incidence, which is the plane spanned by the incoming light and the surface normal.

$$\begin{aligned} r_{(p,s)} &= \frac{E_{r(p,s)}}{E_{i(p,s]}} \\ t_{(p,s)} &= \frac{E_{t(p,s)}}{E_{i(p,s]}} \end{aligned} \tag{3.3}$$

Here, E_p and E_s are the electric field components parallel and perpendicular to the plane of incidence. The index stands for the incident (i), reflected (r), and transmitted (t) beam, respectively. For reflected light, their ratio is called the complex reflectance ratio ρ

$$\rho = \frac{r_p}{r_s} = \tan \Psi e^{i\Delta} \tag{3.4}$$

which is the fundamental equation in ellipsometry [34, 35]. It includes the previously mentioned amplitude ratio $\tan\Psi$ and phase difference Δ between the two orthogonal components of the ellipse [97],

$$\tan \Psi = \frac{|r_p|}{|r_s|} \qquad \Delta = \delta_p - \delta_s \tag{3.5}$$

These parameters vary in dependence of angle of incidence due to changes in reflectance for p- and s-polarization. The reflectance R is defined as the square of the magnitude of Fresnel's reflection coefficients. Figure 3.2 displays the reflectance of p- and s-polarization in dependence of ϕ_0 for light reflected at an air–silicon interface, assuming $k = 0$.

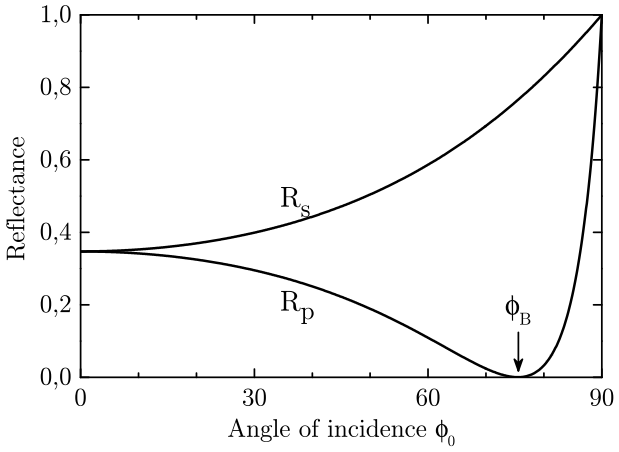

FIGURE 3.2: Plot of Reflectance R_p and R_s at the air–silicon interface in dependence of incident angle.

It can be seen that the fraction of reflected light differs for p- and s-polarization. While R_s steadily increases with increasing incident angle, R_p passes through a minimum with $R_p = 0$ at the Brewster angle ϕ_B. In the case of $k \neq 0$ the reflectance R_p does not reach zero anymore and the minimum is called pseudo-Brewster angle [36]. In ellipsometry, the angle of incidence is often chosen close to the (pseudo) Brewster angle, because it results in a high ratio of reflection coefficients. Consequently, a high sensitivity of the measurement is achieved, with small differences in sample properties leading to prominent changes of the corresponding spectral features.

Jones and Stokes formalism

A mathematical description of the polarization state of light and its transformation by optical devices can be given with the Jones formalism [35, 36]. The Jones *vector* gives the state of polarization via the two wave components E_p and E_s. In dependence of the direction of propagation z and the time t the Jones vector is

$$E(z,t) = \begin{bmatrix} E_p \\ E_s \end{bmatrix} = \begin{bmatrix} E_{p0} \exp(i\delta_p) \\ E_{s0} \exp(i\delta_s) \end{bmatrix} \tag{3.6}$$

When the intensity is normalized to I = 1, linear polarization in p-, s- or 45°-direction, for example, is written as

$$E_{p,\text{linear}} = \begin{bmatrix} 1 \\ 0 \end{bmatrix} \qquad E_{s,\text{linear}} = \begin{bmatrix} 0 \\ 1 \end{bmatrix} \qquad E_{+45^\circ} = \frac{1}{\sqrt{2}} \begin{bmatrix} 1 \\ 1 \end{bmatrix} \tag{3.7}$$

Transformation of polarization by an optical device, such as a polarizer or retarder, is described by the Jones *matrix*. For example, the Jones matrix for a polarizer P with its transmission axis parallel to the E_p-vector is

$$P = \begin{bmatrix} 1 & 0 \\ 0 & 0 \end{bmatrix} \tag{3.8}$$

and the polarization state of incident light linearly polarized at 45° that passes such a polarizer can be calculated via multiplication of the incident Jones vector from the left with the polarizer's matrix

$$\begin{bmatrix} E_p \\ E_s \end{bmatrix} = \frac{1}{\sqrt{2}} \begin{bmatrix} 1 & 0 \\ 0 & 0 \end{bmatrix} \begin{bmatrix} 1 \\ 1 \end{bmatrix} = \frac{1}{\sqrt{2}} \begin{bmatrix} 1 \\ 0 \end{bmatrix} \tag{3.9}$$

A drawback of the Jones formalism is that it can only describe completely polarized light. If one has to deal with partial polarization due to depolarization effects from optical components or the sample, or incomplete polarization at the polarizers (as it is the case in real experiments) the Stokes formalism is used [35, 36].

The Stokes parameters are the ones being measured in ellipsometry and can be defined as light intensities at different polarizer settings (equation 3.10). S_0 represents the total intensity. For totally polarized light the last equation in 3.10 is equality, while the inequality stands for partially polarized light [101, 102].

$$\begin{aligned} & S_0 = I_{0^\circ} + I_{90^\circ} \\ & S_1 = I_{0^\circ} - I_{90^\circ} \\ & S_2 = I_{+45^\circ} - I_{-45^\circ} \\ & S_3 = I_R - I_L \\ \text{with} \quad & S_0^2 \geq S_1^2 + S_2^2 + S_3^2 \end{aligned} \tag{3.10}$$

Their correlation to Ψ and Δ is given in equation 3.11, normalized to the total intensity S_0 [35, 36].

$$\begin{aligned} S_0 &= 1 \\ S_1 &= -\cos(2\Psi) \\ S_2 &= \sin(2\Psi)\cos\Delta \\ S_3 &= -\sin(2\Psi)\sin\Delta \end{aligned} \tag{3.11}$$

3.1.2 Determination of tanΨ and Δ

With an ellipsometric configuration as depicted in figure 3.1, the field amplitude E at the detector can be described in dependence of the azimuth angles P and A at the polarizer and analyzer, respectively [35], as

$$E = E_\mathrm{i}(r_p \cos P \cos A + r_s \sin P \sin A) \tag{3.12}$$

Due to polarization effects of the source or a polarization-dependent detector, it is necessary to set the corresponding polarizer at a fixed value while rotating the other. It has become common practice to set the fixed polarizer to $\alpha_1 = 45°$, thereby the incident field amplitudes are of equal magnitude. The detected intensity in dependence of the

rotating polarizer's azimuth α_2 is

$$\mathrm{I}(\alpha_2) = \frac{1}{2}(S_0 + S_1 \cos(2\alpha_2) + S_2 \sin(2\alpha_2)) \tag{3.13}$$

In an FTIR spectrometer the interferometer has partly polarizing properties, therefore in an ellipsometer coupled to an FTIR the polarizer in front of the sample should be the one with fixed azimuth. Instead, the analyzer is set to four positions at 0°, 90°, +45°, and −45° respectively. This approach has already been shown in the definitions of the Stokes parameters in equation 3.10. From these measured intensities Ψ and Δ can be derived via

$$\begin{aligned} \cos 2\Psi &= \frac{I(90°) - I(0°)}{I(90°) + I(0°)} \\ \sin 2\Psi \cos \Delta &= \frac{I(+45°) - I(-45°)}{I(+45°) + I(-45°)} \end{aligned} \tag{3.14}$$

Note that Δ is not determined directly but via $\cos\Delta$, resulting in inaccuracy for values of $\cos\Delta \approx \pm 1$. This can lead to improper thickness determination, since Δ is more sensitive to thickness changes than tanΨ. To overcome this, measurements of the same settings with a retarder, which is placed between sample and detector to induce an additional phase shift δ, are recorded. It results in the value $\cos(\Delta + \delta)$ and, together with the measurement without retarder, Δ can be determined with good sensitivity [35]. A drawback of this procedure is the double amount of time necessary for the measurements. For the studies conducted in this work, measurements with retarder were not performed. Instead, the thickness results obtained from in situ VIS ellipsometric measurements and in situ AFM were used. Therefore, in IR-SE the spectra of tanΨ were sufficient to gain the desired information about the polymer brushes and their interaction with the environment.

A different way to determine tanΨ is via direct measurement of the intensities of E_p and E_s and calculation of tanΨ. This is done by fixing both polarizers to the same azimuth and results in a higher number of photons at the detector. If $P = A = 0°$, $\cos P = \cos A = 1$ and $\sin P = \sin A = 0$ in equation 3.12. In an analogous manner, setting both polarizers to 90° leads to $\cos P = \cos A = 0$ and $\sin P = \sin A = 1$. As it turns out, the reflection coefficients are directly accessible which leads to tanΨ according to

$$\begin{aligned} \tan\Psi &= \frac{|E_i\, r_p|}{|E_i\, r_s|} = \frac{|r_p|}{|r_s|} \\ \text{with} \quad I \propto |E|^2 \qquad \tan\Psi &= \sqrt{\frac{I(0°, 0°)}{I(90°, 90°)}} \end{aligned} \tag{3.15}$$

In the case of an isotropic bulk sample or the presence of only one isotropic layer between the bulk and ambient media, measurement of the two ellipsometric parameters enables to derive n and k directly [35, 37]. However, when more layers are present on the sample the number of unknown parameters exceeds the number of measured ones, so that the sample properties are not directly accessible anymore. Instead, an optical layer model is used to describe the light path through the layers and the changes at

each interface. Modeling is also necessary for anisotropic samples [92]. With iterative methods the parameters of the model are varied to achieve the best fit between measured and simulated spectra [93, 97]. There are various dielectric function models that can be used to describe the sample and to extract physical properties of the layers. Some are applied in a spectral region where the sample is transparent (e.g. Cauchy model), while others include oscillators to account for resonance frequencies (e.g. Drude, Lorentz, Gaussian models). A description of the models used in this work will be given in section 4.3.

3.1.3 Experimental Setup

VIS Ellipsometry

The majority of ellipsometric applications use light in the UV–VIS range for fast determination of thin layer thickness and refractive index as well as live monitoring of thin-film growth, etching, and thermal oxidation processes [36]. In this work, VIS ellipsometry was employed *ex situ* to pre-characterize the polymer brush samples and *in situ* to obtain results on the swelling behavior of the brushes. Most of the VIS ellipsometry measurements were done by Eva Bittrich and Stefan Adam at IPF Dresden. The ex situ setup corresponds to figure 3.1. Measurements were performed under ambient conditions (23–25 °C, ≈ 30% humidity) at different angles of incidence with Ψ and Δ being recorded in dependence of wavelength. Results were used to check the samples for successful grafting of the polymer brushes as well as dry layer characterization.

For in situ VIS ellipsometry measurements the samples were placed in a temperature-controlled cuvette with its side windows oriented to be perpendicular to the incoming radiation. The angle of incidence was set to 68° [28, 37]. The sequence of in situ measurements usually started with the sample in dry state, followed by filling the cuvette with solution and probing at temperatures in the range of 15–55°C. In the case of protein adsorption experiments the in situ sequence consisted of two parts: First, the sample was measured in plain buffer solution at the desired temperatures. Then, buffer solution was replaced with protein-containing buffer and measurements were repeated at the same temperatures as before. Finally, a rinsing step with buffer solution was performed to evaluate possible protein desorption. In all cases, phosphate-buffered saline (PBS) was used at a concentration of 0.01 mol/l and a pH of 7.4. Protein solutions were prepared with a concentration of 0.25 mg/ml in PBS.

Infrared Ellipsometry

Ex situ IR-SE measurements of the polymer brushes were recorded with the angle of incidence set to 65°. For silicon with $n = 3.42$ at $400\,cm^{-1}$ the Brewster angle is approximately 74° (see section 3.1.1). The samples were mounted on a simple holder so that the reflexion at the sample–air interface was detected. The scheme shown in figure 3.1 basically represents the ex situ setup for IR-SE measurements. Here, an FTIR spectrometer is used as source and the ellipsometer is placed in an acrylic glass box purged with dried air to reduce atmospheric absorptions from water and carbon dioxide. Data was recorded after sufficient purging of the ellipsometric compartment. The decrease in humidity could be followed in the IR spectra via the decrease of atmospheric water bands in the range of 1900–1300 cm^{-1}. The best results were obtained after purging the chamber for about 1 hour, resulting in a remaining relative humidity of < 0.01%.

For in situ measurements, a specially designed flow cell was used [42]. A schematic cross-section of the cell is displayed in figure 3.3. The cell is a polymeric frame (PEEK) with an approximately 20 mm x 15 mm x 7 mm sized inner cavity and equipped with inlet and outlet tubes. It is closed on one side with a quartz glass window, and on the other with the infrared-transparent silicon wedge that is utilized as substrate, with its brush-coated side facing the interior of the cell. Radiation is directed through the wedge onto the brush–liquid interface. The in situ cell is temperature-controlled by a peltier element and a Pt1000 sensor connected to a PID-control device (OsTech GmbH, Berlin, Germany) with a stability of ± 0.05 °C. It enables measurements in the range of 20–60 °C. The presented setup has several advantages. First, the wedge angle generates a divergence between the outer and inner reflex of the wedge, indicated by red and green arrows in figure 3.3. The detector is arranged to capture the inner reflexion (green arrow), that is, the reflexion from the solid–liquid interface. Another advantage of the wedged shape is that interferences due to multiple reflections between the silicon surfaces are minimized. Finally, recording the reflected beam through the substrate instead of the aqueous solution is necessary, because water strongly absorbs IR radiation. The penetration depth of IR light in water lies in the range of only a few micrometers [37].

In situ IR-SE spectra were recorded with the angle of incidence at the instrument set to 52.5° at the outer surface of the wedge. To direct the inner reflexion to the detector the sample holder needed to be slightly rotated. According to Snell's law the incidence angle on the solid–liquid interface results in about 13.3°.

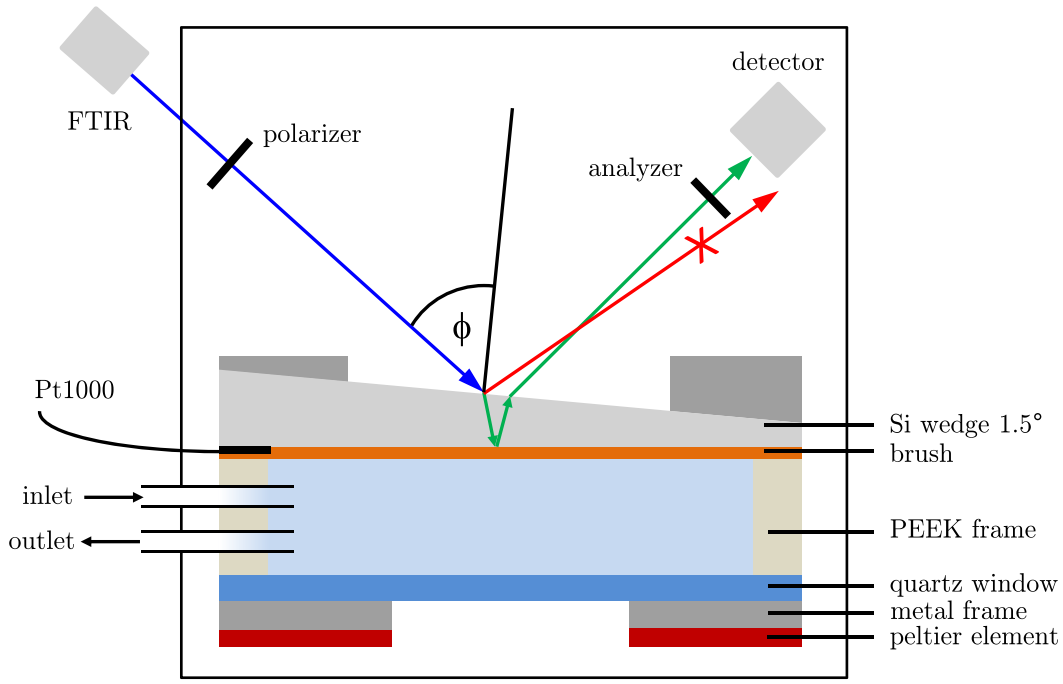

FIGURE 3.3: Scheme of the IR-SE setup with a cross-section of the in situ cell (dimensions are not to scale). The box represents the compartment that is purged with dry air.

The course of in situ tanΨ measurements was as follows: First, the measurements of the reference substrate were performed. This was done in dry state, meaning with the flow cell purged with Ar or N_2. Then the cell was filled with the liquid (water, buffer solution, protein solution) and the temperature set to the desired value. When a stable temperature was reached ($\pm 0.1\,^{\circ}C$) the measurement was started. This was repeated until spectra at all desired temperatures and in all desired solutions had been recorded.

3.2 Atomic Force Microscopy

Atomic force microscopy (AFM) is a technique to image surface topography and is classified to the group of scanning probe microscopes. These techniques use a very small tip to scan the sample surface and are able to measure different properties, such as height, lateral forces, adhesion, etc. down to atomic scale resolution. AFM in particular probes the force between tip and sample and is able to scan any sample material, while a scanning tunneling microscope (STM), for example, can only be applied on conducting surfaces [103, 104]. A scheme of the setup of an atomic force microscope is shown in figure 3.4. The tip is attached to the end of a flexible cantilever that can be moved in z direction. The sample is placed on an x, y stage and moved beneath the cantilever in close proximity to the tip. The force between tip and sample causes a deflection of the cantilever, which is proportional to the tip–sample force and can be detected with a laser reflected at the surface of the cantilever onto a photodiode. A controlling unit ensures feedback between the detected deflection of the cantilever and the position of tip and sample [103].

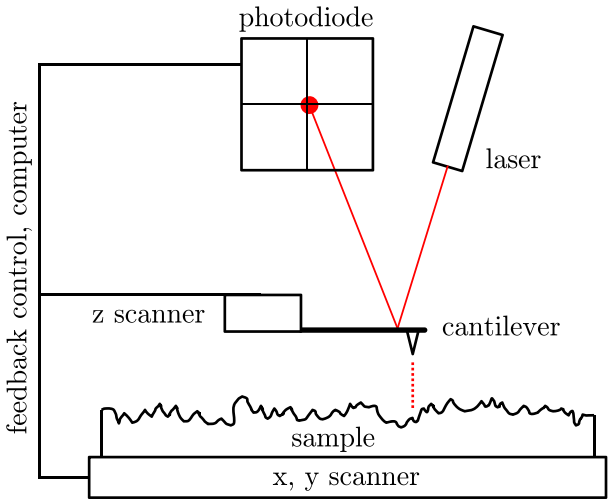

FIGURE 3.4: Scheme of the general setup of an atomic force microscope.

There are various modes of operation possible in AFM, mainly differentiated between contact, non-contact and tapping mode. The choice of the mode depends mainly on the nature of the sample. Especially the sample's softness and surface roughness are the important parameters. Different information can be obtained from the measurements, for example topography, phase images or the adhesion force between tip and surface. In contact mode the tip of the cantilever is in contact with the sample and bends according to the surface topography. The cantilever's deflection is then translated into a height profile. A disadvantage of this mode is fast abrasion of the tip caused by the contact with the sample and damage on the sample itself, especially when large height differences

occur on the sample over a short distance. Therefore this mode is preferred on hard samples with low roughness [105].

Non-contact and tapping (=intermittent contact) modes use an oscillating cantilever, thus they are often referred to as dynamic modes. These modes cause less damage to the tip due to reduced contact between sample and tip, so they are suitable to measure soft structures such as biological samples and organic thin films. In tapping mode, the cantilever is oscillated at a fixed frequency at or near its resonance frequency. It is held at a close distance to the sample and only touches it intermittently. The change of forces between tip and surface results in a change of oscillation amplitude, which acts as feedback parameter. In non-contact mode the cantilever is oscillated exactly at its resonance frequency and in most cases does not touch the sample, resulting in even less sample damage than tapping mode. Feedback parameter in this case is the change of resonance frequency due to tip-sample interactions. In both these dynamic modes, the z-position of the cantilever is adjusted by the feedback controller to restore the initial condition. This information is translated into a topography image [106].

In this work AFM measurements were only performed in the dynamic modes on the PNIPAAm-*b*-PGMA copolymer brushes, since the contact mode would cause too much damage to soft samples like polymers [105]. The non-contact mode was used at the Park Systems instrument in Berlin to record topography images in dry state under ambient conditions. The oscillation amplitude was set in the range of 9–16 nm. This mode was chosen to prevent damage to the sample, especially because the samples were used afterwards for the IR-SE experiments.

In situ AFM scans and thickness determination were performed on additional PNIPAAm-*b*-PGMA copolymer brushes on silicon wafers. The experiments were done in the laboratory of Sergiy Minko's group at University of Georgia with supervision by Oleksandr Trotsenko. The instrument used is a Bruker Dimension Icon which operates in the PeakForce QNM^{TM} tapping mode. The tapping frequency was set to 2 kHz and a peak force of 1.5 nN. This tapping mode works with intermittent tip–sample contact and, additionally to the height image, records a force curve at each tapping of the sample map from which a topographic image of the adhesion force is generated. Compared to the conventional tapping force the damage of the tip is reduced by control of the maximum force between tip and sample [107]. For thickness determination of the copolymer brushes a part of the brush layer was scratched away with a needle that is softer than silicon but harder than the polymer. AFM scans were recorded at the resulting step edge in dry state as well as in water at 25 °C and 40 °C. During the dry state measurements the sample chamber was purged with nitrogen and the sample was heated to 65 °C to remove atmospheric water from the brushes. Measurements in water were performed by placing a drop on the sample and dipping the cantilever into it to scan the solid–liquid interface. The sample stage is equipped with a heating plate and allows temperature control with a precision of ± 0.1 °C.

Data evaluation of AFM images was made with the open source software Gwyddion. It provided image tools such as regression analysis to determine the average height in a selected region of the sample. This tool was used to calculate the height difference at the step edge on PNIPAAm-*b*-PGMA copolymer brushes. Height profiles and surface roughness were also extracted.

Chapter 4

Sample Preparation and Data Evaluation

This chapter summarizes details on synthesis, preparation, and characterization and how this was integrated in the cooperation with partners in the USA and Germany. It begins with a list of materials and instruments used for sample preparation and in situ experiments. Afterwards, the polymer synthesis and characterization of the resulting polymer chains are briefly introduced for each polymer system. This is followed by the detailed description of brush preparation and preliminary characterization of the brushes, which were performed in the laboratories of cooperation partners at Clemson University (USA), Clarkson University (USA), and IPF Dresden (Germany). The last section of this chapter describes the data evaluation and simulation procedure, including corrections that were made to be able to fit simulated data to the measured spectra.

4.1 Materials

The two different systems of temperature-sensitive polymer brushes are based on the well-known polymer PNIPAAm and on POx. All brushes were prepared by the 'grafting-to' method with PGMA used as anchor between substrate and brush polymer. Table 4.1 lists the used polymers and materials, which were either purchased or synthesized by cooperation partners. A list of used devices and software is given in table 4.2.

TABLE 4.1: List of materials used in this work.

Material	Specifications	Manufacturer
Silicon (111) wedge	p-type, 1.5°	Vario GmbH, Germany
Silicon (100) wafer		Si-Mat, Germany
Silicon (111) wafer		Semiconductor Processing Co., USA
PNI-70	35.7 kg/mol	synthesized at ORNL, B.S. Lokitz
PNI-40	65.5 kg/mol	synthesized at ORNL, B.S. Lokitz
PMeOx	22.0 kg/mol	Polymer Source Inc., Canada
P*c*PrOx	48.4 kg/mol	synthesized at IPF, S. Adam
copolymer10	52.6 kg/mol	synthesized at IPF, S. Adam
copolymer25	61.3 kg/mol	synthesized at IPF, S. Adam
PGMA	17.5 kg/mol	Polymer Source Inc., Canada
PBS tablets	0.01 mol/l, pH 7.4	Sigma-Aldrich, Germany
FIB	340 kDa, 95%	Calbiochem, USA
HSA	66 kDa, 99%	Sigma-Aldrich, Germany
Ethanol	99.8%, p.a.	Sigma-Aldrich, Germany
D_2O	99.9%	Sigma-Aldrich, Germany
MEK	99+%	Acros Organics, USA
$CHCl_3$	ACS Grade	Acros Organics, USA
H_2SO_4	98%, ACS Grade	Acros Organics, USA
H_2O_2	30%, ACS Grade	Acros Organics, USA

TABLE 4.2: List of instruments and software used in this work.

Name	Manufacturer
IR ellipsometer	Bruker Vertex 70 & custom-built ellipsometer
LN_2 cooled MCT detector	InfraRed Associates, Inc., USA
Temperature control unit	Ostech, Germany
VIS ellipsometers (ex situ)	SE850, Sentech, Germany
	SE402, Sentech, Germany
VIS ellipsometer (in situ)	alpha-SE, J.A. Woollam Co., Inc., USA
in situ cuvette	TSL Spectrosil, Hellma, Germany
AFM	XE-100, Park Systems, South Korea
AFM (in situ)	Bruker Dimension Icon, with ScanAsyst™, Germany
Dip-coater	Mayer Feintechnik D-3400, Germany
OPUS software	Bruker, Germany
SpectraRay/3 software	Sentech, Germany
Origin 9.1 software	OriginLab, USA
Gwyddion 2.40 software	Freeware (https://gwyddion.net)
MatLab R2012b	MathWorks, USA

4.2 Polymer Syntheses and Brush Preparations

4.2.1 Poly(2-oxazoline) Brushes

POx synthesis and brush preparation was done at IPF in Dresden by Stefan Adam. PMeOx was purchased, the other polymers were synthesized via a microwave-assisted cationic ring-opening polymerization (CROP) in benzonitrile [108]. Except for MeOx the used monomers *c*PrOx and methyl-3-(oxazol-2-yl) propionate (EsterOx) were also synthesized at the IPF as described elsewhere [31, 108, 109].

Polymerization

First, a short starting block of 2–4 EsterOx units bearing methyl ester groups in the side chain was synthesized via initiation by methyl triflate. This EsterOx block served as initiator for the CROP of the main polymer. The monomer solution for the CROP reaction either contained only *c*PrOx or a mixture of *c*PrOx and MeOx in the ratio 3:1 or 9:1, resulting in statistic POx copolymers with 25% (copolymer25) and 10% (copolymer10) MeOx, respectively. Polymerizations were performed under microwave heating at 100 °C. The living chain ends were terminated via hydrolysis (P*c*PrOx, copolymer10) or with piperidine (copolymer25). According to experiments of our collaboration partners at IPF the end groups did not have any effect on the temperature-responsive polymer characteristics. For purification, the polymers were precipitated in cold n-hexane, redissolved in $CHCl_3$, and dried under reduced pressure. To transform the methyl ester groups of the EsterOx block into free carboxylic groups, the polymers were hydrolyzed via a modified procedure according to Rueda et al. [110]. More detailed descriptions of the monomer synthesis as well as the polymerization procedure can be found in literature [31, 108, 109].

Characterization of the polymer chains

Molecular weights of the resulting polymers were determined with size exclusion chromatography at IPF Dresden (see table 4.3). Turbidity measurements were performed to determine the cloud point temperature (T_{cp}) of the polyoxazoline chains in solution. T_{cp} is defined as the temperature at which a polymer solution turns from transparent to opaque due to the phase separation of the solution. The experiments were conducted at IPF Dresden on a UV-VIS spectrophotometer (Agilent Varian Cary 50) containing a temperature-controlled cuvette holder. The optical path length in the quartz cuvettes was 4 mm. Absorption values of POx solutions of different concentrations between 1–50 mg/ml were measured at a wavelength of 550 nm in the range of 15–45 °C in 1 °C-steps and converted into transmission values [108, 111]. T_{cp} was set as the inflection point of the transmittance vs. temperature curve. The T_{cp} values at 50 mg/ml are given in table 4.3.

Brush preparation

Polyoxazoline brushes were prepared via the 'grafting-to' approach [56] on polished, infrared-transparent silicon wedges (1.5°) with (111)-orientation. The wedges were cleaned by ultrasonication in ethanol followed by an oxygen plasma treatment to remove organic residues and activate the surface with silanol groups. On these cleaned and activated silicon substrates a thin (~ 2.0 nm) PGMA anchoring layer was deposited via spin-coating from a 0.3 mg/ml (0.02 wt %) solution in $CHCl_3$. Annealing at 100 °C

TABLE 4.3: Characteristics of the poly(2-oxazoline)s used for brush preparation: Molecular weight M_n, polydispersity index (PDI), cloud point temperature T_{cp} at c=50 mg/ml, and glass transition temperature T_g.

POx	M_n [kg/mol]	PDI	T_{cp} [°C]	T_g [°C]
P*c*PrOx	48.4	1.23	18.0	81
Copolymer10	52.6	1.09	22.7	81
Copolymer25	61.3	1.41	29.4	82
PMeOx	22.0	1.27	–	n/a

TABLE 4.4: Dry layer thicknesses d_{dry} for the prepared POx brushes on Si and spin-coated layers on Au as well as the grafting densities σ of the brushes on Si.

POx	$d_{dry,Si}$ [nm]	σ [chains/nm^2]	$d_{dry,\,Au}$ [nm]
P*c*PrOx	10.1 ± 0.1	0.13 ± 0.001	79.8 ± 0.3
Copolymer10	10.1 ± 0.1	0.12 ± 0.001	–
Copolymer25	10.5 ± 0.1	0.10 ± 0.001	87.2 ± 0.3
PMeOx	4.8 ± 0.1	0.13 ± 0.01	85.9 ± 0.5

for 20 min under vacuum lead to a reaction between the silanol groups on the surface and the epoxy groups of the PGMA side chains. The resulting covalently bound and cross-linked PGMA layer was still equipped with a sufficient number of epoxy groups for the subsequent polymer chain attachment. Grafting of the polyoxazoline brush layer was performed by spin-coating a 0.5 wt % POx solution in $CHCl_3$ on top of the PGMA anchoring layer. This layer was annealed under vacuum at 150 °C for 2 h to form a covalent bond between PGMA and the COOH-end-functionalized POx chains. Ungrafted polymer chains were washed out by rinsing several times with $CHCl_3$. The spin-coating and annealing procedure of POx was repeated three times to obtain high grafting densities (see table 4.4). It turned out that three repetitions are sufficient to reach almost maximum surface coverage, because after a fourth cycle only a minor increase in grafting density occurred.

Pre-characterization of the brushes

Dry layer thickness (d_{dry}) of the brushes was determined with VIS ellipsometry and these values used to calculate the grafting density σ of the brushes via equation 4.1. In this equation, ϱ describes the polymer bulk density and N_A is Avogadro's number. The bulk density of the POx used in this work is not known, however, literature values of similar POx are 1.01–1.05 g/cm^3. Therefore, an estimated value of 1.00 g/cm^3 was used for the calculations [108, 112]. Results are given in table 4.4 and show very similar grafting densities due to the repeated grafting process.

$$\sigma = \frac{d_{dry} \cdot \varrho \cdot N_A}{M_n} \tag{4.1}$$

Preparation of spin-coated layers on gold

Additionally to the brushes, thicker spin-coated layers of P*c*PrOx, PMeOx and copolymer25 (25% MeOx) were prepared on gold-coated glass slides without a PGMA layer

underneath. This was done by spin-coating a ~1 wt % POx solution in $CHCl_3$ directly onto the gold layer. Thickness values of the resulting layers were determined with VIS ellipsometry and are given in table 4.4.

4.2.2 Block-Copolymer Brushes PNIPAAm-*b*-PGMA

Synthesis of the linear PNIPAAm-*b*-PGMA chains was performed by Bradley Lokitz at Oak Ridge National Laboratory (ORNL). This was done from glycidyl methacrylate (GMA) and *N*-isopropyl acrylamide (NIPAAm) monomers via reversible addition fragmentation chain transfer (RAFT) polymerization. Details about the reaction procedure can be found in literature [63, 64]. The parameters of the resulting polymers are given in table 4.5. Block-Copolymers with two different compositions of block lengths were used for the brush preparation, which was done on a research visit to the group of Igor Luzinov at Clemson University together with Michael Seeber and Yuriy Galabura. Michael Seeber also studied the resulting brushes with different methods in dry state as well as in situ [63]. A short summary of these results is given in this section after the preparation procedure.

TABLE 4.5: Parameters of the two block-copolymers used for PNIPAAm-*b*-PGMA brush preparation. The copolymer block lengths were chosen to be similar for PNIPAAm and varying for PGMA.

Block-copolymer	M_n [g/mol]	M_w [g/mol]	M_w/M_n
PNI-70	PGMA: 11500 PNIPAAm: 24200 total: 35700	PGMA: 13500 PNIPAAm: 32400 total: 45900	1.28
PNI-40	PGMA: 36600 PNIPAAm: 28900 total: 65500	PGMA: 43900 PNIPAAm: 30200 total: 74100	1.13

Brush preparation

Single crystal silicon wedges (Vario) and wafers (Semiconductor Processing Co.), each with (111)-orientation of the surface, were cleaned in an 80 °C piranha solution, which consists of concentrated sulfuric acid (H_2SO_4) and hydrogen peroxide (H_2O_2, 30%) in the ratio 3:1, followed by repeated rinsing in ultrapure water. This cleaning step removed any organic residues on the surface and activated the surface with silanol groups for the grafting step.

The polymer layer was grafted to the substrate according to the following procedure: First, a 25–30 nm layer of the PNIPAAm-*b*-PGMA copolymer was deposited on the surface via dip-coating (Mayer Feintechnik D-3400) from a solution in methyl ether ketone (MEK). The thickness of the deposited layer could be adjusted by variation of solution concentration and speed of the dip-coating process. We used a copolymer concentration of ~0.75 wt % in MEK and a speed of 240 mm/min. Second, the coated substrates were annealed at 130 °C for 16 hours. In the third step, the grafted layers were repeatedly rinsed in MEK (3 x 30 min) and dried under nitrogen flow.
For such thin layers of the copolymer brushes (< 30 nm) nearly all coated polymer chains were grafted to the surface, thereby eliminating the need for the subsequent rinsing step [63]. Nevertheless, this rinsing step has been performed on all brushes studied in this work, as described above. Several samples of each block-copolymer composition

TABLE 4.6: Parameters of the two sets of PNIPAAm-*b*-PGMA copolymer brushes studied in this work. The grafting density σ is related to the PNIPAAm chain density and was calculated according to equation 4.2 [63]. d_{dry} is the thickness of the polymer layer in dry state, determined with AFM on the step edge on wafers and with VIS ellipsometry on wedges.

Sample	Substrate	experiment	σ [nm^{-2}]	d_{dry} [nm]
PNI-70	Si wedge	IR-SE	0.61 ± 0.01	32.4
	Si wedge	IR-SE	0.50 ± 0.01	26.8 ± 0.2
	Si wafer	AFM	0.46 ± 0.01	24.1 ± 0.3
	Si wafer	VIS	0.49 ± 0.01	26.1 ± 0.2
PNI-40	Si wedge	IR-SE	0.30 ± 0.002	28.0
	Si wedge	IR-SE	0.27 ± 0.002	28.4 ± 0.2
	Si wafer	AFM	0.25 ± 0.002	23.0 ± 0.3
	Si wafer	VIS	0.28 ± 0.002	25.4 ± 0.2

were prepared on different silicon substrates. These were necessary for in situ IR-SE measurements (wedges) and in situ VIS ellipsometry and AFM measurements (wafers). Their dry layer thickness and calculated grafting density are listed in table 4.6.

Pre-characterization of the brushes

The following paragraphs describe preliminary results that Michael Seeber obtained during his doctoral research [63], including brush parameters, angle-resolved x-ray photon spectroscopy (AR-XPS) results, and contact angle measurements.

Grafting densities σ of brushes normalized to a thickness of 30 nm were calculated according to equation 4.2. In this equation, Γ describes the surface coverage of polymer chains (in mg/m^2) via the density ϱ of the macromolecules and the layer thickness h. Values for ϱ were calculated via the software Polymer Design Tools (DTW Associates, Inc.) and resulted in $1.05\,g/cm^3$ for PNIPAAm and $1.27\,g/cm^3$ for PGMA. The results of σ are $\sim 0.5\,nm^{-2}$ and $\sim 0.3\,nm^{-2}$ for PNI-70 and PNI-40 [63], respectively, while it is about $0.3\,nm^{-2}$ for traditional PNIPAAm grafting-to brushes [16, 28, 63].

$$\sigma = \frac{\Gamma \cdot N_A \cdot 10^{-21}}{M_n} \quad \text{with} \quad \Gamma = h \cdot \varrho \tag{4.2}$$

Angle resolved x-ray photon spectroscopy (AR-XPS) experiments, which have been conducted by our project partners at Clemson University in collaboration with Georgia Tech, provided information about the composition of the top ~10 nm of the brushes as well as PNIPAAm and PGMA references [63]. Especially the nitrogen content determined with AR-XPS at different angles of incidence (resulting in different penetration depths of the radiation) is a valuable information to estimate the amount of PNIPAAm in the probed areas of the top 2–10 nm. While the nitrogen content is about 12% for a PNIPAAm reference layer and about 11% for a traditional PNIPAAm reference brush, the top 2 nm of the copolymer brushes have a nitrogen fraction of 9–10% which further decreases at increasing probing depth. This indicates that PGMA is present even in the top parts of the brush and its fraction increases with probing depth. An estimation of the PNIPAAm fraction in the outermost 2 nm region of the copolymer brushes resulted in 80% for PNI-70 and only 71% for PNI-40, while it is 95% for the PNIPAAm reference brush. Changes in carbon content are similar for all samples—copolymers as well as

PNIPAAm references—decreasing by 1.5–2.0% at increasing probing depth. An exception is the PGMA reference, its carbon content decreases by 3%. For the PNIPAAm and PGMA reference layers Michael Seeber explains it to be a preferred occurrence of the carbon-rich backbone at the brush–ambient interface with the nitrogen- and oxygen-containing side chains turned inwards, towards the bulk layer. The copolymer brushes generally seem to have a higher density in their topmost layer, because both carbon and nitrogen content are highest in this region.

Temperature-dependent advancing contact angle measurements were performed after two different solvent treatments (MEK and cold water) of the brushes. MEK served as a good solvent for both PNIPAAm and PGMA, while cold water is only a good solvent for PNIPAAm. This should give information about the mobility of the PNIPAAm and PGMA blocks, compared to a PNIPAAm reference brush. Measurements were performed at 25 °C and 40 °C [63].

The MEK rinse resulted in a small temperature-dependent change of contact angle (6–7°) for PNI-70 and the PNIPAAm reference brush. PNI-40 on the other hand showed a difference of 17°. Especially at low temperature its contact angle was much smaller than for the other two samples. The behavior of PNI-70 is explained by Michael Seeber as insufficient cross-linking between the PGMA blocks, enabling both polymers to be equally 'washed' to the surface by the non-selective solvent. PNI-40 on the other hand is strongly cross-linked, therefore only the temperature-responsive PNIPAAm is mobile and can be washed to the surface, while PGMA blocks are hidden underneath [63].

The water rinse greatly increased the surface switchability of PNI-70 to a difference in contact angle of 23°, while it slightly decreased for PNI-40 from 18° to 11°. (Including the error range, it stayed about the same for PNI-40.) At this point the good mobility of PNIPAAm blocks in PNI-70 is obvious, compared to the 'locked' state in PNI-40 due to strong cross-linking of the PGMA blocks. No changes from MEK rinse to water rinse were detected for the PNIPAAm reference brush, proving the presence of a 2-layer-system with a thin PGMA anchoring layer on the substrate and the PNIPAAm brush layer on top. However, it has a smaller surface switchability than both block-copolymer brushes, which is due to its lower grafting density. As described in literature [28, 113] the switching amplitude of PNIPAAm grafting-to brushes is dependent on molecular weight and grafting density of the chains. At low grafting density there are less interchain interactions, which reduces their collective collapse above the LCST.

4.3 Data Analysis

Data Analysis is the most important step in ellipsometry. As it was stated in section 3.1.2, direct calculation of physical layer parameters from measured Ψ and Δ is only possible in the case of a bulk material or a single isotropic layer with sharp boundaries. But in real samples this is rarely the case due to surface roughness or the presence of additional layers, which increase the number of unknown parameters. For example, the polymer brushes studied in this work were prepared on crystal silicon substrates that are covered with a native silicon oxide layer. For such layered samples an optical model needs to be applied and varied via an iterative method to find the best fit between simulated and measured spectrum. From the obtained simulation the unknown physical parameters can then be derived.

In IR-SE, even without modeling one can learn a lot about the sample by qualitative spectral analysis. Position and shape of the vibrational bands can give information about functional groups present in the layer and also about interactions between different groups or with surrounding molecules. For thin layers, these signals are small and might overlap with bulk signals. Even though ellipsometry is known to be a reference-free method, where only the polarization state of the reflected beam is analyzed, in IR-SE it is advantageous to record a reference spectrum of the uncoated substrate. The ratio between $\tan\Psi$ spectra of sample and reference is then used for interpretation. This way the vibrational bands of the sample can be resolved from overlapping substrate bands [114].

To be able to import our measured data into the simulation program and compare simulated and measured $\tan\Psi$ spectra, spectral correction was necessary. In the following sections these corrections as well as different layer models and simulation fitting procedures, that were employed on the spectra in this work, are described.

4.3.1 Correction of IR-SE Spectra

Measurements are never ideal. Usually the various components of an instrument induce some kind of imperfection, especially optical components. In an FTIR for example, the beam-splitter is a common source for partial polarization. Furthermore, collimation mirrors may not have an exact focus point, and there can be adsorbate layers on the surfaces of optical devices. Some of these instrumental errors can be removed in IR-SE via an empty channel measurement (E) to which sample measurements are referenced. This has been done with all spectra recorded in this work. Equation 3.15 then reads

$$\tan\Psi = \sqrt{\frac{I(0°,0°)/E(0°,0°)}{I(90°,90°)/E(90°,90°)}} \tag{4.3}$$

Additionally, reference measurements of uncoated substrates were recorded under the same conditions as the respective samples. The ratio $\tan\Psi_{\text{sample, meas}}/\tan\Psi_{\text{ref, meas}}$ was then used for spectral interpretation. Especially for in situ measurements this referencing was necessary to resolve the small polymer bands within the large bulk water signals.

The upper panel of figure 4.1 shows exemplarily the measured $\tan\Psi$ spectra of a P*c*PrOx brush in water at 20 °C as well as the respective Si reference spectrum under identical conditions. These spectra are the result of equation 4.3. The graphs look the same due to the bulk water signals around 3600 cm^{-1} and 1650 cm^{-1}. Calculation of the quotient $\tan\Psi_{\text{brush}}/\tan\Psi_{\text{Si}}$ removes the bulk water signals and the polymer bands of the thin layer become visible, as can be seen in the lower panel of figure 4.1 (grey spectrum). In the following analysis within this work only the quotient spectra will be shown.

A problem we faced in the simulation of IR-SE spectra was that the simulation program SpectraRay/3 can only handle raw data, meaning a simulation of referenced spectra is not possible. To be able to compare referenced spectra of measurement and simulation, two spectra needed to be simulated: One for the sample and one for the reference. Since measured and simulated reference spectra (with the reference simulated from literature data) also show deviations between each other, we used a modified raw spectrum for the import to SpectraRay/3: The referenced spectrum $\tan\Psi_{\text{sample, meas}}/\tan\Psi_{\text{ref, meas}}$ was multiplied again with a simulated reference spectrum $\tan\Psi_{\text{ref, sim}}$.

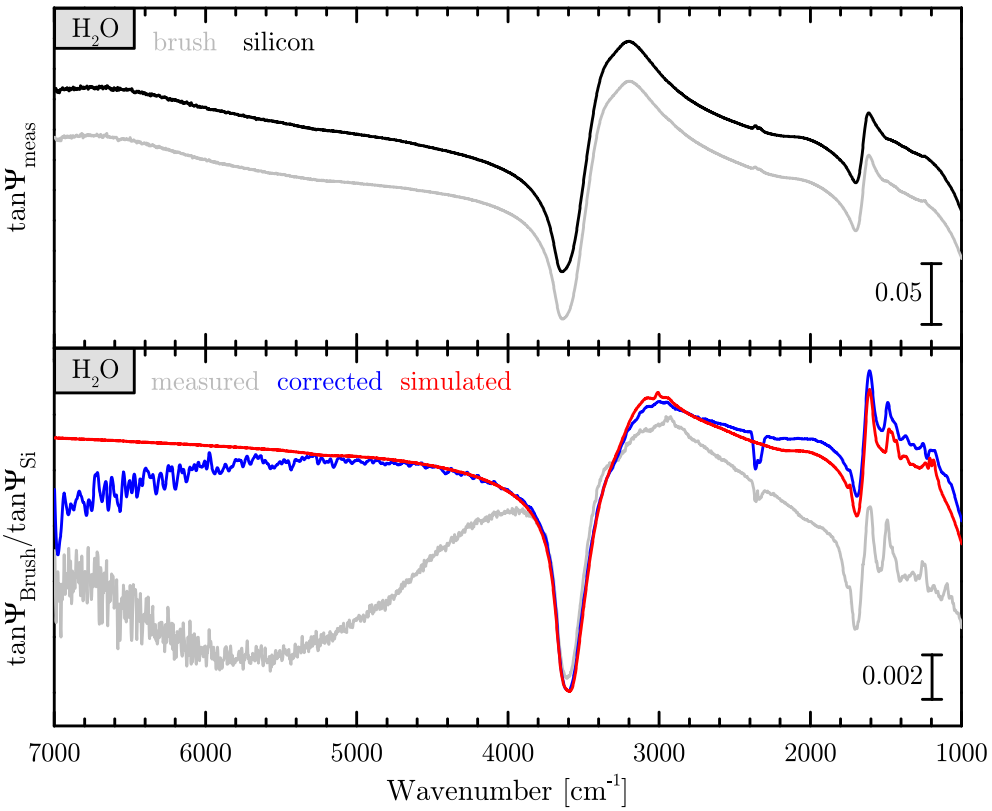

FIGURE 4.1: Measured, corrected and simulated in situ tanΨ spectra of P*c*PrOx in H_2O at 20°C. The upper panel shows the raw measured spectra of brush and reference. The ratio of the two is shown in the lower panel (grey spectrum), as well as the corrected (blue) and simulated (red) spectra.

The above procedure is sufficient for ex situ tanΨ spectra. Applying this procedure to in situ tanΨ spectra to enable their import into the simulation program involves further corrections. We now have to deal with a deviation of the baseline, that is caused by the two silicon wedges—sample and reference—not being mounted in exactly the same way into the in situ cell. This difference can be determined by forming the quotient of sample and reference tanΨ spectra measured with a dry cell: $\tan\Psi_{\text{sample, dry, meas}}/\tan\Psi_{\text{ref, dry, meas}}$. The ratio between the referenced sample in wet state and the one in dry state then removes the deviation of the baseline. Unfortunately, the ratio still contains the sample's dry state bands in the denominator, leading to an unwanted introduction of the dry state bands in the in situ spectrum. Its correction requires a third term $\tan\Psi_{\text{sample, dry, sim}}/\tan\Psi_{\text{ref, dry, sim}}$ that needs to be simulated and multplied with the previously mentioned ratio. The full in situ correction then reads

$$\tan\Psi_{corr} = \frac{\left(\frac{\tan\Psi_{\text{sample, wet, meas}}}{\tan\Psi_{\text{ref, wet, meas}}}\right)}{\left(\frac{\tan\Psi_{\text{sample, dry, meas}}}{\tan\Psi_{\text{ref, dry, meas}}}\right)} \cdot \frac{\tan\Psi_{\text{sample, dry, sim}}}{\tan\Psi_{\text{ref, dry, sim}}} \tag{4.4}$$

In the case of POx brushes this correction worked well, because a good simulation of ex situ spectra of thick spin-coated POx films on gold could be obtained. Using this dataset to simulate the polymer brush in the dry in situ cell (last term in equation 4.4)

resulted in a good match with the measured spectrum. As an example, the effects of the above described corrections are shown in figure 4.1. The lower panel shows the ratio between the two spectra of the upper panel (grey spectrum) as well as the corrected spectrum according to equation 4.4 (blue spectrum). The red spectrum is the result of the simulation.

Unfortunately, the correction did not work for the block copolymer samples. This is because spin-coating of thick, non-grafted films of these polymers on gold does not result in layers comparable to the brushes. Instead, after dip-coating without subsequent annealing, the polymer blocks of PNIPAAm-*b*-PGMA copolymers undergo phase separation on the microscale [63]. The thick, non-grafted layers are needed to evaluate the dry layer properties of the polymer, which are used for the last term in equation 4.4. Using a simulation of the ex situ spectra of the dry ~30 nm brushes on silicon was tried, but even though an acceptable ex situ simulation was possible, it did not result in an appropriate simulation of a dry brush in the in situ cell with this data. Therefore, interpretation of the copolymer brushes (section 5.2) will be restricted to simulations of the dry layers ex situ and a qualitative discussion of the in situ spectra.

4.3.2 Layer Models

A simulation is always based on a model. In ellipsometry optical layer models are used which can be based upon different equations for each layer. A common model is the Cauchy dispersion. It can be applied in those ranges of the electromagnetic spectrum where a material is transparent (k = 0), which is a reasonable approximation for many polymers in the UV-VIS. It is most useful at normal dispersion behavior, that is, when the refractive index decreases continuously at increasing wavelength [115]. The Cauchy dispersion defines the refractive index of the material as a Taylor series (in ω^2) and is very useful to determine layer thickness [37]. Its equation is given as

$$n(\lambda) = A + \frac{B}{\lambda^2} + \frac{C}{\lambda^4} \tag{4.5}$$

In this equation, the parameters A, B, and C describe the shape of the curve but have no physical meaning. A is dimensionless and when $\lambda \to \infty$ then n(λ) $\to$ A. Parameters B and C describe the curvature and amplitude of n in the VIS and UV range, respectively. This implies that for measurements in the VIS range only the first two terms of equation 4.5 are necessary.

The IR range is usually applied for its information about resonances of the material, especially in organic substances, so the Cauchy model is not applied. Instead, oscillator models are used to describe the resonances, for example harmonic (Lorentz) or Gaussian models. They are based on the common approach to describe spectral bands via center frequency, amplitude, and broadening of an oscillator and are applicable for transparent or weakly absorbing materials (= polymers), such as insulators or semiconductors.

For the simulations of vibrational bands in this work, the software SpectraRay/3 was used [116]. It contains the Brendel oscillator model—shown in equation 4.6—that describes vibrational modes with a Gaussian distribution of the center frequency ν_0 of a harmonic (Lorentz) oscillator with strength ν_P. By setting either the Gaussian standard deviation σ to zero or the damping of the harmonic oscillator ν_T to zero with $\sigma \neq 0$,

the model becomes the shape of either a Lorentz oscillator or a Gaussian oscillator, respectively. In the simulations of this work Gaussian oscillators were used.

$$\chi(\nu) = \frac{1}{\sigma\sqrt{2\pi}} \int_{-\infty}^{\infty} \exp\left(-\frac{(x-\nu_0)^2}{2\sigma_k^2}\right) \cdot \frac{\nu_\mathrm{P}^2}{x^2 - \nu^2 + i\nu_\mathrm{T}\,\nu}\,\mathrm{d}x \tag{4.6}$$

Mixed layers, interpenetration layers, or surface roughness can be represented by effective medium approximations [EMA]. These models describe the layer as some kind of mixture of the components. A possible description for the mixture is to assume inclusions in a host medium using volume fractions f_i of the components. One example is the approximation by Bruggeman [117] (equation 4.7, which is an inclusion of particles of one component in the bulk material of another. Here the effective medium (index e) is set as the host medium, which is necessary when the volume fractions of the components (indices 1 and 2) are similar. The Bruggeman theory was used in this work for polymer–polymer and polymer–water mixtures.

$$\mathrm{f}_1 \frac{N_1^2 - N_\mathrm{e}^2}{N_1^2 + 2N_\mathrm{e}^2} + \mathrm{f}_2 \frac{N_2^2 - N_\mathrm{e}^2}{N_2^2 + 2N_\mathrm{e}^2} = 0 \tag{4.7}$$

4.3.3 Simulation

For all simulations of IR bands, the Brendel oscillator model (see equation 4.6) was used with the damping of the harmonic oscillators (ν_T) set to zero, resulting in Gaussian oscillators. Values for ε_∞ and layer thickness were usually taken from VIS ellipsometry results and fixed to these values.

Once the spectra had been corrected for instrumental and setup errors (as described in section 4.3.1) they could be fitted and simulated with an optical model. First, a model was created for the spin-coated polymer layers on gold. It was composed of a layer stack of gold substrate, polymer layer, and ambient air, as depicted in the left scheme of figure 4.2. Data for the ambient and substrate layers are usually available from literature data and in the model they were defined to be of infinite thickness, leaving parameters for the polymer layer the only (partly) unknown quantity. In the case of polymer brushes on silicon, additional layers needed to be added to account for the native oxide layer of

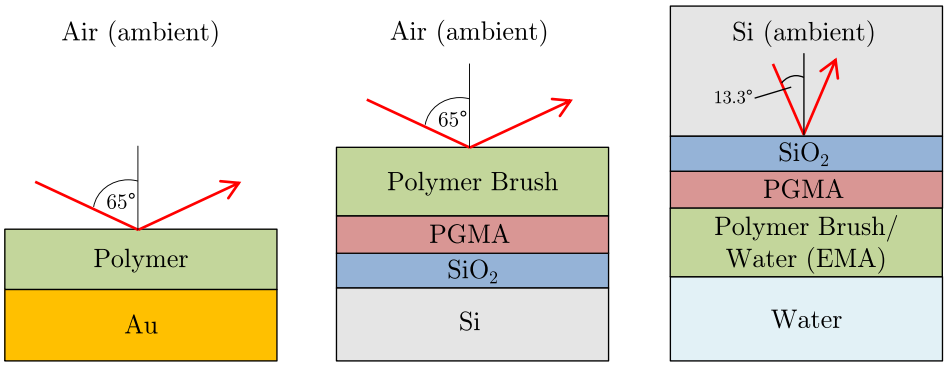

FIGURE 4.2: Schemes of the layer models used for the simulations. Left and Middle: Models for ex situ spectra of samples on gold (left) and silicon (middle). Right: Inverted model for in situ spectra including the effective angle of incidence at the silicon–brush interface.

the substrate and the PGMA anchoring layer (middle scheme in figure 4.2). These can be modeled with literature data or by extracting the dielectric function from measurements and simulation of thick layers of the materials. The data for both the silicon oxide and PGMA layers was taken from previous studies of our group [47, 118]. Evaluation of the thickness of these additional layers was done by VIS ellipsometry after each grafting step during the synthesis procedure. For in situ IR-SE measurements the order of layers in the model was changed and the angle of incidence adjusted, shown in the scheme on the right in figure 4.2.

The simulation itself is an iterative best-fit procedure. The oscillator values (frequency, amplitude, width) are varied to obtain the best fit between measured and simulated spectrum. From the final simulation the sample parameters can be extracted, such as layer thickness d, refractive index n, absorption coefficient k.

Chapter 5

Results and Discussion

The experiments in this work are focused on two different types of thermoresponsive polymer brushes. One type was prepared from POx made of either cyclopropyl-2-oxazoline or methyl-2-oxazoline monomers as well as statistical copolymers of the two. The other type of brushes was synthesised from block-copolymers made of PNIPAAm and the anchoring polymer PGMA. All brushes were prepared via the grafting-to method. In situ experiments were performed on both types of brushes to gain information about their swelling degree and functional behavior in water upon application of the temperature stimulus. Additionally, they were compared to the well-studied behavior of traditional PNIPAAm brushes in water.

IR-SE studies were used to probe optical characteristics of the various brushes and films at the brush–air and brush–water interface. Spectra are discussed with respect to specific vibrational bands and interpreted via optical simulations. Frequency and band shape provide valuable insights into the interactions of the functional groups with other molecules in close proximity. Changes in the environment induce changes of the interactions, which are visible in the spectra. An example for such interactions are hydrogen bonds (see figure 2.2 on page 9).

With the interpretation of vibrational bands and their changes in the IR spectra one can deduce certain mechanisms, such as thermo-responsive switching between a hydrophilic and hydrophobic state which is the prominent characteristic of PNIPAAm and POx. Other possible mechanisms are pH-dependent dissociation of functional groups [10] or a solvent-induced change of polymer properties [67]. Since the ν(C=O) band is the most prominent band, takes part in hydrogen bonding, and is present in both PNIPAAm and POx, it was used in these studies as marker for thermo-responsive changes of the interactions between polymer and water.

The detailed results of IR-SE and complementary methods (VIS ellipsometry and AFM) are presented in this chapter. VIS ellipsometry measurements and optical modeling were used to determine total layer thickness, water content and refractive index of the brushes. AFM scans were evaluated to estimate surface roughness and sample homogeneity. Additionally, in situ AFM measurements were made on some samples with the scratch method to determine brush layer thickness in swollen and collapsed state. The first section deals with the experiments on POx brushes followed in the second section by the results on brushes from PNIPAAm-*b*-PGMA copolymers. Both sections include a comparison to literature studies of the well-known PNIPAAm grafting-to brushes. The last section deals with protein experiments on silicon, PGMA, and PNIPAAm-*b*-PGMA brushes and an outlook to further studies as well as possible applications.

5.1 Poly(2-alkyl-2-oxazoline)s

In situ IR-SE was applied to characterize the thermoresponsive behavior of POx brush films consisting of either pure P*c*PrOx or statistical copolymers containing *c*PrOx and MeOx. Two different copolymers were used, with a composition of either 90% *c*PrOx and 10% MeOx or 75% *c*PrOx and 25% MeOx (see section 4.2.1). Additionally, a pure PMeOx brush—that shows no temperature sensitivity—was studied for comparison.

The section begins with a characterization of thicker layers of the polymers as well as the brushes, both in dry state, and simulations to determine their optical constants. Afterwards, the temperature-dependent sensitivity of the brushes in water is described, which was monitored via the characteristic amide I vibrational band positioned at 1650–1600 cm^{-1}. This band is a direct measure for changes in polymer–water interactions since its frequency shifts when N–C=O groups are involved in hydrogen bonding. Besides the qualitative evaluation of the in situ spectra, simulations on the amide I band were performed in order to gain some quantitative results about the interactions within the brushes.

5.1.1 Characterization in dry state

IR-SE was first applied ex situ on three spin-coated POx layers on gold as well as on the four POx brushes on silicon (see table 4.4). Evaluation of the obtained tanΨ spectra involved vibrational band assignments as well as optical simulations, including dry-state oscillators in the range of the amide I band, to characterize the pure P*c*PrOx and PMeOx layers. The simulation results could then be used to model the copolymer samples and determine their composition.

IR-SE spectra of POx layers on gold substrates

In the upper panel of figure 5.1 tanΨ spectra of the spin-coated polymer layers on gold are displayed. All bands in these spectra can be assigned to POx since no PGMA anchoring layer is present on those samples. One can clearly identify the strong amide I mode situated at 1660–1650 cm^{-1} which is mainly composed of the C=O stretching vibration. This band is positioned at highest frequency for PMeOx (1660 cm^{-1}) and shifts to lower frequencies with increasing content of P*c*PrOx, down to 1650 cm^{-1} for the pure P*c*PrOx. The shift might be due to the electron withdrawing effect of the cyclopropyl group compared to the methyl group [31].

POx are tertiary amides, meaning there is no N−H group in their structure (see figure 2.1). This leads to the absence of an amide II band in the IR spectra that would otherwise appear around 1550 cm^{-1}. Without this N−H group, and without the presence of any other hydrogen-donating groups in POx, no intramolecular hydrogen bond interactions between C=O and such groups are possible. Therefore the measured ν(C=O) band of dry polyoxazolines corresponds to free, that is, non-interacting carbonyl groups.

Second derivatives of the POx tanΨ spectra however, reveal two components within the C=O stretching mode, a very intense one at 1662–1652 cm^{-1} and another weak one at lower wavenumbers (see lower panel in figure 5.1). The low-intensity component might be due to the formation of very weak hydrogen bonds between C=O and C–H groups [119, 120], generally lowering the frequency of stretching vibrations, such as

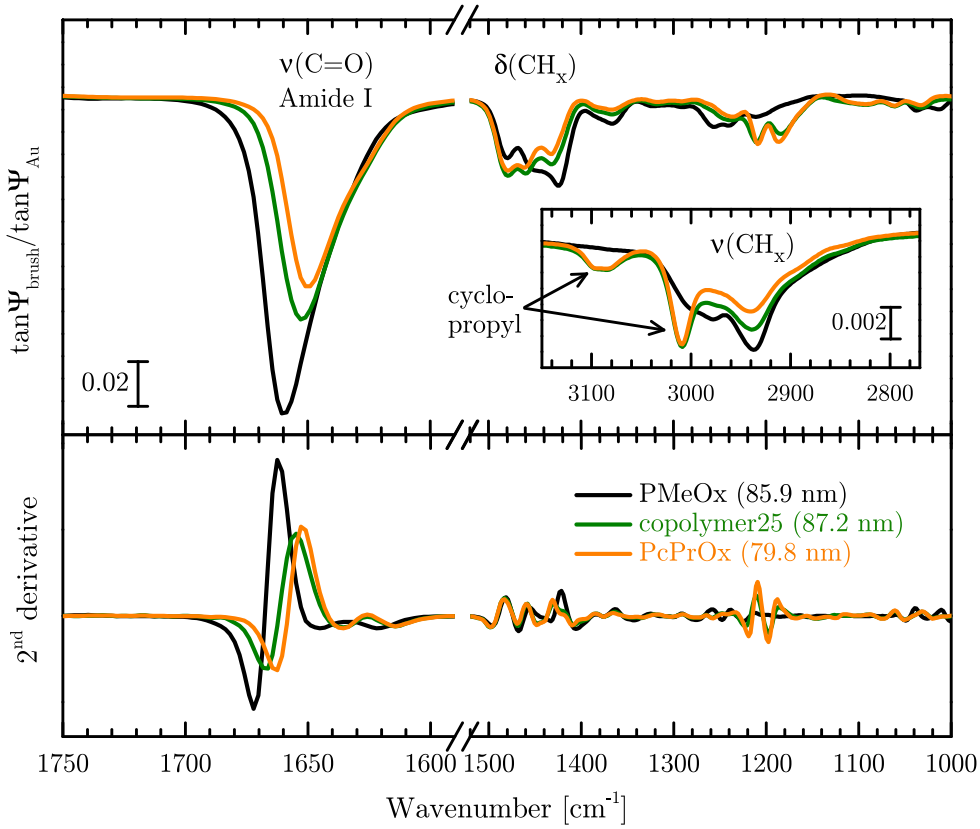

FIGURE 5.1: Ex situ tanΨ spectra (top) and their second derivatives (bottom) of spin-coated POx layers on gold. Dry layer thicknesses were determined with VIS ellipsometry and are given in the legend (values in brackets).

TABLE 5.1: Band Assignments of dry POx brushes. Only the frequencies of the two pure brushes P*c*PrOx and PMeOx are listed.

Frequency [cm^{-1}]		Assignment	Reference
P*c*PrOx	PMeOx		
3098–3080		ν CH_x (cyclopropyl)	[122, 123]
3009		ν CH_x (cyclopropyl)	[122, 123]
	3000	ν_{as} CH_3	[123]
	2978	ν_{as} CH_3	[87]
2940	2938	ν_{as} CH_2	[87]
2900–2820		ν_s CH_2 and ν_{as} CH_3	[123, 124]
1650	1660	ν C=O	[123, 125]
1479, 1460	1480	δ_{as} CH_x	[123, 125, 126]
	1451	δ_{as} CH_x	[123, 125, 126]
1432	1424	δ_{as} CH_x	[123, 125, 126]
1383	1382	δ_s CH_x	[123, 126]
1367	1366	δ_s CH_x	[123]
1317	1323	skeletal C–C	[125]
1291	1290	skeletal C–C	[125]
1236	1256, 1240	skeletal C–C	[125]
1208	1211	skeletal C–C	[125]
1186		skeletal C–C	[125]

ν(C=O). Additionally, short-range interactions between the polymer segments can cause asymmetric line broadening [121].
The range of the bending modes $\delta(CH_x)$ at 1500–1400 cm^{-1} shows three components for each POx. Two of these are at similar positions for all POx samples, situated around 1480 cm^{-1} and 1460 cm^{-1}. They could be attributed to CH_x bending modes within the backbone. The third component appears around 1432 cm^{-1} for the layers containing *c*PrOx and at lower frequency (1424 cm^{-1}) for the PMeOx layer. Due to the different frequency, this band could be assigned to vibrations of the cyclopropyl ring and the CH_3 group, respectively.

In the inset of figure 5.1 tanΨ spectra in the range of the stretcing modes are displayed. A common feature is the asymmetric $\nu(CH_x)$ mode at ~2940 cm^{-1} which is assigned to CH_2 groups of the backbone. The other bands differ strongly between PMeOx and the samples containing P*c*PrOx: Around 2980 cm^{-1} the asymmetric CH_3 stretching mode is visible in the PMeOx spectrum. The spectra of P*c*PrOx and copolymer25 show a broad band around 3098–3080 cm^{-1} and another one at 3009 cm^{-1} which can be assigned to the CH_2 stretching modes of the cyclopropyl ring. These are present at higher frequencies than the backbone $\nu(CH_2)$ modes due to cyclic stress. A list of all band assignments is given in table 5.1.

Simulations of POx on gold substrates

For simulations of tanΨ spectra of ~80 nm POx layers on gold, an optical layer model consisting of Au/Polymer/Air (see figure 4.2a) was used in the software SpectraRay/3. Reference data for gold was taken from Rakić [127]. The polymer layer was modeled using a Brendel oscillator layer (see equation 4.6 in section 4.3). Values for ε_∞ and layer thickness were taken from VIS ellipsometry results, which were $\varepsilon_\infty = 2.301$ and d = 79.8 nm (P*c*PrOx) and $\varepsilon_\infty = 2.262$ and d = 85.9 nm (PMeOx).

The initial values for the oscillators of the polymer layer were based on the information gained from measured tanΨ spectra and their second-derivative spectra. A visual approximation was performed manually. Afterwards, resonance frequency (ν_0), strength (ν_P), and line width (σ) for each oscillator could be fitted via the least-squares method, selecting a proper fitting interval for each value to obtain physically meaningful results.

The obtained simulated spectra as well as the corrected measured data of P*c*PrOx and PMeOx are displayed in the top and middle panels of figure 5.2. From these simulations the n,k-data for each polymer was calculated and used to build a new layer. This layer was based on a modified effective medium approximation (EMA) [117] using a mixture of P*c*PrOx and PMeOx. The EMA layer served as polymer layer in the model of the copolymer to fit its thickness and composition. Measured and simulated spectra of copolymer25 are shown in the bottom panel of figure 5.2.

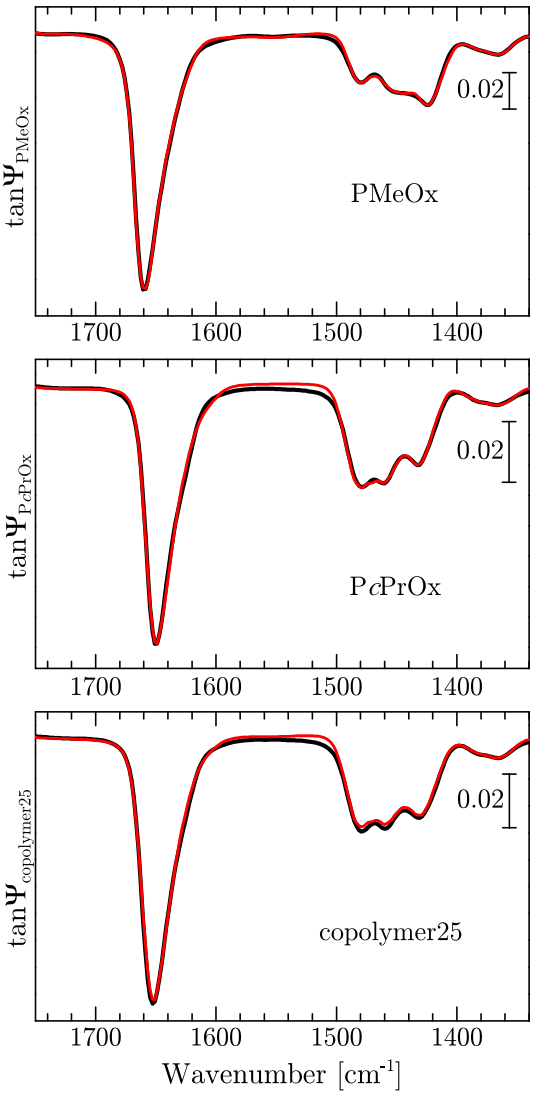

FIGURE 5.2: Measured (black) and simulated (red) tanΨ spectra of the POx layers on gold in the fingerprint range. From top to bottom: PMeOx, P*c*PrOx, copolymer25.

The fit resulted in d = (86±1) nm and (25±5)% MeOx. There is a slight difference to the thickness and MeOx content determined with VIS ellipsometry on copolymer25 (d = (87.2±0.3) nm and (30±5)% MeOx), which can be correlated to the different environmental conditions: VIS ellipsometry was performed in ambient atmosphere at ~30% relative humidity. In this state the POx layers are slightly swollen due to hydration by water vapor, especially the hydrophilic MeOx units. IR-SE spectra were recorded in dry atmosphere (<0.1% relative humidity). Under these conditions the layer thickness is lower. In the simulation it is assumed that no polymer–polymer interactions between MeOx and *c*PrOx units are present. The successful simulation of the copolymer indicates the absence of any interactions that involve the C=O groups.

IR-SE spectra on silicon

Similar ex situ measurements as those of the layers on gold were performed of the four different POx brushes on silicon. The resulting tanΨ spectra, including a spectrum of the PGMA anchoring layer, are displayed in the upper panel of figure 5.3. In these spectra, the presence of the PGMA anchoring layer is visible via additional bands. Most prominent is PGMA's C=O band at ~1735 cm^{-1}, which is identical for all POx

samples, indicating that the anchoring layer is not influenced by the chemistry of the brush toplayers. There is also no overlap of the ν(C=O)$_{PGMA}$ or other PGMA bands with the ν(C=O)$_{POx}$ band, because the latter is located at much lower wavenumbers due to mesomeric effects within the N–C=O groups [128]. This is very important for further band analysis of in situ spectra. Similar to the C=O band of the thicker layers on gold (lower panel in figure 5.3), the C=O band of the POx brushes on silicon is positioned between 1659 cm^{-1} and 1651 cm^{-1} with the highest frequency for PMeOx and a shift to lower wavenumbers with increasing P*c*PrOx content. While the C=O band position is the same on silicon and gold for PMeOx (1659 cm^{-1}), the samples of P*c*PrOx and copolymer25 on silicon show a C=O frequency that is increased by 1-2 cm^{-1}.

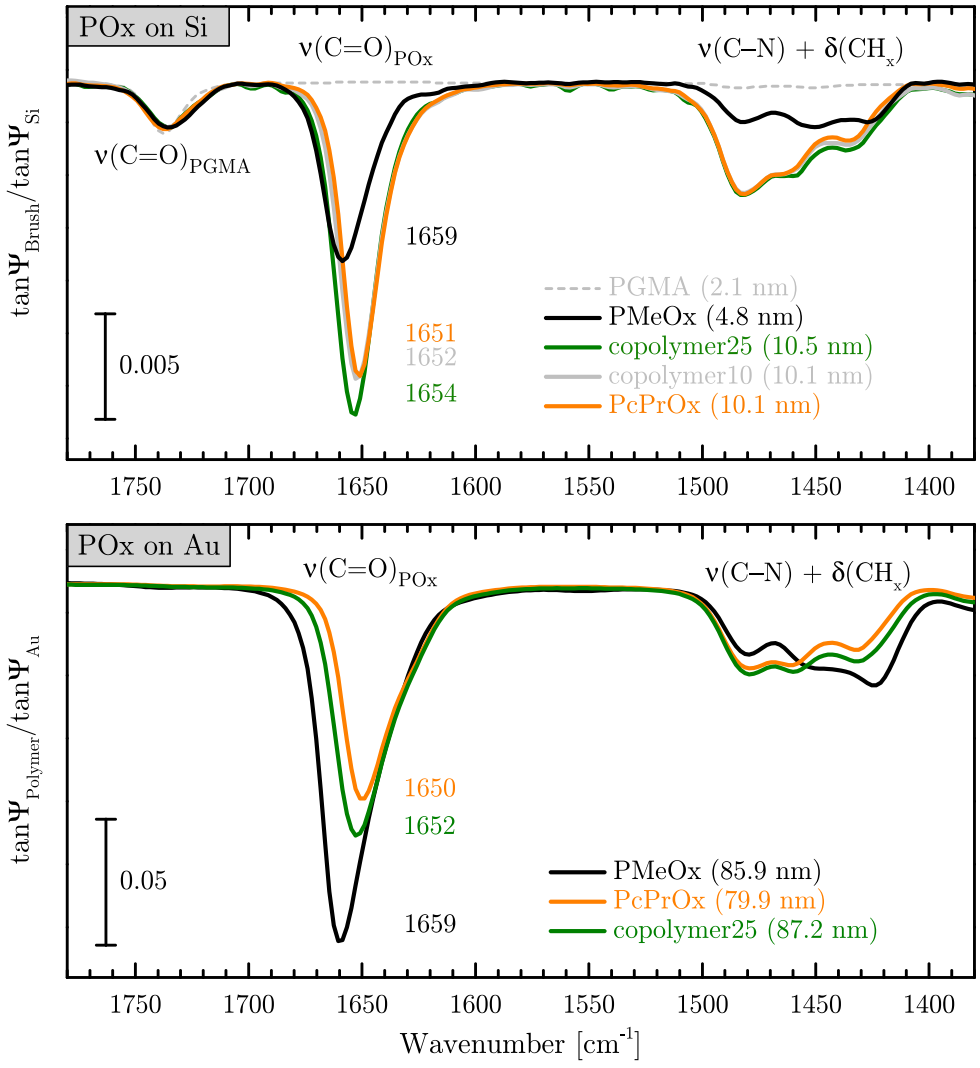

FIGURE 5.3: Measured and simulated ex situ tanΨ spectra of POx brushes on silicon (upper panel) and POx layers on gold (lower panel). Spectra were recorded at 65° angle of incidence and referenced to tanΨ$_{ref}$ of a clean substrate under the same conditions. Values printed in brackets are the dry layer thicknesses determined with VIS ellipsometry under ambient conditions.

The region around 1500–1400 cm^{-1} is slightly overlapped by two PGMA bands, which are located at approximately 1485 cm^{-1} and 1450 cm^{-1} [47]. However, these PGMA bands have a weak intensity and can be neglected in further band analysis. For clarification, a simulated tanΨ spectrum of a 2.1 nm thin PGMA layer has been added to figure 5.3. The observed ν(C=O)$_{POx}$ band shapes are similar to those of the thicker layers on gold, but the band width and intensity is larger on gold due to increased layer thickness. There are also differences in the range of the ν(C−N) and $\delta(CH_x)$ bands. For example, in the spectrum of PMeOx on silicon the three visible bands have similar intensity, while in the spectrum of PMeOx on gold the band around 1423 cm^{-1} is the most intense. Comparing the spectra of the other POx samples, it can be seen that the band around 1481 cm^{-1} is of higher intensity on silicon. A possible reason for the observed discrepancies is the different structure of the layers. On silicon, there is the additional PGMA anchoring layer between substrate and the POx brushes. On gold however, there is no PGMA layer and the POx chains have only been spin-coated onto the substrate without the formation of brushes. Therefore, PGMA–POx interactions are possible for the samples on silicon, but not for those on gold.

Simulation of POx on silicon

A simulation—similar to the one of the samples on gold—has been performed with the POx brush layers on silicon. For this the optical model needed to be changed to the different substrate. Additionally, the brush layer system comprises a native silicon oxide layer and a thin PGMA anchoring layer, resulting in a layer system of Si/SiO_2/PGMA/Polymer/Air (see figure 4.2). The substrate bulk layer was changed to a silicon n,k-layer with n = 3.42 and k = 0 [129]. A 1.6 nm native silicon oxide layer [118] and a PGMA layer [47] were added using datasets established in previous studies of our group. PGMA layer thickness was set to d = 2.1 nm and n_∞ = 1.525 according to results of VIS ellipsometry measurements. The POx layer parameters were also set to the values determined with VIS ellipsometry. Since the band positions were not exactly the same in the samples on gold and on silicon, oscillator parameters were adjusted in analogy to the procedure on gold. From these results, the n,k-data was exported and used to create an EMA layer in the optical model. The copolymer layers were fitted with this layer, only leaving thickness and MeOx volume fraction as open fit parameters. Results of the simulations are given in figure 5.4. Thickness and MeOx fraction in the copolymer samples resulted in d = (10.3 ± 0.5) nm and (15 ± 6)% MeOx for copolymer10 and d = (11.2 ± 0.5) nm and (30 ± 7)% MeOx for copolymer25.

An interesting observation is made comparing the C=O band of the PGMA layer in measured and simulated spectra. In all four POx samples—most prominent in PMeOx—the measured C=O band is broader than the simulated one and slightly shifted to lower wavenumbers. This can be explained by Van-der-Waals interactions between POx and PGMA in the interfacial region between the two layers. An improved model would include an interpenetration layer between the two polymers, because the carboxy-terminated polymer chains partly diffuse into the PGMA layer during annealing to react with epoxy groups within. Likewise, some loops and tails of the PGMA chains can move towards the reactive chain ends of the brush polymer. Since PMeOx has the highest grafting density, its interactions with the PGMA layer are larger and therefore it shows the strongest ν(C=O)$_{PGMA}$ band broadening in its spectrum. In literature, this penetration into the anchoring layer has been proven by comparing grafting densities of polymer chains attached to substrates covered with either a 1 nm thin PGMA layer [60]

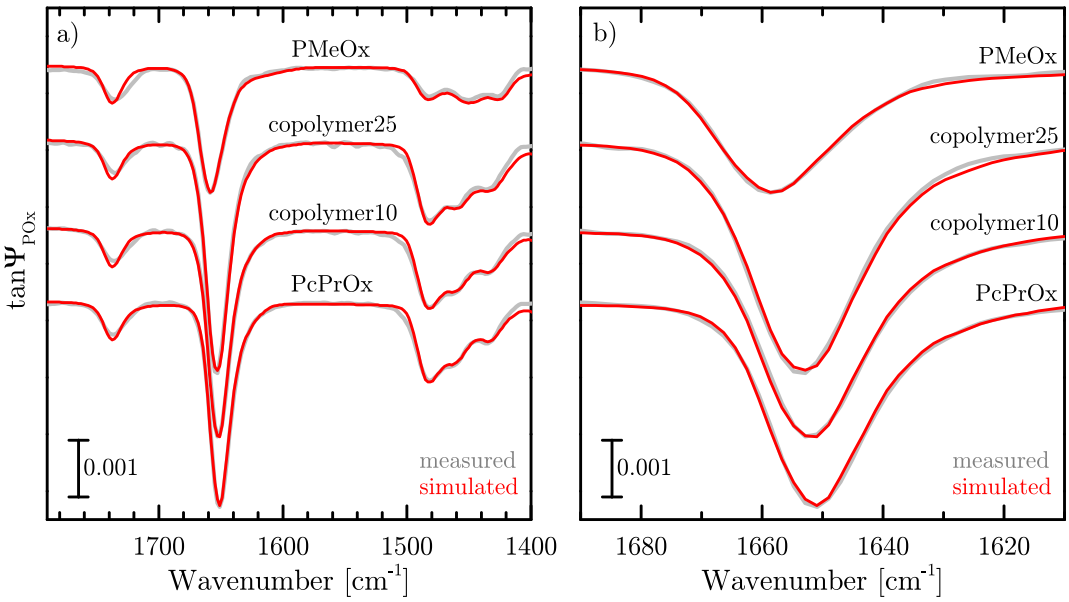

FIGURE 5.4: Ex situ measured (grey) and simulated (red) tanΨ spectra of dry POx brushes on silicon in a) the fingerprint range and b) zoomed into the range of the ν(C=O) mode. All spectra were recorded at 65° angle of incidence and corrected as described in section 4.3.1. Spectra are y-shifted for better visualization.

or only an epoxysilane monolayer [130, 131]. It turned out that a higher grafting density can be achieved with a polymeric anchoring layer due to the possibility of interpenetration, increasing the accessibility of epoxy groups for covalent attachment.

5.1.2 In situ swelling behavior

This section deals with the stimuli-responsive behavior of POx in water. First, a summary of the temperature-induced transition of the respective POx chains in solution is given. These data were collected and analyzed by Stefan Adam at IPF Dresden [108, 111]. It is followed by the in situ behavior of the brush layers, studied by IR ellipsometry and VIS ellipsometry. While VIS ellipsometry can access the swollen layer thickness and water content of the brushes via an optical layer model [13, 28], the IR spectra provide valuable information about functional groups and interactions between the groups or with a surrounding medium [132]. In the case of POx the interactions between the carbonyl group and water are of great interest. Therefore, in the spectral interpretation and simulation the focus was put on the carbonyl stretching mode, $\nu(C{=}O)_{POx}$, around 1650 cm^{-1}.

Transition of POx chains in water

The transition behavior of the synthesized POx chains in aqueous solutions was studied via turbidity measurements to determine their clouding points (see table 4.3 in section 4.2). All samples showed a sharp and reversible transition behavior in water without significant hysteresis, similar to the results on other POx presented in literature [30, 85, 87]. Copolymerization of *c*PrOx with the non-responsive, hydrophilic MeOx resulted in an increased LCST compared to pure P*c*PrOx due to the increased hydrophilicity of

the chains. Accordingly, the highest LCST was determined for the copolymer with the largest fraction of MeOx (25%) [111].

There is also a concentration-dependence of the cloud points according to type I Flory-Huggins miscibility behavior: Upon increasing chain length of a polymer its critcal point shifts to lower concentration [133]. In other words, at constant chain length and increasing concentration the cloud point shifts to lower temperatures. This observation is supported by Bloksma et al. [31], who found the same dependence on concentration and chain length of P*c*PrOx in solution. For the POx studied in this work, the trend is non-linear. Up to a concentration of 10 mg/ml the decrease of cloud point is very strong. It levels off at higher concentrations until an almost steady value is reached at 30–50 mg/ml [108, 111]. As there occurred only a minor decrease of the cloud point from 30 to 50 mg/ml, the values at 50 mg/ml could be assumed for concentrated solutions and even for thin layers. These values are 18 °C, 22.7 °C, and 29.4 °C for P*c*PrOx, copolymer10, and copolymer25, respectively.

Transition of POx brushes in water

Knowing the transition behavior of POx *chains* in solution we were now interested in the characteristics of the prepared *brushes* in contact with water and their response to a change in temperature. This was studied with in situ VIS and IR ellipsometry. Most of the qualitative analysis and discussion described in this section has already been published [134].

In situ experiments in the infrared range were analyzed predominantly in the range of the ν(C=O)$_{POx}$ stretching mode at approximately 1650 cm^{-1}. This region is partly overlapped by the bending mode of water, which arises as a broad band in the range of 1700–1600 cm^{-1}. In heavy water, this band is positioned around 1250–1150 cm^{-1}, leaving the ν(C=O) region free from overlapping contributions [135]. Therefore, additional measurements in heavy water were performed and enabled an unambiguous interpretation of the ν(C=O)$_{POx}$ band.

In dry state the ν(C=O) frequency of POx brushes was determined at 1660–1650 cm^{-1} (section 5.1.1). Placing the samples in cold water causes a significant redshift of the frequency to approximately 1610 cm^{-1}, displayed in the blue and green graphs of figure 5.5. This shift is caused by the formation of hydrogen bonds between C=O groups and water molecules, resulting in reduced electron density (reduced double bond character) of the C=O bond [128]. Figure 5.5 also displays the spectra of POx in their collapsed state at 45 °C (red graphs). In this state, the ν(C=O) band is shifted back to slightly higher wavenumbers compared to the swollen state at 20–25 °C, which is due to a partial loss of hydrogen bonds. Here it can clearly be seen that PMeOx does not show any temperature sensitivity. Its spectra at 20 °C and 45 °C overlap. The other three POx, containing different amounts of *c*PrOx, show temperature-responsive behavior, which is strongest for the pure P*c*PrOx brush. In detail, the band maximum in P*c*PrOx, copolymer10 and copolymer25 shifts from 1608 to 1619 cm^{-1}, from 1610 to 1618 cm^{-1}, and from 1608 to 1615 cm^{-1}, respectively, resulting in a decreasing frequency shift from 11 cm^{-1} in P*c*PrOx to 7–8 cm^{-1} in the copolymers.

The overall ν(C=O) band shapes of P*c*PrOx and the copolymers in figure 5.5 indicate that the band envelope comprises several components related to different hydration states. However, the ν(C=O) band is also overlapped by the downward-pointing δ(H_2O) mode of water around 1650 cm^{-1}, which might obscure the total band shift of the carbonyl

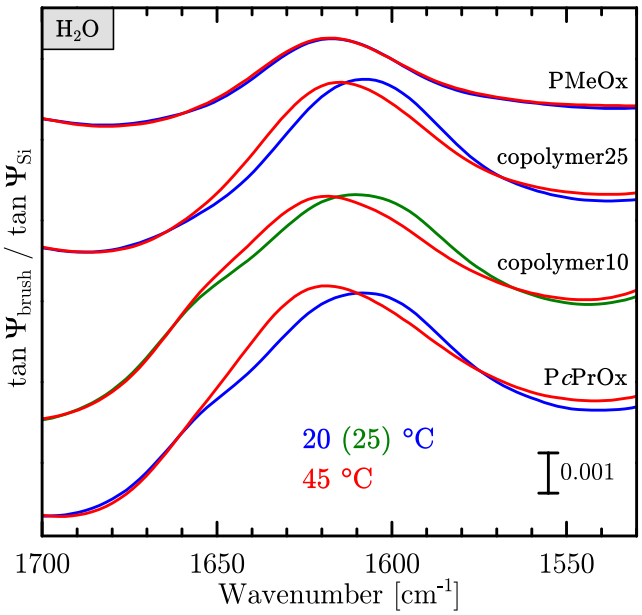

FIGURE 5.5: In situ tanΨ spectra of POx brushes in H_2O at low and high temperature in the range of the carbonyl band. Measurements at low temperature were mostly performed at 20 °C, except copolymer10, which was measured at 25 °C. Spectra were recorded at steady temperature and referenced to $\tan\Psi_{Si}$ of a clean silicon wedge under the same conditions.

mode. In order to identify the switching behavior more unambiguously, measurements were performed in H_2O and additionally in D_2O. The band related to the bending vibration of heavy water occurs at ~1215 cm^{-1}, thus allowing for a clear analysis of the ν(C=O) band components. Figure 5.6 shows in situ IR-SE spectra of the two temperature-responsive P*c*PrOx and copolymer25 polyoxazoline brushes in water and heavy water in the spectral region of the ν(C=O) band. Additionally, second-derivative spectra are plotted to reveal components within the carbonyl bands.

The spectra in H_2O (top panels in figure 5.6) were recorded at temperatures between 20–45 °C in 5 °C steps. The P*c*PrOx homopolymer brush shows three distinct components around 1657, 1620–1625, and 1600 cm^{-1}. The first one is close to the position that was determined for free C=O in dry state. The other two components are at much lower wavenumbers, indicating two different states of hydrogen bonding of the C=O groups in the brush. Since the oxygen atom can form two hydrogen bonds with water due to its two free electron pairs, the component at 1625–1620 cm^{-1} is assigned to C=O groups involved in one hydrogen bond (weakly hydrated) and the other component around 1600 cm^{-1} to those involved in two hydrogen bonds (strongly hydrated). The weakly hydrated component also arises in swollen state, probably because complete C=O hydration is inhibited by steric hindrance effects of the polymer chains [136].

With increasing temperature, the strongly hydrated component decreases and the weakly hydrated component increases. This transformation of the polymer–water interactions is related to the brush turning from hydrophilic to more hydrophobic. On a molecular level it can be understood that one of the hydrogen bonds to the strongly hydrated C=O groups breaks, resulting in a higher number of weakly hydrated C=O groups and a smaller number of strongly hydrated ones. Note again that P*c*PrOx is a tertiary amide that does not allow for intramolecular hydrogen bonding between neighboring monomer units. This is contrary to secondary amides like PNIPAAm,

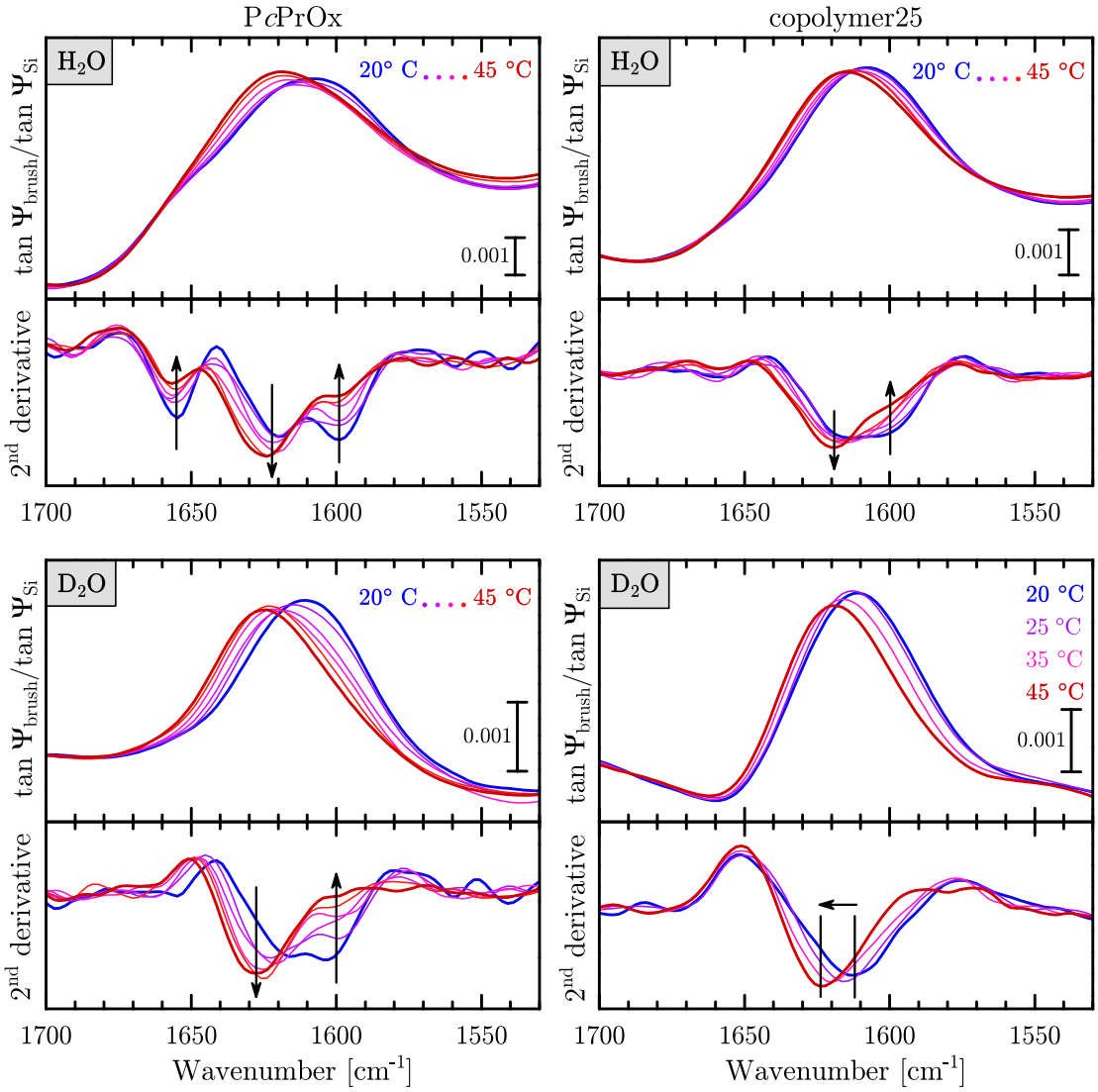

FIGURE 5.6: Temperature-dependent in situ tanΨ spectra of POx and their second derivatives in the range of the ν(C=O) vibration. Top: POx in H_2O, Bottom: POx in D_2O, Left: P*c*PrOx, Right: copolymer25.

TABLE 5.2: Thicknesses, H_2O volume fraction, and swelling degrees of POx brushes determined via in situ VIS ellipsometry.

Polymer	Thickness d [nm]			H_2O [vol. %]		swelling degree [%]	
	dry	20 °C	45 °C	20 °C	45 °C	d_{20}/d_{dry}	d_{45}/d_{dry}
P*c*PrOx	8.5 ± 0.1	20.2 ± 0.5	14.0 ± 0.5	52 ± 3	32 ± 3	240 ± 5	160 ± 5
copolymer10	8.9 ± 0.1	24.3 ± 0.5	15.3 ± 0.5	61 ± 3	38 ± 3	270 ± 10	170 ± 10
copolymer25	9.4 ± 0.1	32.4 ± 0.5	20.4 ± 0.5	69 ± 3	51 ± 3	340 ± 10	220 ± 10
PMeOx	4.0 ± 0.1	9.0 ± 0.7	14.1 ± 0.7	49 ± 5	69 ± 5	225 ± 20	350 ± 20

which exhibit additional vibrational bands associated with H—N interacting with C=O groups [71, 75].

Interestingly, the component assigned to the free C=O group at 1655 cm^{-1} also diminishes at higher temperatures. This is not expected, because a loss of water in the brush would rather correlate with an increase of free C=O groups. The signal decrease is more likely due to the overlapping contribution of the water-bending vibration at 1650 cm^{-1}. Since no 1655 cm^{-1} component is observed for P*c*PrOx in D_2O (figure 5.6, bottom left), it is possible that $\delta(H_2O)$ is the major contribution to the 1655 cm^{-1} component of the spectra in H_2O. Its change in intensity could then be related to the change in water content and thickness of the collapsing brush.

The ν(C=O) band of the copolymers in H_2O, for example copolymer25 in figure 5.6, top right, only displays two major components in its second derivatives, namely the weakly and strongly hydrated ones around 1619 cm^{-1} and 1600 cm^{-1}, respectively. This shows that all C=O groups are involved in hydrogen bonding. The brushes are more hydrophilic owing to the incorporation of MeOx in the copolymers, leading to a higher water content compared to the pure P*c*PrOx brush, which is in agreement with in situ VIS ellipsometry measurements (see table 5.2). However, the temperature-responsive change of the distribution between weakly and strongly hydrated C=O groups is smaller in the copolymers than for P*c*PrOx. This observation will be discussed shortly.

In situ measurements of P*c*PrOx and the copolymer25 brush in heavy water (figure 5.6, bottom panels) show that the deswelling behavior takes place gradually and is stretched over the entire measured temperature range. This is in contrast to the abrupt phase transition of poly(2-oxazoline)s in solution [85, 87, 111], and also to PNIPAAm, which shows a fast transition around the LCST both in solution [71] and in the form of brushes [16, 28].

For P*c*PrOx in D_2O (figure 5.6, bottom left), two hydrated carbonyl stretching components are measured at 1618–1628 cm^{-1} and 1600 cm^{-1}. While the strongly hydrated component at 1600 cm^{-1} clearly decreases with increasing temperature, the other component increases and seems to shift from 1618 cm^{-1} at 20 °C to 1628 cm^{-1} at 45 °C. A possible explanation for this shift is a gradual change from a state of hydrogen bonding with water molecules that are bound to other water molecules, to a state of hydrogen bonding with water molecules forming a bridge between two C=O groups. Formation of the latter could be a result of interchain association and steric hindrance within the brush layer [32]. For P*i*PrOx in solution, the frequency of the bridging hydrogen bonds is supposed to be around 1630 cm^{-1} [32, 87] which is close to the observed 1628 cm^{-1} position for P*c*PrOx.

For copolymer25 this shift of the components is more strongly pronounced. Its second derivative spectra in D_2O (figure 5.6, bottom right) do not show two components anymore but only one broad component, which gradually shifts from ~1612 cm^{-1} to ~1624 cm^{-1} upon increasing temperature. The shift still indicates a transition from a strongly hydrated state of the brush around room temperature to a lesser hydrated one at higher temperatures, but the separation of the two bands in the second derivative spectrum is overlapped by the presence of many bands of intermediate states, including bridging water molecules. Again, the copolymer brush is more strongly hydrated than the P*c*PrOx homopolymer brush due to incorporation of hydrophilic MeOx units. The total change of its ν(C=O) frequency at increasing temperature is smaller, partially due to an overlap with the additional ν(C=O) components of MeOx units which stay unchanged upon increasing temperature. Although there is no VIS ellipsometry data available of the thickness and water content of the brushes in D_2O, the swelling behavior

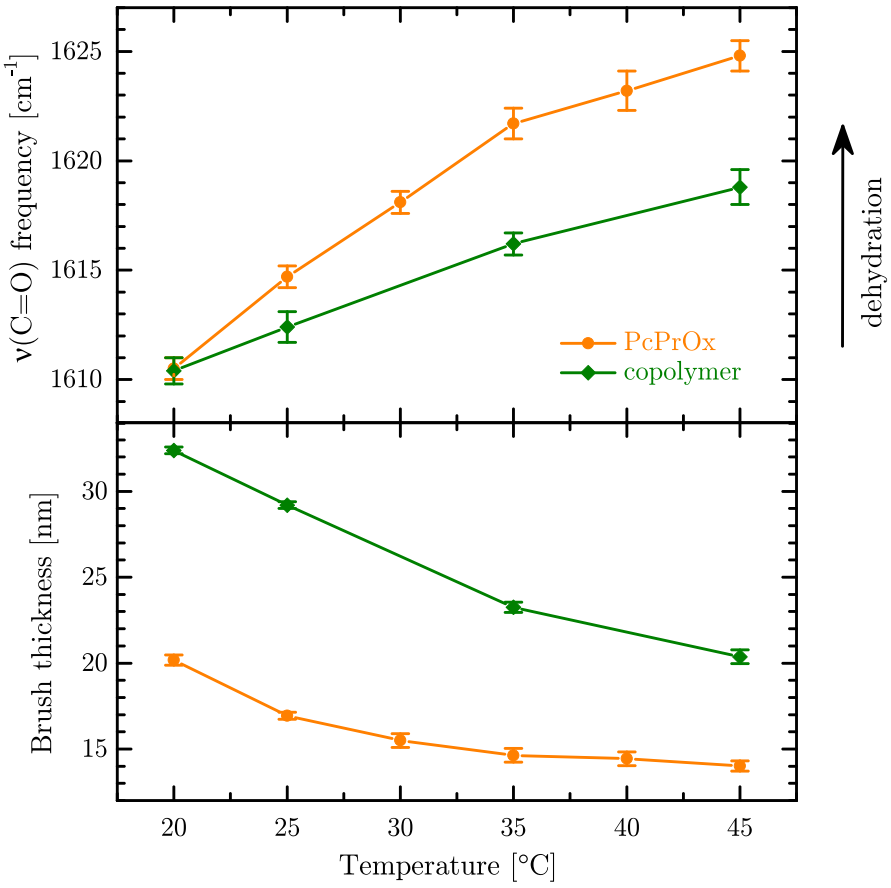

FIGURE 5.7: Plot of the temperature-dependent ν(C=O) frequency (top) of P*c*PrOx and copolymer25 in D_2O in the in situ tanΨ spectra compared to the swollen thickness (bottom) determined with VIS ellipsometry in H_2O. Corresponding swelling degrees to the brush thickness at 20 °C and 45 °C are 240% and 190% (P*c*PrOx) and 345% and 220% (copolymer25).

can be assumed to be similar to the results of swelling experiments in normal water.

A comparison between the ν(C=O) frequency shift measured in the infrared and the total change in water content of the brushes measured in the visible range is visualized in figure 5.7. In IR spectra the transition of the brush can be followed via the frequency shift of certain functional groups, in this case via the ν(C=O) band (top panel). In VIS ellipsometry the swollen brush thickness is a quantity that gives complementary information about the switching behavior (lower panel). However, the total value of swollen brush thickness is dependent on the dry thickness and cannot be directly compared between the two brushes. To be able to do so, we calculated the swelling degree (ratio between dry and swollen thickness, in percent) of the two brushes at 20 °C and 45 °C. The resulting values are 240% and 190% for P*c*PrOx and 345% and 220% for copolymer25, respectively.

As mentioned before, for the POx samples we observed different results from the two techniques: While in IR-SE the frequency difference between lowest and highest temperature is greater for the P*c*PrOx brush, VIS ellipsometry results show a larger difference in swelling degree (and water content) in the copolymer brush.

Note that despite their different swelling degree in the hydrated state at 20 °C the

ν(C=O) frequency of both P*c*PrOx and copolymer25 is at the same position (1610 cm^{-1}). This indicates similar hydration states of the brushes' C=O groups. A possible reason is that, due to the stronger hydrophilicity of the copolymer brush, more water is present in the layer. This additional water does not interact with the polymer, but causes a higher swelling degree and a different behavior of molecular interactions between polymer and water when the temperature is changed. While the transition of the pure P*c*PrOx brush can be followed clearly via the decrease of strongly hydrated C=O groups in favor of weakly hydrated ones, the transition of the copolymer brush is more blurred due to the overlap of different forms of interaction between C=O and water, such as bridging water molecules. Also there is a smaller fraction of the temperature-responsive *c*PrOx units in the copolymer25 brush compared to the homopolymer P*c*PrOx brush, leading to the observed frequency shift being smaller.

VIS ellipsometry results on the other hand indicate a greater change in water content and swelling degree of the copolymer brush. It has to be taken into account, that the two methods operate in different wavelength ranges and with different experimental set-ups. While in VIS ellipsometry the brush–solution interface is probed directly through the solution, in IR-SE the interface is probed through the substrate and the brush layer. Consequently the surface and its roughness is probed differently. This could have an effect on the results of the brush layer, especially in the swollen state when there is a smaller contrast between the refractive index of swollen brush and water. Additionally, different spot sizes were probed with the two methods. In IR-SE, an area of about 1 cm^2 is probed, while in VIS ellipsometry the area is in the range of mm^2 or less.

We conclude that in the copolymer there is a certain amount of additional water present that does not interact with C=O groups, therefore it does not take part in changes of C=O frequency. However, these water molecules still contribute to the overall swelling of the brush layer. The observed differences in swelling could be due to the different chain length of the polymers, from which the brushes have been prepared. A dependency of the swelling behavior on molecular weight, and consequently on grafting density, has been described in literature [28, 80, 113, 137] and for the present POx samples such a dependency is very likely. Copolymer25 has the longest chains (61.3 kg/mol), while P*c*PrOx chains are much shorter (48.4 kg/mol). Still, both polymers in hydrated state show the same IR frequency of the C=O band (figure 5.7). In contrast to the temperature-responsive brushes, the hydrophilic PMeOx brush—with a molecular weight of only 22.0 kg/mol and a higher grafting density—shows a ν(C=O) frequency of 1618 cm^{-1} in water (not shown in the graph). This indicates that PMeOx is not fully hydrated, even though it is the most hydrophilic of the three POx samples. The low molecular weight resulted in a much thinner PMeOx brush layer, which also influences the swelling behavior. One cannot define a single reason for the deviations in swelling behavior, because the parameters brush thickness, molecular weight, and grafting density are dependent on each other and influence the functional behavior of the brush.

Simulations of in situ POx spectra

Based on the simulations of ex situ tanΨ spectra in section 5.1.1, the optical model was adjusted to fit the in situ measurements (see figure 4.2 in section 4.3.3). The angle of incidence was adapted to $\sim 13.3°$ according to the geometry at the inner surface of the wedge. Measured spectra of the dry brushes in the empty in situ cell were corrected as described in section 4.3.1 to be able to simulate the spectra. In the model, oscillator parameters of the polymer layer as well as the angle of incidence were slightly adjusted to find the best fit between corrected measurement and simulation. These dry state

simulations of samples and reference in the in situ setup were needed for the data correction of the brush spectra in wet state according to equation 4.4 in section 4.3.1. Visualization of a measured, corrected, and simulated in situ tanΨ spectrum is given in figure 4.1.

For simulating in situ spectra, the wet state was included in the optical model, replacing the bottom layer (air) with bulk water. The necessary n,k-data of either H_2O or D_2O was established in an earlier work of our group [47]. The polymer layer and bulk water were combined in an EMA layer to model the swollen brush. This brush/water layer was assumed to be homogeneous, since the measurements were done at only one angle of incidence, which does not provide enough independent parameters to model a swollen brush profile.

Raw in situ spectra are largely dominated by the bulk water signal, which makes the contribution of the swollen brush layer almost invisible. For comparison with the measured in situ spectra, which are referenced to in situ spectra of a clean silicon wedge, reference spectra of the layer system Si/SiO_2/water were also simulated and applied on the simulated brush layer spectra.
The fitting procedure on the corrected tanΨ spectra was performed in several consecutive steps: The results obtained with in situ VIS ellipsometry for swollen layer thickness and water content of the brushes were used as starting values in the EMA layer. These variables as well as the angle of incidence of simulated sample and reference were slightly adjusted to find the best fit of the $\nu(H_2O/D_2O)$ band shape. This can be seen in figure 4.1 on page 29 at 3800–3300 cm^{-1}. After this fit, thickness and water content were fixed on the resulting values. Due to the correlation between the stretching and bending modes of water, the intensity and shape of the $\delta(H_2O/D_2O)$ band was fixed simultaneously. This is important because the $\delta(H_2O)$ band overlaps with the polymers' ν(C=O) band and it would be otherwise impossible to distinguish between the contribution of water and polymer in the simulation of the band. In the following step, oscillator parameters of the ν(C=O) band components were changed to the values in hydrated state. For this, the frequencies in the second derivative spectra were used as starting values. Three components were included in the C=O band, one each for free C=O, weakly hydrated, and strongly hydrated C=O groups. Starting values for oscillator strength and line width were estimated. The adjustment was performed until the best possible match between measurement and simulation was found.

Results of the fitting procedure on P*c*PrOx at high and low temperature, both in normal and heavy water, are presented in figure 5.8. In the spectrum in H_2O (left panel), the overlap of the ν(C=O) vibrational band with the broad, downward-pointing $\delta(H_2O)$ band at 1700–1650 cm^{-1} is clearly visible, which is not the case for D_2O (right panel). As a result, the observed maximum position of the band related to $\nu(C{=}O)_{POx}$ shifts to slightly lower wavenumbers in H_2O. While there are other possible reasons for this deviation, for example a stronger C=O$\cdots D_2O$ interaction compared to a C=O$\cdots H_2O$ hydrogen bond, it is concluded that the overlap is at least partly responsible for the band shift.

In H_2O the ν(C=O) band has been simulated with 3 components at 1654, 1624, and 1596 cm^{-1}, representing the vibrational modes of free, weakly hydrated, and strongly hydrated C=O groups. At 20 °C the simulation resulted in 14% free, 30% weakly, and 56% strongly hydrated components. At 45 °C there was an insufficient overlap in the range of the $\delta(H_2O)$ band, that resulted in an unsuccessful simulation using the same three components. The fit in figure 5.8 was made including an additional fourth component at 1607 cm^{-1} to represent intermediate hydration states of the transition from

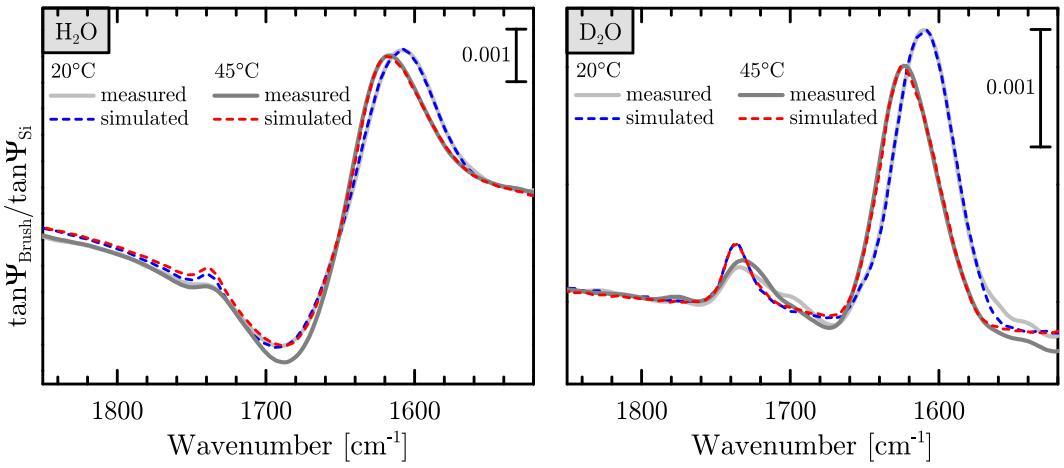

FIGURE 5.8: Measured (and corrected) in situ tanΨ spectra of P*c*PrOx in normal and heavy water at 20°C and 45°C (grey lines) as well as simulated spectra at the respective temperatures (blue and red dashes). Note the overlap of the ν(C=O) band with the downward-pointing H_2O bending mode in the left panel around 1700–1650 cm^{-1}, which is absent in the D_2O spectra shown in the right panel.

strongly to weakly hydrated C=O groups, for example bridging water molecules [32, 87]. However, we suspect this simulation can hardly be compared to the other simulations due to the additional component and the deviations in the range of the water band. Therefore it will not be further discussed.

In D_2O the simulation with three components was successful for both temperatures. At 20 °C the components were positioned at 1651, 1622, and 1596 cm^{-1}, again representing free, weakly hydrated, and strongly hydrated C=O groups. Simulation resulted in 6% free, 34% weakly hydrated, and 60% strongly hydrated C=O groups, indicating the main part of the band being comprised of the strongly hydrated component. Upon increasing temperature the two components representing hydrated carbonyl groups slightly shifted towards each other to 1625 cm^{-1} and 1602 cm^{-1}. Their intensity at 45 °C changed to an equal distribution, being 46% (weakly hydrated) and 48% (strongly hydrated), while the intensity of the free component stayed around 6%. Therefore, the amount of strongly hydrated C=O groups has diminished in favor of weakly hydrated ones.

In PMeOx (figure 5.9), neither a shift nor an additional component arises, since it is a non-responsive polymer. Its IR-SE spectra show only minor changes of the C=O band, their magnitude being in the range of spectral noise. Simulations of (corrected and smoothed) in situ PMeOx spectra at 20 °C and 45 °C reveal an steady contribution of the weakly hydrated component and a slight broadening of the strongly hydrated component, but the change is within error range ($\pm$ 2%). The amount of the free, weakly hydrated, and strongly hydrated component in the simulation resulted in 17%, 44%, and 39%, respectively. In situ VIS ellipsometry measurements on the other hand show a strong swelling of the PMeOx brush at increasing temperature. Its swelling degree changes from 225% at 20 °C to 350% at 45 °C (see table 5.2), indicating that more water penetrates the brush layer. Despite this change in swelling degree, water–polymer interactions in the PMeOx brush do not change. The additional water in the brush merely fills the space between polymer segments, which explains the behavior of the carbonyl band in the infrared.

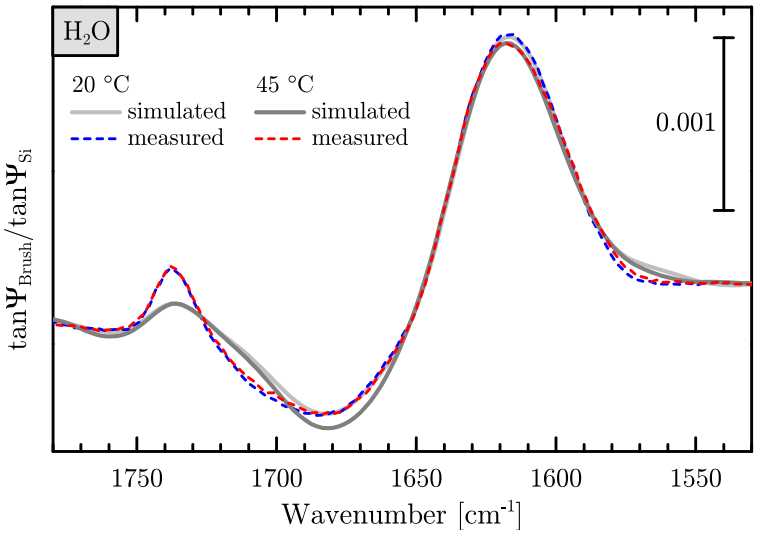

FIGURE 5.9: Measured (and corrected) in situ tanΨ spectra of PMeOx in normal water at 20°C and 45°C (grey lines) as well as simulated spectra at the respective temperatures (blue and red dashes). Note the overlap with the downward-pointing H_2O bending mode round 1700–1650 cm^{-1}. Spectra were smoothed with a cubic smoothing spline (λ=0.998) after the baseline correction.

Up to this point, the pure brushes P*c*PrOx and PMeOx have been successfully simulated in situ. Their n,k-data was extracted from the simulations and could be used to build a combined effective medium layer to represent the copolymers. The copolymer25 layer was initially modeled as an EMA with 25% MeOx and included as layer in the EMA of polymer and water. Swollen thickness and water content were taken from in situ VIS ellipsometry data, which are 32.5 nm and 70% vol. H_2O, respectively. A scheme of this modeled layer is depicted in figure 5.10.

The simulation revealed a good agreement of the water bands using the values for thickness and water content that had been obtained from VIS ellipsometry. Figure 5.11 shows the tanΨ spectrum of copolymer25 in H_2O at 20 °C, as well as two simulations

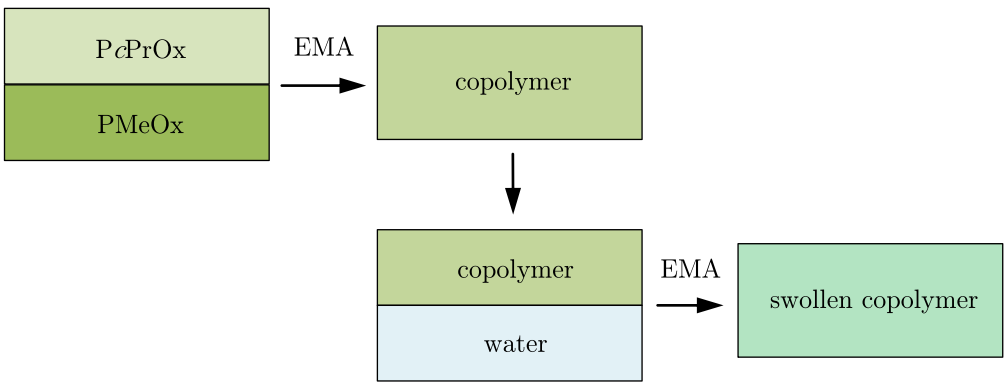

FIGURE 5.10: Combination of the data on P*c*PrOx and PMeOx to create a model layer for the swollen copolymer brush using the effective medium approximation.

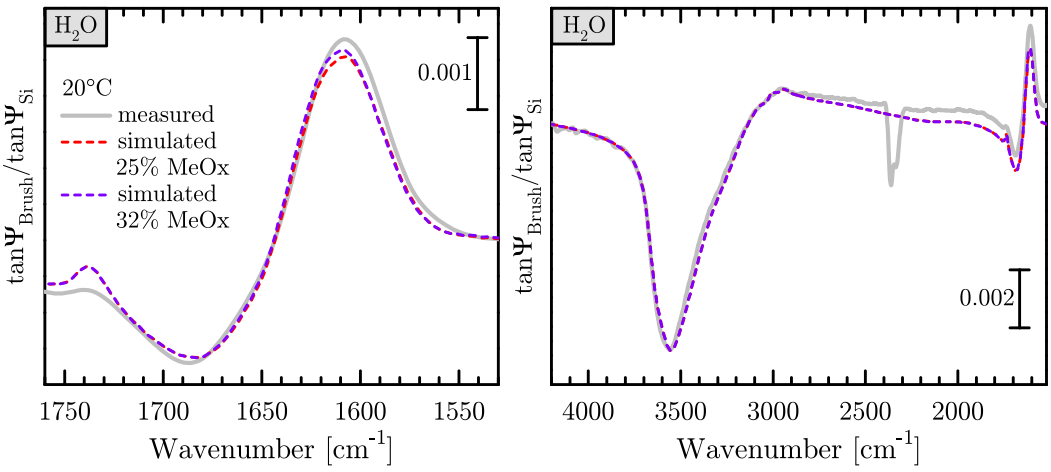

FIGURE 5.11: Measured and two exemplary simulated in situ tanΨ spectra of copolymer25 in H_2O at 20°C. The simulations were calculated with 25% and 32% MeOx content.

with 25% and 32% MeOx content. The right panel displays the mid-IR range, with the prominent downward-pointing $\nu(H_2O)$ band visible around 3600 cm^{-1}. The left panel is a zoom into the fingerprint range, showing the $\delta(H_2O)$ band, pointing downwards (1680 cm^{-1}), and the ν(C=O) band, pointing upwards (1610 cm^{-1}). In the left panel it can be seen that the intensity of the simulated ν(C=O) band of copolymer25 is too low. Increasing the MeOx content by several percent increases the C=O intensity, but results in a shift of the band to higher wavenumbers that leads to a bad overlap of measurement and simulation. From the synthesis procedure and also from simulations of copolymer25 in dry state we know that the MeOx content of the sample lies in the range of 25–30%, so a further increase of the MeOx content in the simulation would not represent the sample. Additionally, the band position would shift too far to higher wavenumbers.

The unsuccessful simulation of the in situ IR spectra leads to the assumption that the PMeOx or the P*c*PrOx data, that was used to build the model, does not accurately represent the respective fraction in the copolymer. As it has been discussed previously, there are several reasons for why the samples cannot directly be compared with each other, such as brush thickness, molecular weight, and grafting density. The different molecular weight of the polymer chains is probably the most important, because it influences the resulting grafting density and thickness of 'grafting-to' brushes. In this work, the PMeOx brush has much shorter chains compared to the chain length of copolymer25, and the qualitative analysis has shown that the PMeOx brush is not fully hydrated in water. PMeOx, being the most hydrophilic POx sample, was expected to show the lowest C=O frequency value in water due to extensive hydrogen bonding. However, in the swollen in situ spectra at 20 °C the maximum of the ν(C=O) band of PMeOx was at 1618 cm^{-1}, while the spectra of the other samples showed C=O frequencies around 1610 cm^{-1} (see figure 5.5). It is assumed that the relatively short PMeOx chains (22.0 kg/mol) cannot stretch out far enough into the solution to become fully hydrated. Accordingly, the brush restricts the amount of water being able to penetrate into the layer. Therefore, the n,k-data obtained from this brush does not properly represent the hydration state of the MeOx fraction in the copolymer25 sample and consequently leads to an unsuccessful simulation.

The P*c*PrOx and copolymer POx brushes were prepared from polymer chains with a

much higher molecular weight (48.4–61.3 kg/mol), resulting in a lower grafting density. The effect can be seen in figure 5.7. Both copolymer25 and P*c*PrOx can be assumed to be fully hydrated, because the ν(C=O) frequency in swollen state is the same for both brushes. The additional water content in copolymer25 has two explanations: First, it retains more water due to its increased hydrophilicity, caused by the 25% MeOx content. Second, it has the longest polymer chains (61.3 kg/mol) and therefore the lowest grafting density, which leaves more space between the chains for water molecules. Since the PMeOx brush with its low molecular weight does not reach a fully hydrated state in cold water, it does not serve as suitable reference to simulate the copolymer spectrum from pure PMeOx and P*c*PrOx data. To be able to do so, the pure brushes, from which the reference data is obtained, need to have a similar grafting density—and therefore a similar chain length—as the copolymer. If this is successful, POx can be suitable for modeling mixed polymer brushes. For example, their ν(C=O) band is easier to understand than the one in PNIPAAm. With the $\mathrm{N{-}H}$ group missing in POx, the number of interactions of the C=O group is limited to interactions with the solvent, because no direct interactions between the polymer chains can take place. This has been shown via the successful simulation of the POx samples in dry state, including the copolymer samples (see section 5.1.1). It might even be possible to include the oscillators of the C=O components of the two different POx to evaluate the contribution of each component.

5.2 Block-copolymer brushes PNIPAAm-*b*-PGMA

The idea behind the preparation of brushes from PNIPAAm-*b*-PGMA copolymers was to combine the two grafting steps of PGMA and PNIPAAm into one step, reducing time and effort needed for production. Brushes were produced in the group of Igor Luzinov at Clemson university [63] from two different block-copolymers via dip-coating from solution, as described in chapter 4. The block lenghts were chosen to be similar for PNIPAAm (M_n~25 kg/mol) while the PGMA block was either much shorter or longer. This ensured the resulting brushes to have similar PNIPAAm chain lengths for comparison with each other. Properties of the polymer chains and the prepared brushes are given in tables 4.5 and 4.6.

Covalent attachment of the copolymers to the substrate takes place via the PGMA blocks. There also occurrs cross-linking between these blocks, while PNIPAAm remains mobile, only being tethered to PGMA at one end. Ideally, this results in a PGMA-dominated layer close to the substrate, a PNIPAAm brush layer at the top, and an interpenetration layer between these two. Regarding the fact that only the PGMA blocks can form covalent bonds to the silicon substrate, the part of the polymer layer directly in contact with the substrate has to contain mainly PGMA. The thickness fractions and composition of interpenetration layer and top layer of the brush are unknown and it is possible that there is a composition gradient throughout the brush layer, starting with mainly PGMA at the substrate and ending with mainly PNIPAAm at the surface. As AR-XPS measurements of the top 2–10 nm of the brushes have shown (see section 4.2.2), even the topmost few nanometers contain PGMA, with the PGMA content increasing at increasing depth. This leads to a reduced mobility of the PNIPAAm chains, because they are partly trapped within the cross-linked PGMA network. The studies in this work aimed at resolving the structural nature of the copolymer brushes as well as the PNIPAAm chain mobility—an indicator for the switching abilities—and to compare the responsive behavior to traditional PNIPAAm brushes.

5.2.1 Characterization of the dry brushes

Previous studies of the PNIPAAm-*b*-PGMA brushes in dry state were perfomed at Clemson University by Michael Seeber to determine brush composition and surface properties [63]. The results are summarized in section 4.2.2. In this section the characterization of the brushes in dry state will be described, which has been perfomed with VIS and IR ellipsometry as well as with AFM.

Thickness and composition

VIS ellipsometry has been applied to determine brush thickness on the Si *wedges*, their 'dry state' referring to the brushes at ambient conditions of ~25 °C and ~30% relative humidity. On Si *wafers* the brush thickness was determined from AFM scans at the step edge of a scratch that was made in the brush layer. These scans were performed in an Ar purged atmosphere at 65 °C to remove any residual water within the brush layer. The purging did not result in a fully dried environment due to the large chamber volume. However, humidity was decreased to about 20% in the bulk volume of the chamber and even lower in the immediate surrounding of the sample, because the Ar gas flow was directed directly over the sample surface. Thickness results are listed in table 4.6 in section 4.2.2 and show that the values determined with VIS ellipsometry are several

TABLE 5.3: Band Assignments of dry block-copolymer brushes.

Frequency [cm^{-1}]		Assignment	Reference
PNI-70	PNI-40		
3440	3440	νN−H$_f$	[123]
3400-3250	3380-3250	νN−H$_b$	[123, 124]
3066	3066	Amide B (Fermi resonance)	[138]
(3005)	3005	ν CH_2 (epoxy group)	[139]
2973	2974	ν_{as} CH_3	[125, 140]
2935	2936	ν_{as} CH_2	[125, 140]
2875	2878	ν_s CH_x	[125, 140]
1735	1737	ν C=O (PGMA)	[123, 125]
1695-1630	1692-1620	amide I (PNIPAAm)	[123, 125, 140]
1570-1495	1570-1505	amide II (PNIPAAm)	[123, 125, 140]
1480-1440	1490-1440	δ CH_x	[123, 140]
1388	1389	δ $CH(CH_3)_2$	[123, 140]
1368	1368	δ $CH(CH_3)_2$	[123, 140]
1316		δ **CH**$(CH_3)_2$? amide III?	[125]

nanometers higher than those determined with AFM. This is due to the higher humidity of the environment during VIS ellipsometry measurements, in which the PNIPAAm chains start to swell.

To check composition and purity of the brushes and determine the dry state vibrational modes, IR-SE tanΨ spectra were recorded ex situ in dry state (see figure 3.1) with the ellipsometer chamber purged with dry air. The recorded tanΨ spectra of PNI-70 and PNI-40 are shown in figure 5.12. They are dominated by the strong signals of PGMA's C=O stretching vibration at 1735 cm^{-1} and PNIPAAm's amide I and II bands at $\sim$1650 cm^{-1} and $\sim$1550 cm^{-1}, respectively. The amide I band is mostly composed of C=O stretching with small contributions of C−N stretching, C−C−N deformation and in-plane N−H bending. The amide II band is composed of the in-plane N−H bending and C−N stretching modes with minor contribution from the in-plane C=O bending as well as C−C and C−N stretching [138]. One can clearly see the difference between the PGMA:PNIPAAm ratios of the two copolymer brushes.

In the inset of figure 5.12 the region of stretching vibrations is displayed. It shows the typical CH_x stretching vibrations in the range 3000–2850 cm^{-1}. The most prominent band lies around 2974 cm^{-1} and is more intense for PNI-70 than for PNI-40. It can be assigned to the asymmetric C−H stretching in the CH_3 moieties of PNIPAAm's isopropyl groups. The N−H stretching band occurs at higher frequency and is usually present as a Fermi resonance doublet in combination with the first overtone of amide II [138]. Its most intense contribution is the broad band at $\sim$ 3300 cm^{-1}. The corresponding N−H groups are mostly hydrogen-bonded (ν(N−H$_b$)) to C=O of neighboring polymer sections. Only a small fraction is in the free state (ν(N−H$_f$)), visible as a weak band around 3440 cm^{-1}. The second part of the Fermi resonance doublet can be seen as a weak band present around 3066 cm^{-1}. Band assignments for the two copolymer brush compositions are listed in table 5.3.

In previous studies of our group on thin homopolymer layers of PNIPAAm and PGMA, which were carried out by Andreas Furchner [47], the brushes in dry state were simulated by an optical layer model and fitted to the spectra. From those simulations

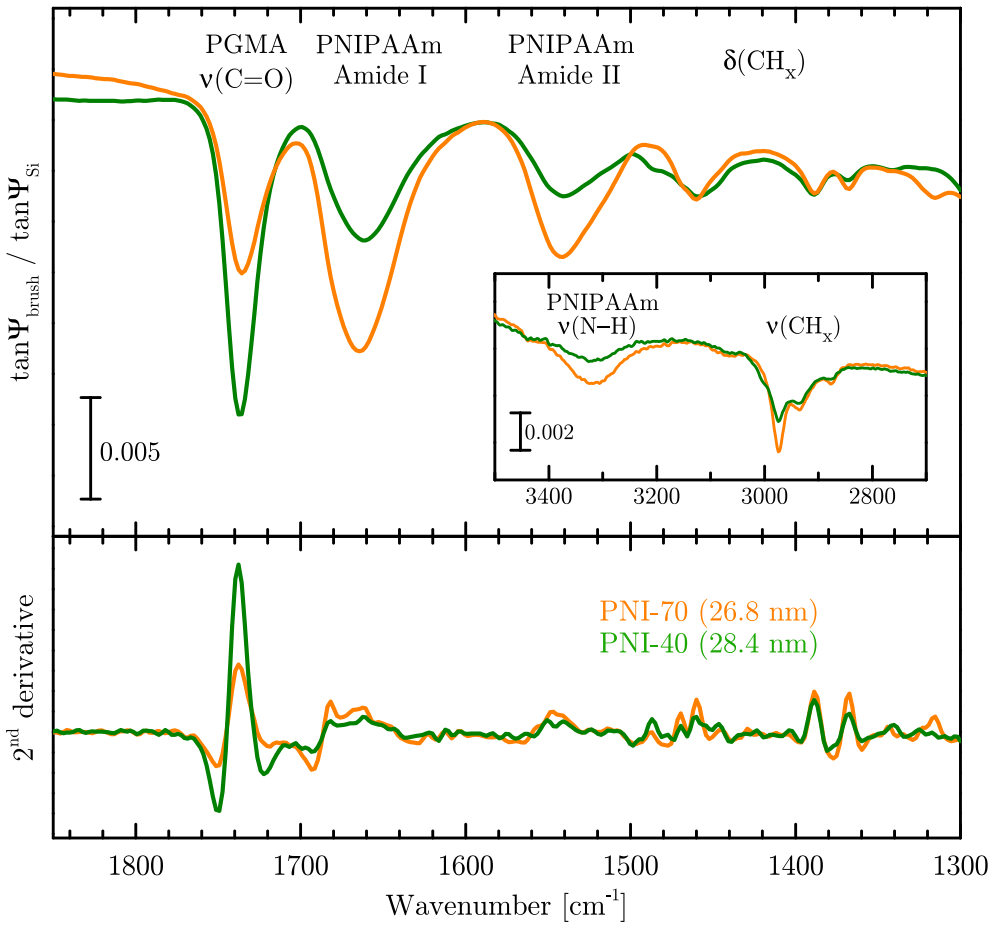

FIGURE 5.12: tanΨ spectra (top) and their second derivatives (bottom) of PNIPAAm-*b*-PGMA block-copolymer brushes in dry state. Measurements were done ex situ at an angle of incidence of 65° and are referenced to a clean silicon substrate.

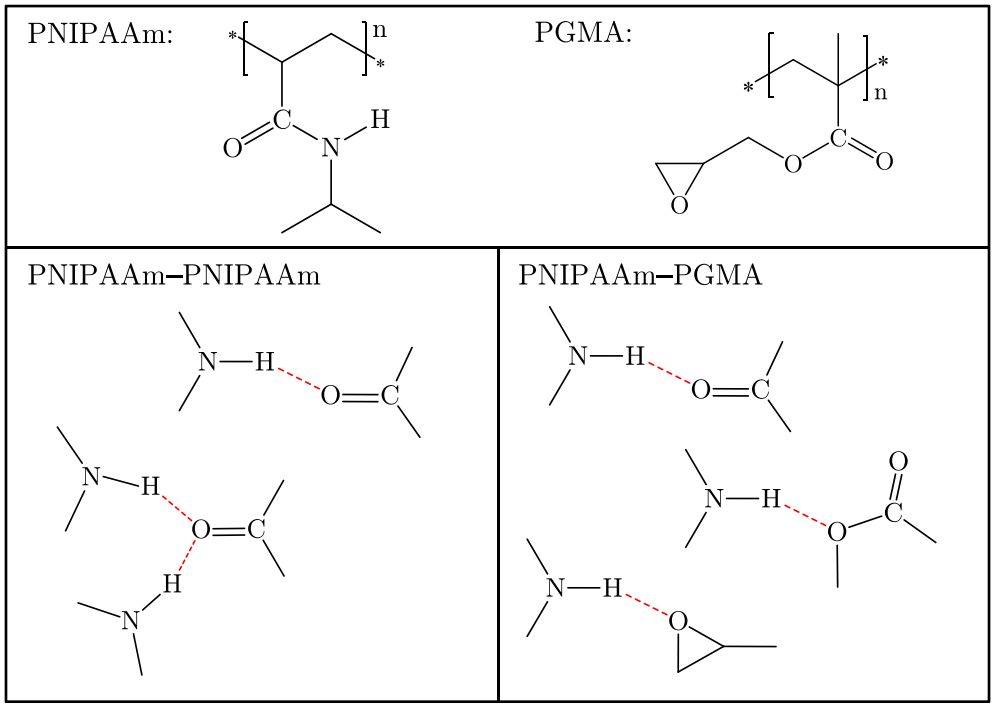

FIGURE 5.13: Possible interactions between the funtional groups of PNIPAAm and PGMA in dry state. The lower left panel displays PNIPAAm–PNIPAAm interactions, the lower right one PNIPAAm–PGMA interactions. Note that each oxygen atom in PGMA can—in principle—form two hydrogen bonds, which increases the number of possibilities to six. However, this is unlikely due to steric hindrance.

the calculated n, k-data was used to build a model for PNIPAAm-*b*-PGMA copolymer layers. Different layer models were tested: (1) A one-layer model using an effective medium approximation either with a homogeneous mixture or a lateral gradient of the two polymers; (2) A two-layer model (PGMA and PNIPAAm); (3) A three-layer model, which is based on the two-layer model with an additional mixed interpenetration layer in between. With the total brush thickness in dry state fixed to the value determined via VIS ellipsometry (± 1 nm), free parameters in the fitting step were thickness of the individual layers as well as the volume fraction in the mixed layers.

In all cases, the simulation resulted in good reproduction of PNIPAAm's amide I band while both the amide II (PNIPAAm) and C=O (PGMA) bands resulted in higher amplitudes than measured. These differences indicate the presence of additional interactions between PNIPAAm and PGMA, so that the PNIPAAm-*b*-PGMA layers cannot be modeled as a simple mixture of the respective homopolymers. For example, hydrogen bonds can form between PNIPAAm's N−H group and PGMA's C=O group, affecting the frequencies of amide II (PNIPAAm) and ν(C=O) (PGMA). These interactions will be similar to the intramolecular N−H $\cdots$ O=C hydrogen bonds in PNIPAAm homopolymer brushes. There are several possible interactions between PNIPAAm and PGMA (see figure 5.13), resulting in many unknown variables in the model. Since the PNIPAAm-*b*-PGMA system is already quite complicated in dry state, the further analysis (especially in situ) of PNIPAAm-*b*-PGMA brushes in this work is kept to qualitative conclusions.

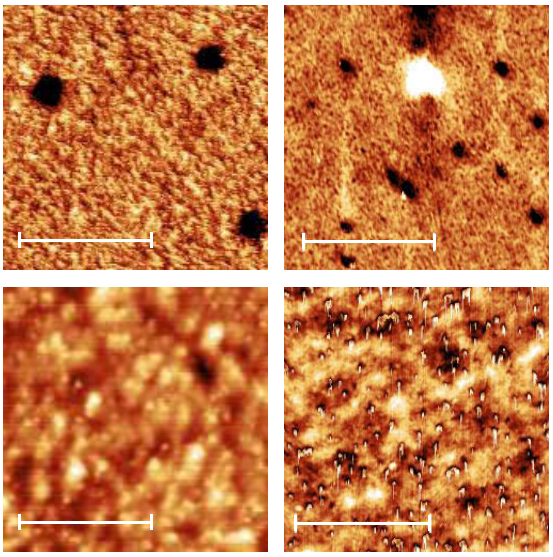

FIGURE 5.14: AFM images of PNIPAAm-*b*-PGMA block-copolymer brushes. *Top:* PNI-70 with d_{dry} = 32.4 nm; *Bottom:* PNI-40 with d_{dry} = 28.0 nm; *Left:* Before the swelling experiment in water; *Right:* After the swelling experiment in water; Scale bars: 500 nm

Brush surface characterization

AFM scans are used to study the surface topography and, by using the scratch method, one can also determine total layer thickness at the step edge of a scratch in the layer. Figure 5.14 shows the brush surface scans of PNI-70 and PNI-40 in dry state under ambient conditions before and after a swelling experiment in water. The scans on the left were recorded after the last MEK rinsing step of the preparation procedure, MEK being a good solvent for both PNIPAAm and PGMA. The scans on the right show repeated measurements in dry state after the swelling experiment in water had been performed, water being a good solvent for PNIPAAm but a bad solvent for PGMA.

Both samples show an overall smooth surface. However, dark spots with a diameter of ~100 nm and a depth of ~20 nm are visible on the surface of the sample with higher PNIPAAm content (PNI-70). These cavities decreased in size and depth after the swelling experiment in water (see figure 5.15) due to rearrangement of the mobile PNIPAAm chains in close proximity.

It is likely that the cavities originate from polymer bundles that neither formed a covalent bond with the substrate nor with a surrounding PGMA segment, therefore they were washed out in the rinsing step. Michael Seeber estimated the radius of gyration (R_g) of the PNIPAAm-*b*-PGMA polymer chains to be 4.1–4.5 nm, resulting in a diameter of $2R_g$~8.5 nm. This means one of such bundles is an aggregate of many polymer chains [63].

The AFM scans in figure 5.14 were also evaluated in terms of surface roughness of the brushes to check the influence of different solvent treatments (see table 5.4). PNI-70 has a decreased root mean square (rms) of surface roughness after rinsing in water compared to the initial MEK rinsed surface. This occurs not only because the cavities decrease in size and depth but also because the brush surface between the cavities becomes smoother. It was expected that such a smoother surface after a water rinse will be observed for all brushes, because only the water-soluble PNIPAAm blocks can swell in water and rearrange at the brush–water interface. However, this seems not to

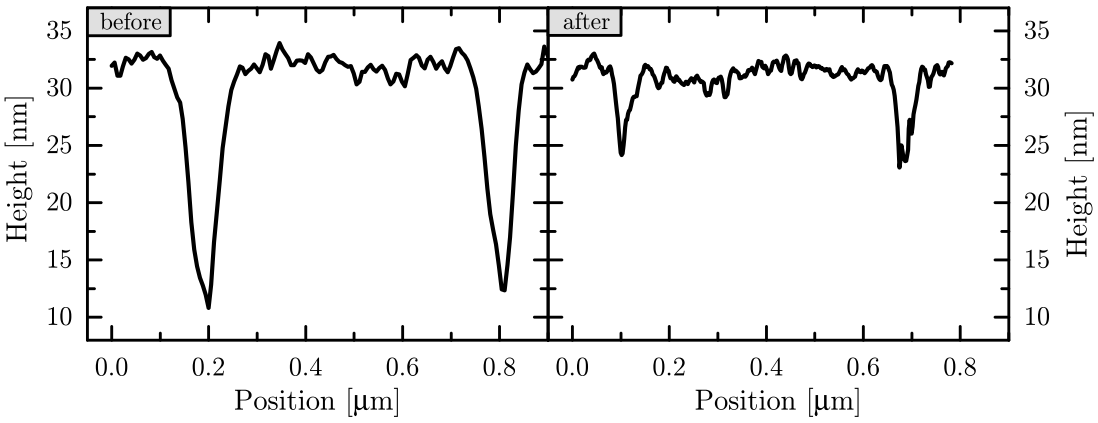

FIGURE 5.15: AFM height profile of PNI-70 with $d_{dry} = 32.4$ nm before (left) and after (right) the swelling experiment in water.

apply for PNI-40, possibly due to its PNIPAAm blocks being too short and therefore their mobility is insufficient to smoothly cover the underlying PGMA. In fact, its surface roughness is slightly increased after the water rinse.

TABLE 5.4: Root mean square (rms) roughness of the copolymer layers under different conditions. Due to the cavities in PNI-70 rms roughness values were determined both including and excluding those areas.

Sample	d_{dry} [nm]	brush state	rms roughness [nm]	
			incl. cavities	excl. cavities
PNI-70	32.4	dry, MEK rinse	1.6 ± 0.1	0.9 ± 0.1
		dry, H_2O rinse	0.9 ± 0.1	0.7 ± 0.1
	26.8	dry, H_2O rinse	0.7 ± 0.1	–
		dry, PBS rinse	0.8 ± 0.1	–
	24.2	dry, in situ AFM	0.9 ± 0.1	–
		H_2O, 24°C	1.0 ± 0.1	–
		H_2O, 40°C	1.0 ± 0.1	–
PNI-40	28.0	dry, MEK rinse	0.7 ± 0.1	–
		dry, H_2O rinse	0.9 ± 0.1	–
	25.1	dry, H_2O rinse	0.9 ± 0.1	–
		dry, PBS rinse	1.0 ± 0.1	–
	23.0	dry, in situ AFM	0.9 ± 0.1	–
		H_2O, 25°C	1.0 ± 0.1	–
		H_2O, 40°C	1.3 ± 0.2	–

5.2.2 In situ swelling behavior

In section 4.2.2 some preliminary characterization of the PNIPAAm-*b*-PGMA brushes has been described, including contact angle measurements at different temperatures to determine the switchability at the surface. The experiments show that the brushes exhibit a temperature-dependent change of surface wettability. Especially PNI-70, after being rinsed with water, has an increased change in contact angle compared to a traditional PNIPAAm brush [63]. However, it should be noted that the contact angle

probes the brush–ambient interface but cannot give information about the swelling degree or the switching behavior within the layer.

This section describes the results of in situ experiments on PNIPAAm-*b*-PGMA copolymer brushes, which are a measure for the PNIPAAm chain mobility. In situ IR-SE experiments as well as complementary methods were performed on the brushes and compared to the results obtained on traditional PNIPAAm brushes in previous studies [16, 28, 47]. Most of the results presented in this section have already been published [141].

In situ AFM

A first evaluation of the swelling degree of the brushes and their extent of temperature-responsive collapse in water was done with in situ AFM. These experiments were done with Oleksandr Trotsenko in the group of Sergiy Minko at the University of Georgia in Athens, USA. Figure 5.16 shows the height profiles in dry state as well as in water at low and high temperature.

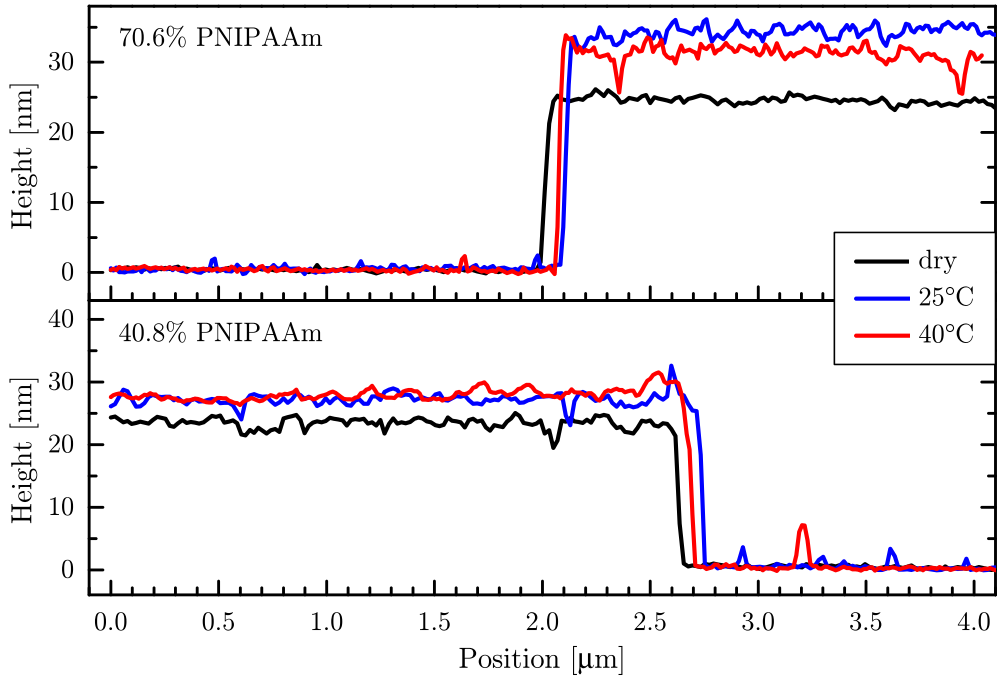

FIGURE 5.16: AFM in situ profiles of PNIPAAm-*b*-PGMA block-copolymer brushes at a step edge. *Top:* 70.6% PNIPAAm; *Bottom:* 40.8% PNIPAAm.

The swelling degree of the brushes turned out to be much less than expected. Both samples are about 24 nm in dry state and swell only a few nanometers in water. At room temperature PNI-70 reaches 34 nm and collapses to about 31 nm at 40 °C, while PNI-40 only swells to about 27 nm and does not show any temperature-sensitive collapse. A traditional PNIPAAm brush on the other hand swells to several times its dry thickness and collapses significantly [16, 47]. Table 5.5 summarizes the in situ swelling results of the copolymer brushes and a traditional PNIPAAm brush, determined with AFM as well as visible and infrared ellipsometry.

TABLE 5.5: In situ thickness results of the copolymer brushes and of a traditional PNIPAAm brush [16].

Sample	Method	d_{dry} [nm]	$d_{swollen}$ [nm]	$d_{collapsed}$ [nm]
PNI-70	AFM	24.5	34.5 (25°C)	31.2 (40°C)
	VIS	25.2	26.3 (18°C)	26.3 (40°C)
PNI-40	AFM	23.4	27.2 (25°C)	27.9 (40°C)
	VIS	23.8	25.6 (18°C)	27.9 (40°C)
PNIPAAm	IR	12.6	43 (25°C)	20 (39°C)
	VIS	11.0	45.6 (25°C)	19.5 (39°C)

The in situ AFM images were also used to determine surface roughness of the brushes (see table 5.4). Both samples show a similar roughness in dry state and in water at both temperatures with one exception: PNI-40 has an increased roughness at 40 °C compared to room temperature. This might be correlated to its increased roughness in dry state after a water rinse, as mentioned previously. A reason could be a rearrangement of the rather short PNIPAAm blocks, which is insufficient to smoothly cover the underlying rough PGMA network. Instead, the PNIPAAm blocks tend to accumulate.

In situ VIS Ellipsometry

In situ ellipsometry in the visible spectral range was performed with comparable brush samples on Si(111) wafers at IPF in Dresden by Eva Bittrich. Figure 5.17 shows exemplarily the two heating cycles of a swelling experiment on a $d_{dry} = 27.7$ nm PNI-70 sample in water. Similar to the results of in situ AFM scans, the figure shows a low swelling degree and only a marginal temperature-dependent collapse of the brush. Below 20 °C PNI-70 swells to about 36–37 nm, with a collapse of ~2 nm taking place just above 20 °C. In the range of 25–40 °C the brush thickness stays constant and then it slightly increases again. The latter behavior of the brush swelling at higher temperatures was also observed for PNI-40 (data not shown). It swells from a dry thickness of (23.8 ± 0.1) nm to (25.6 ± 0.1) nm at 18 °C and further to (27.9 ± 0.1) nm at 40 °C without any collapse in between.

The small reswelling behavior observed for PNI-70 around 40 °C, and accordingly a decrease in refractive index of the swollen brush layer, as well as the continuous thickness increase for PNI-40 indicate that more water molecules enter the brushes. The reason for this behavior remains unclear at this point. It could be related to smaller water clusters that are present at elevated temperatures, due to their increased kinetic energy, and that are able to penetrate the brush cavities.

There is also a difference to be noted between in situ AFM and VIS ellipsometry results: The PNI-70 sample scanned with in situ AFM was still 'swollen' at 25 °C. Its collapse took place somewhere between 25 °C and 40 °C instead of ~20 °C as it was measured with VIS ellipsometry.

In contrast to the observed LCST ranges for the block-copolymer brushes, pure PNIPAAm in solution or in form of a traditional grafting-to brush exhibits an LCST behavior around 31–32 °C [24, 25, 28, 47]. It seems that the combination of PNIPAAm in a block copolymer with hydrophobic PGMA lowers the LCST due to the increased hydrophobicity of the layer. Additionally, an increased hydrophobicity results in lesser affinity to take up water, reducing the swelling of the brush.

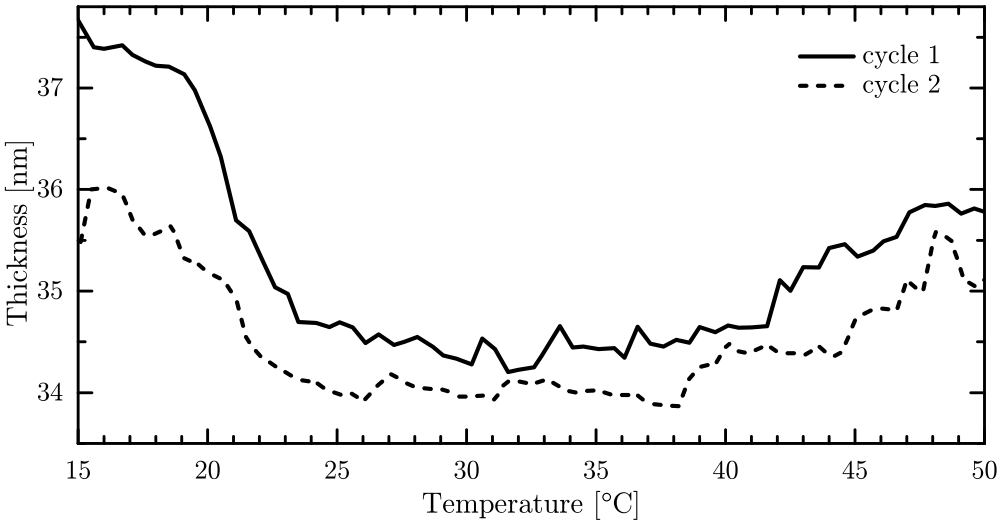

FIGURE 5.17: In situ VIS ellipsometry swelling results of a $d_{dry} = 27.7$ nm PNI-70 brush in water. Temperature was cycled two times from 15 °C to 54 °C at 0.7 °C/min. Displayed are the two heating cycles.

As described in chapter 4, with AR-XPS measurements the composition of the outer 2–10 nm of the copolymer layers was studied by Michael Seeber in Clemson [63]. He found that even the very top layer of about 2 nm consists of only 71–83% PNIPAAm, and that the amount of PGMA increases with increasing probing depth. A statement found in literature [22] describes, that polymer dynamics are slowed down considerably when different polymers are entangled and when they can form intermolecular interactions. Taking this statement into consideration, there is a disadvantage for the PNIPAAm chain mobility in the copolymer brushes compared to traditional PNIPAAm brushes.

In situ IR Ellipsometry

From the previously described results we know that the PNIPAAm-*b*-PGMA copolymer brushes have a low swelling degree in water, and a response to temperature in terms of thickness could only be observed for PNI-70. Still, it is possible that temperature-dependent changes of polymer–water interactions occur in the PNI-40 brush without water being released from the layer. The changes would take place on the molecular level and result in different vibrations of certain functional groups. Vibrational spectroscopy such as IR-SE is used to characterize the vibrations via their band position in IR spectra.

The results of in situ IR-SE experiments on PNI-70 and PNI-40 are displayed in figures 5.18 and 5.19, respectively. The graphs show tanΨ spectra of each brush in water at 25 °C and 45 °C, referenced to the measurement of a blank silicon wedge under the same conditions. Additionally, the spectra were smoothed with a cubic smoothing spline in MatLab (smoothing coefficient $\lambda = 0.998$). Second derivatives of the spectra are displayed underneath the tanΨ spectra, showing the different components of the bands more clearly. In this part of the fingerprint range the most important signals are the C=O vibrational band of PGMA at 1735 cm^{-1} and PNIPAAm's amide I and II bands at $\sim$ 1640 cm^{-1} and $\sim$ 1560 cm^{-1}.

In both samples the ν(C=O) band of PGMA stays constant with temperature. This was expected since PGMA is a hydrophobic polymer that does not interact with water [142].

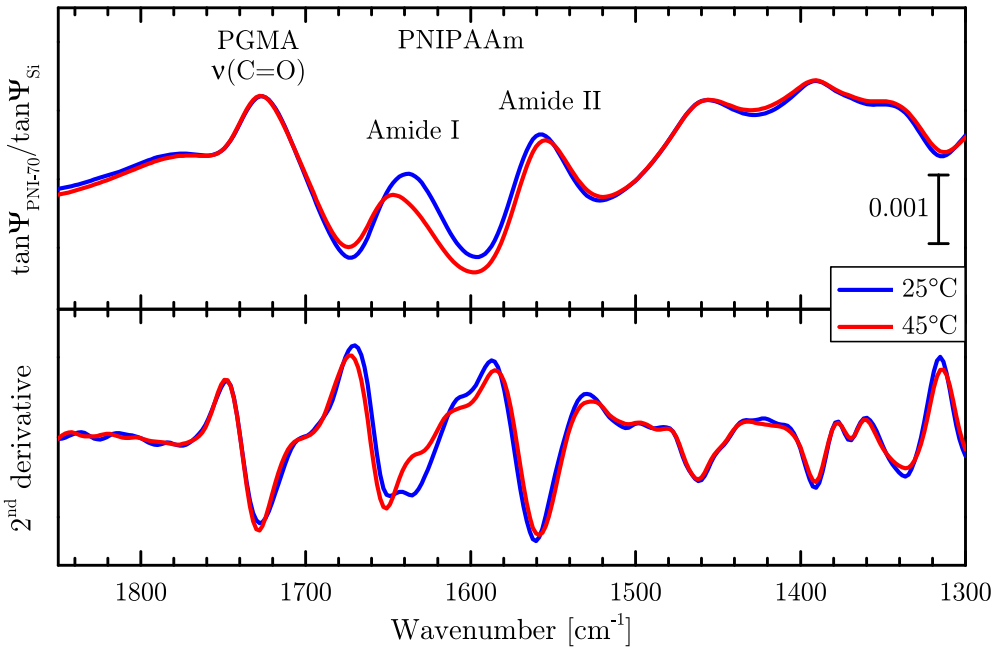

FIGURE 5.18: In situ tanΨ spectra of PNIPAAm-*b*-PGMA block-copolymer brush PNI-70 (70.6% PNIPAAm) in water and their second derivatives. Spectra are referenced to a clean silicon wedge under the same conditions.

PNIPAAm's amide bands on the other hand show more or less significant changes, associated with the switching behavior of the brushes around their volume phase transition (LCST behavior). Similar to PNIPAAm in solution [140] the amide I band of the brushes, which is mainly composed of the ν(C=O) stretching mode, contains at least two major components in water [28]. One is related to C=O groups fully hydrated by water molecules ($\sim 1625\,\mathrm{cm}^{-1}$), and the other is due in part to C=O ... H−N hydrogen-bond interactions ($\sim 1652\,\mathrm{cm}^{-1}$).

In the spectrum of PNI-70 at 25 °C the amide I band shape contains contributions of both hydrated and amide–amide interacted C=O groups (see figure 5.18). In the dehydrated state above the LCST, the hydrated component of PNI-70 is decreased (see the second derivative around 1630–1625 cm^{-1} in figure 5.18) which results in a shifted maximum of amide I in the tanΨ spectrum. However, this is not the case for PNI-40. Its spectra in figure 5.19 show a mixture of the two components in the amide I band at both temperatures and hardly any intensity changes in the second derivative. A comparison of the copolymer brush spectra to those of a traditional PNIPAAm brush at 25 °C and 45 °C [141] in the fingerprint region is displayed in figure 5.20. Here, the amide I signal of the traditional PNIPAAm brush changes clearly from a strongly hydrated state at 25 °C to increased amide–amide interaction at 45 °C.

Identification of the single components in the amide II band is more difficult, since it includes a coupling of the N−H bending (60%) and C−N stretching (40%) modes [25, 29, 140]. During the phase transition the frequency of the N−H vibration shifts to lower wavenumbers due to a decreased force constant of the vibration [28]. This is due to a change of hydrogen bonding from N−H ··· OH_2 to N−H ··· O=C that can be clearly observed in the traditional PNIPAAm brush. In the copolymer brushes only a small redshift upon heating is detected, indicating less changes of N−H interactions.

The decrease of amide band changes with decreasing PNIPAAm content in the

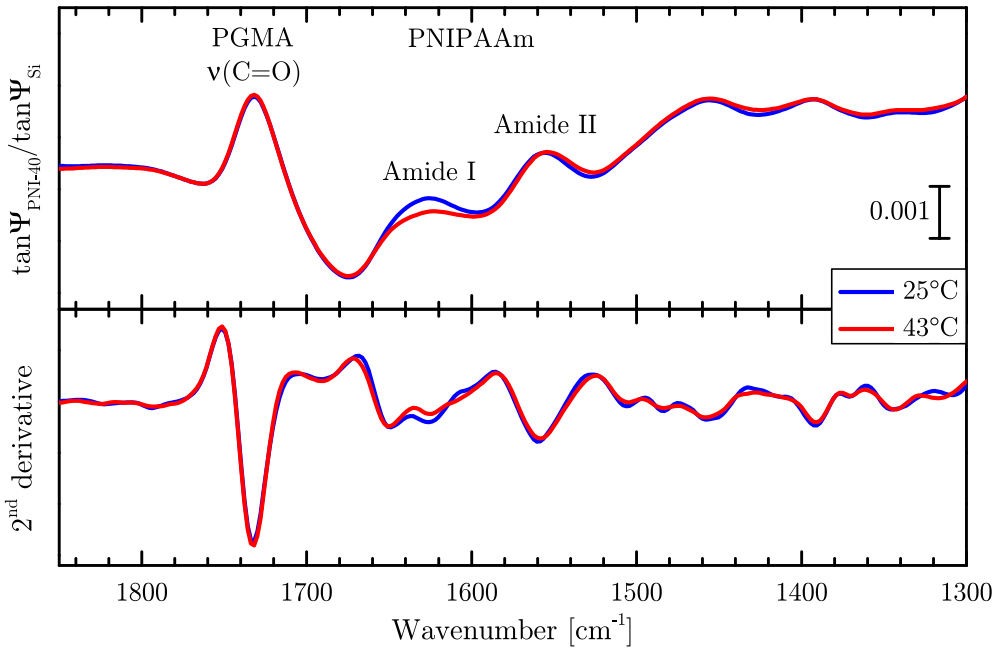

FIGURE 5.19: In situ tanΨ spectra of PNIPAAm-*b*-PGMA block-copolymer brush PNI-40 (40.8% PNIPAAm) in water and their second derivatives. Spectra are referenced to a clean silicon wedge under the same conditions.

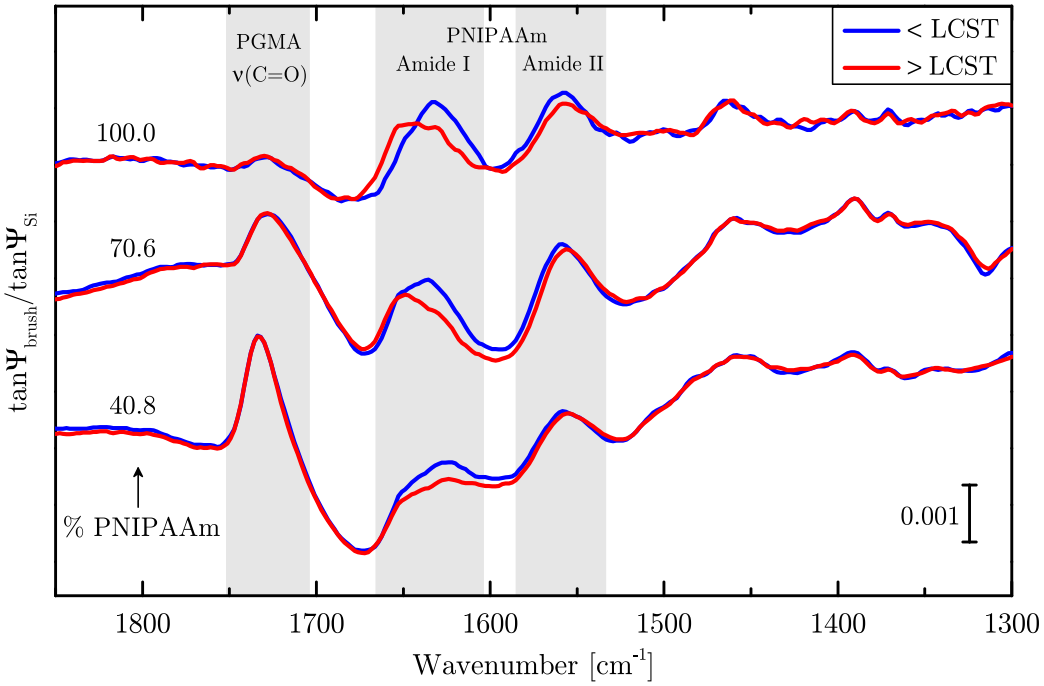

FIGURE 5.20: In situ tanΨ spectra of the two PNIPAAm-*b*-PGMA block-copolymer brushes at 25 °C and 43 °C, and a traditional PNIPAAm brush at 25 °C and 40 °C. Spectra are referenced to $\tan\Psi_{Si}$ of a clean silicon wedge under the same conditions. Note that the different interfaces (silicon/solution vs. brush/solution) cause an overlap of amide I by a downward-pointing $\delta(H_2O)$ band.

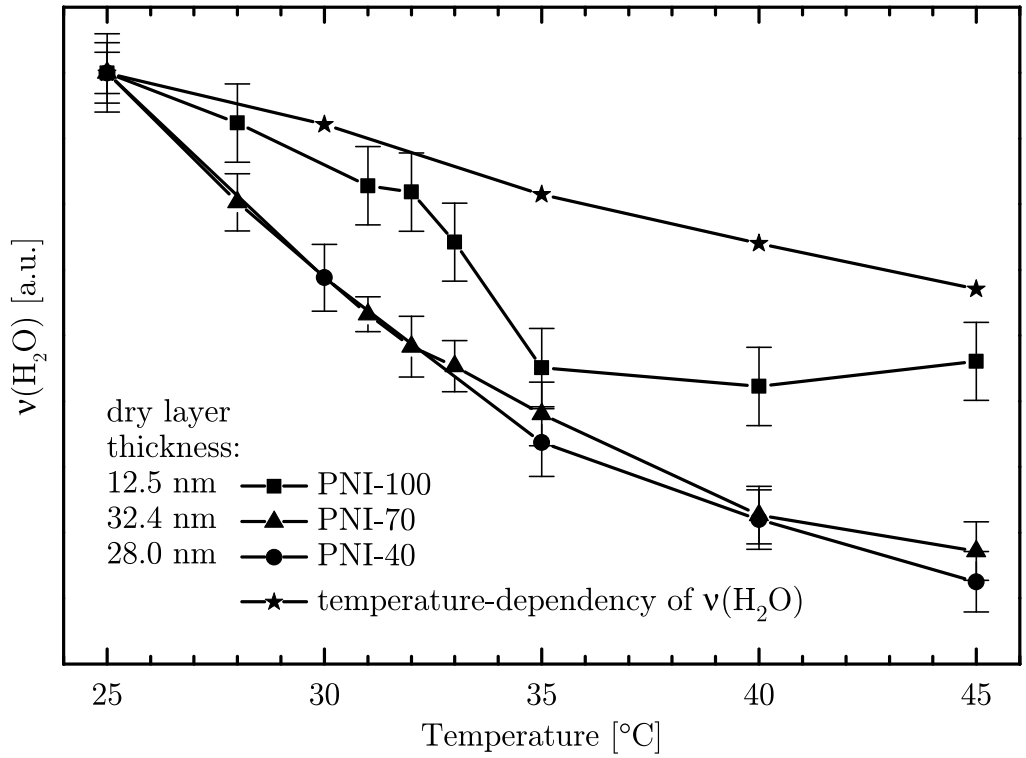

FIGURE 5.21: Change of the $\nu(H_2O)$ amplitudes of a traditional PNIPAAm brush (PNI-100) and the two copolymer brushes PNI-70 and PNI-40 in dependence of temperature in comparison to an optical simulation of a swollen brush without temperature-responsive behavior. A simulation is included to show the temperature-dependent changes of $\nu(H_2O)$ in a constantly swollen polymer (d = 30 nm, 50% H_2O). Amplitude values are relative values normalized to the state at 25°C.

brush suggests that the PNIPAAm block in the copolymer brushes undergoes a smaller decrease in water content and an overall weaker temperature-dependent transition. This behavior is attributed to the increased amount of PGMA present in the layer, its hydrophobicity suppressing the diffusion of water into the brush. In the copolymer brushes the grafted ends of the PNIPAAm blocks—that is, the connections between PNIPAAm and PGMA—can be deep within the cross-linked PGMA network. This is due to the one-step coating process of the block copolymers instead of the traditional two-step procedure (see section 4.2.2) and results in the PGMA network in the copolymer brushes being thicker than the average 2 nm PGMA anchoring layer in traditional grafting-to brushes. It causes the PNIPAAm chains to be partly trapped, restricting their mobility which in turn decreases the temperature-dependent switching behavior. In PNI-40 the PNIPAAm fraction seems to be too low to enable siginificant swelling. The mobility is limited to such an extent that it prevents water molecules from entering the brush. Consequently, if the brush does not properly swell in water, there can hardly be any potential for changes in interactions between polymer and water that are necessary for a collapse of the brush.

There is another important difference between traditional PNIPAAm brushes and the copolymer brushes: The little extent of switching in the copolymer brushes is spread over a wide temperature range. This can be followed by looking at the degree of changes that occur in the water stretching band around 3600 cm^{-1}. In figure 5.21 the amplitude value of νH_2O is displayed for PNI-70, PNI-40, and a traditional PNIPAAm brush (PNI-100). The amplitudes of each sample are normalized to the value at 25 °C to compensate for differences in brush thickness. Additionally, the same data was calculated for a simulated polymer layer that does not exhibit any functional behavior. The simulation describes a constantly swollen polymer layer of d = 30 nm and 50% water content without any temperature-responsive changes. This visualizes the change in νH_2O amplitude that occurs in all brushes due to the temperature-dependency of water in the swollen layer.

The simulated plot (stars) in figure 5.21 shows a linear decrease of the amplitude in dependence of temperature. A similar course is observed for the amplitudes of PNI-70 (circles) and PNI-40 (triangles), but for these layers the slope is steeper and slightly curved. At low temperatures the curves have a higher slope that levels off around 35 °C to a similar slope as the simulation. This indicates that at temperatures < 35°C there is a change of the water stretching vibrational mode additional to the temperature-dependent one that is described by the simulation. It is caused by changes in swelling of the brush in the range of 25–35 °C. It is likely that the transition already starts at lower temperatures, as it was determined with VIS ellipsometry (see figure 5.17).

The last plot in figure 5.21 (squares) describes the change in the $\nu(H_2O)$ band of the traditional PNIPAAm brush (PNI-100). Contrary to the copolymer brushes, this curve clearly shows a transition from swollen to collapsed brush in a small temperature range (32–35 °C).

Summarizing the results on the functional behavior of PNIPAAm-*b*-PGMA brushes, it was found that the brushes hardly swell in water. Their thickness increases only very little and the brushes show no collapse when the temperature is raised. IR-SE spectra however indicated that on the molecular level some changes of the interactions between polymer and water take place upon an increase in temperature. Compared to traditionally prepared PNIPAAm grafting-to brushes the changes were less prominent, but of the same nature. Amide–water as well as amide–amide hydrogen bonds can be identified in the "swollen" state. Above PNIPAAm's LCST, the amount of amide–water interactions decreases, indicating less hydration of the polymer chains. The amount of amide–amide interactions on the other hand did not increase simultaneously, as they do in traditional PNIPAAm brushes. This can be explained by steric hindrance in the copolymer brush, which is caused by the cross-linked network of PGMA blocks throughout the layer. This steric hindrance is likely to be the reason why the changes in the in situ IR-SE spectra take place over a wide temperature range for the PNIPAAm-*b*-PGMA samples, in contrast to the abrupt switching of traditional PNIPAAm brushes around 32 °C. The formation of amide–amide hydrogen bonds between neighboring PNIPAAm chains facilitates the collapse, because the chains are drawn closer to each other and water molecules are released from the layer.

At this point it is questionable, if the PNIPAAm-*b*-PGMA samples can be called *brushes*. According to the calculated grafting densities (0.3–0.5 chains/nm^2) and the radius of gyration of the copolymers' PNIPAAm fractions (4.1–4.5 nm) [63] the samples are in the brush regime. However, due to the structure of the layer, the PNIPAAm chain mobility—an important characteristic of polymer brushes—is strongly limited.

5.3 Protein adsorption

Proteins are an important class of biomacromolecules, being involved in a large number of biological processes. They are composed of a long chain of amino acids connected via amide bonds, the so-called peptide bonds. The sequence along the peptide chain is called primary structure. These chains are folded to form a secondary structure, e.g. α -helices or β -sheets, and the folded sections can further interact with each other, which is called tertiary structure. When several of such clusters interact with each other to form the full protein, it is called quarternary structure. Apart from the primary structure, the other structures are formed mostly by non-covalent interactions, especially hydrogen bonding and hydrophobic interactions. The resulting three-dimensional structure is highly specific [143]. It is also the reason why proteins are very sensitive to environmental changes, such as pH or temperature [144]. This leads to unfolding and denaturation of the protein and consequently to a loss of protein function. Similar processes can happen upon adsorption of the protein [145].

In some cases protein stability can be enhanced via immobilization in a membrane or on a surface. For example, immobilization of trypsin can enhance its stability at elevated temperatures or basic pH (6–10) and increase its storage stability in buffer solution [146]. In such cases, the type of immobilization—covalent linking, physical adsorption, etc.—is of importance to maintain protein activity [144, 147]. Possible applications for such immobilized proteins are catalytic reactions, biosensors, or tissue engineering [50].

The latter was being focused on in the joint DFG–NSF project in which this work was involved. As described in chapter 2, the goal of the project was to create functional polymer interfaces that can control cell attachment and detachment and maybe even cell proliferation via immobilization of growth factors within the polymer. Adsorption of cells to a surface takes place via membrane proteins or extracellular proteins [5]. Therefore the first step to evaluate the brushes' behavior towards biomolecules is to study the adsorption and desorption of simple proteins on the surfaces.

PNIPAAm has been of high interest because it is biocompatible and shows a temperature-dependent transition close to the physiological temperature. For traditional PNIPAAm brushes both protein adsorbing [6, 8, 90] and repelling [7, 43–46] results are described in literature, depending on the molecular weight and grafting density of the chains. Considering brushes with thickness and grafting density similar to the brushes studied in our group (grafting density 0.1–0.3 chains/nm^2, thickness up to 30 nm) PNIPAAm is protein-resistant in most cases. This is advantageous for biomedical applications which demand that the surfaces do not adsorb proteins or other biomolecules [148, 149]. Examples for PNIPAAm brushes with protein adsorption abilities are those with low grafting densities [8] or PNIPAAm-*co*-PGMA surfaces [9].

Protein adsorption is mainly dependent on hydrophilic and hydrophobic interactions. Usually, the uncharged, hydrophobic domains are hidden in the inner core of a protein and most of the charged ones are present at or close to the surface [144]. The resulting net charge is individual for each protein and pH-dependent, with the pH value at which a protein has a net charge of zero being called the isoelectric point (IEP). Since driving forces of protein adsorption are usually of hydrophobic origin, the IEP is an important value around which the respective protein adsorbs strongest [145, 150]. Unfolding can enhance hydrophobic protein–surface interactions, leading to strong adsorption, but it is often irreversible because extensive unfolding leads to denaturation of the protein. Thermodynamic reasons can also be a driving force for protein adsorption. This has been found in a study of protein adsorption on polyelectrolyte brushes, where

apart from electrostatic repulsion also entropic forces influence the protein affinity of the brush [151].

Protein adsorption to polymer brushes can take place in three different generic modes that are called primary, secondary, and ternary adsorption [3, 152]. Primary adsorption takes place when the protein diffuses between the polymer chains and adsorbs directly to the substrate surface. Secondary and ternary adsorption describe adsorption to the polymer chains, either on top of the brush surface (secondary adsorption) or within the brush (ternary adsorption). Which mode of adsorption takes place is dependent on several factors, for example protein size, grafting density of the brush, chain length, or polymer–protein interactions.

The blood plasma protein fibrinogen (FIB) was chosen for the adsorption experiments because it strongly (and in many cases irreversibly) adsorbs to hydrophobic surfaces [153], serving as a good indicator for the presence of PGMA segments on the top of the copolymer brushes. FIB is an elongated 340 kDa blood plasma protein with approximate dimensions of 5 x 5 x 45 nm [154]. Its IEP lies around pH 5.5 [155, 156].

Adsorption on PNIPAAm-*b*-PGMA brush samples was determined with in situ ellipsometry in the VIS and IR ranges. Additionally, FIB adsorption was performed on a plain silicon substrate and a thin PGMA layer. In all experiments measurements of adsorption processes monitiored under otherwise identical conditions were referenced to the spectrum of the initial sample spectrum before the adsorption, leading to $\tan\Psi_{\text{sample+protein}}/\tan\Psi_{\text{sample}}$.

5.3.1 Fibrinogen adsorption on Silicon and PGMA

Prior to the protein experiments on polymer brushes, the adsorption of FIB on a silicon substrate (hydrophilic surface) as well as on a ~ 2.5 nm thin PGMA layer (hydrophobic surface) was evaluated. Both of these substances are expected to adsorb FIB [48, 157]. Their affinity towards proteins is important for our studies on polymer brushes, because they might influence the adsorption results due to primary and ternary adsorption. Especially in the case of PGMA we were interested in the adsorption results, because PGMA is present in the copolymer brushes and might have an influence on the behavior of the brush–liquid interface towards proteins. Additionally, knowledge of the protein's amide bands is necessary, since PNIPAAm also contains amide groups, causing an overlap of the vibrational bands in the spectra.

Figure 5.22 displays in situ $\tan\Psi$ spectra of bare silicon (left) and the thin PGMA layer (right) immersed in FIB solution, referenced to the same samples in protein-free buffer solution. Referenced in situ $\tan\Psi$ spectra are a measure of the change in optical contrast of the brush–solution interface. Upon protein adsorption, upward-pointing vibrational amide I and II bands will become visible, which is clearly the case in these experiments. On both samples, FIB adsorption is evidenced by the presence of strong amide I and II bands around 1650 cm^{-1} and 1550 cm^{-1}, respectively.

On silicon the subsequent spectra at 25, 45 and again at 25 °C show an increase of adsorbed FIB over a time period of about 6 hours. The shape of the amide bands does not differ when adsorption takes place at 25 or 45 °C, the latter being just below the temperature of the first denaturation step of FIB [158, 159]. The additional spectrum of the adsorbed layer recorded in protein-free PBS after a buffer rinse at 25 °C (green spectrum in figure 5.22) also shows no decrease in the amide bands. This indicates that FIB is strongly adsorbed to the substrate and its structure in the adsorbed state does not change in the measured temperature range.

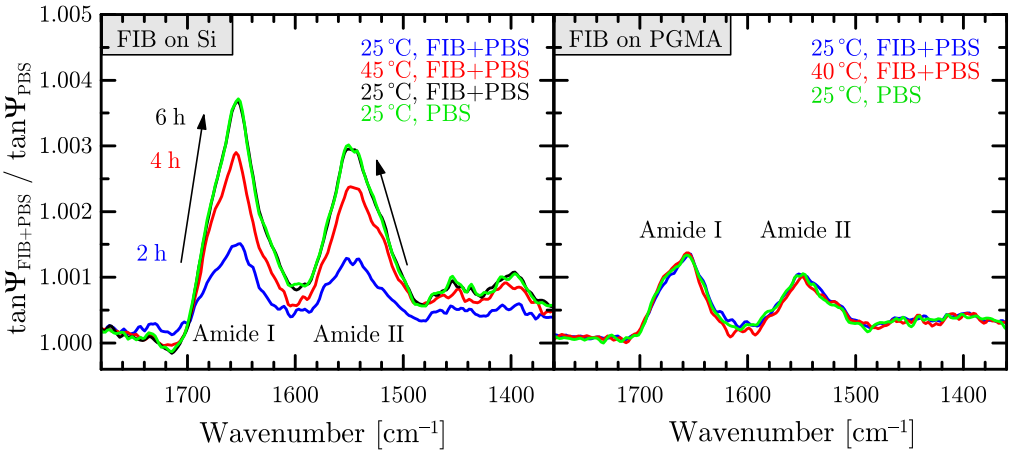

FIGURE 5.22: IR-SE spectra of FIB adsorption at 0.25 mg/ml to a bare silicon surface (left) and a 2.5 nm thin PGMA layer (right). The spectra are referenced to the respective sample in plain PBS buffer solution. Adsorptions were performed for several hours until no further increase in protein signal was detected. Spectra shown in green were recorded after the adsorption experiment with the layers immersed in pure PBS buffer solution.

Similar observations were made for the thin PGMA layer. However, on PGMA the adsorption process was completed after only about 10 minutes and the adsorbed amount is much lower than on silicon. A temperature increase up to 40 °C did not increase the adsorbed amount and neither did any of it desorb during the buffer rinse.

After the in situ experiments, the average protein layer thickness and refractive index in dry state were determined with ex situ VIS ellipsometry. It resulted in $n_\infty = 1.65$ and $d_{dry} = (20 \pm 2)$ nm on silicon and $_{dry} = (7 \pm 1)$ nm on PGMA. These values are consistent with FIB's optical properties [160]. It seems that FIB has a different affinity towards the silicon surface than to PGMA [161]. On PGMA, the maximum adsorbed layer thickness was reached after about 10 minutes, while on silicon it took about 2 hours for a similar amount to adsorb. The adsorption process on silicon continued for several hours until maximum layer thickness on silicon was reached, with the FIB layer being three times as thick as on PGMA. A possible explanation is as follows: The strength of initial FIB adsorption on the more hydrophilic silicon surface is low, enabling surface reorganization which leads to a higher surface coverage or maybe even multilayer formation [162]. On PGMA however, initial adsorption is too strong to enable reorientation. FIB adsorbs strongly upon contact with the surface leading to a quick adsorption process and probably some chemical attachment via reaction between amino acid residues and PGMA's epoxy groups [48].

In figure 5.23 the in situ tanΨ spectra of adsorbed FIB layers on Si and PGMA after a buffer rinse are displayed in the same plot window to be able to directly compare the amide band shape. It is evident that the band envelope is different for FIB adsorbed on the two substrates. On Si (black spectrum), amide I shows increased intensity in the range of 1630–1600 cm^{-1} and decreased intensity in the range of 1690–1670 cm^{-1} compared to the amide I band shape on PGMA (grey spectrum). Amide II is of higher intensity on Si in the range of 1540–1500 cm^{-1}. The changes might be related to a different secondary structure on the two surfaces. According to literature [138, 163] the above mentioned spectral ranges of the amide I band are correlated with vibrational modes of β-sheets ($\sim$1630 cm^{-1}) and turns (1682–1662 cm^{-1}), indicating less β-sheets

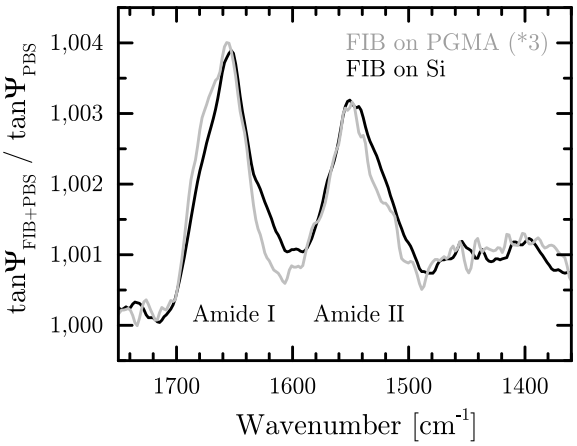

FIGURE 5.23: Direct comparison of IR-SE spectra of FIB adsorption to silicon and PGMA. Displayed are the green spectra from figure 5.22 on Si and PGMA (adsorbed FIB after a buffer rinse at 25 °C), with the intensity of the spectrum on PGMA increased by a factor of 3.

and more turn structures in FIB adsorbed on PGMA. Together with the observed fast adsorption rate on PGMA we conclude that fibrinogen has a higher affinity towards the hydrophobic PGMA surface and undergoes changes in its secondary structure to increase the area of interaction with the surface.

5.3.2 Fibrinogen adsorption experiments on PNIPAAm-*b*-PGMA brushes

In the special case of PNIPAAm-*b*-PGMA copolymer brushes, we were interested in the protein affinity compared to traditional PNIPAAm brushes. As mentioned in the beginning of this section, PNIPAAm layers of similar structure and thickness are known to be protein-repellent, especially in the swollen state below the LCST [43, 45, 47]. Recent studies of our group [75] about the detailed switching behavior of PNIPAAm brushes revealed that the brushes in their collapsed state are less hydrophobic than previously thought. Similar findings have also been made by Brouette et al. [46]. This might be the reason for PNIPAAm's protein-resistancy below as well as above its LCST. PGMA layers on the other hand have a high affinity towards proteins because of their hydrophobicity [48, 164].

Due to the incorporation of PGMA blocks the PNIPAAm-*b*-PGMA brushes are more hydrophobic than traditional PNIPAAm brushes [63] and could have a higher affinity towards proteins than pure PNIPAAm brushes. Especially at temperatures above PNIPAAm's LCST, when the PNIPAAm chains are collapsed, it might be possible for PGMA domains to be exposed on the surface and accessible for protein adsorption. FIB adsorption studies below and above the LCST are a good indicator for the presence of PGMA segments at the interface.

The samples were measured via in situ VIS and IR ellipsometry in PBS buffer solutions (pH 7.4) containing 0.25 mg/ml FIB (see section 3.1.3). VIS ellipsometry experiments were done by Eva Bittrich at IPF Dresden, while IR-SE experiments were performed at ISAS in Berlin. Different experimental setups of the in situ cell for VIS and IR measurements required the brushes to be prepared on different substrates. The parameters of the brush samples are summarized in table 4.6.

Similar results were obtained with the two methods: Up to 40 °C no protein adsorption on PNIPAAm-*b*-PGMA brushes was detected. Thickness and refractive index values of VIS ellipsometric measurements stayed about the same as they were in plain PBS solution at the respective temperature (table 5.6).

IR-SE tanΨ spectra show only those changes that occur due to the temperature-dependent switching behavior of the brush (figure 5.24) but no protein amide bands. These results indicate a PNIPAAm-dominated brush–solution interface of PNIPAAm-*b*-PGMA brushes. Although AR-XPS measurements revealed the presence of some PGMA segments in the topmost part of the brush layers [63], these segments are sufficiently screened by PNIPAAm which prevents FIB adsorption. These results indicate a brush–solution interface that is dominated by PNIPAAm chains, both above and below the LCST of PNIPAAm. It seems that PNIPAAm's hydrophilic characteristic, even in its collapsed state, prevents interaction with the protein. It underlines previous observations made in our group [75] and also in literature [46], that PNIPAAm in its collapsed state is still hydrophilic, and that the hydration of the PNIPAAm chains prevents polymer–protein interaction.

TABLE 5.6: VIS ellipsometry results on switching behavior and protein adsorption experiments on PNIPAAm-*b*-PGMA brushes. The values were determined via a layered optical box model [165]. Errors of d and n are less than 0.5 nm and 0.003, respectively.

	PNI-70		PNI-40	
Experiment	d [nm]	n (633 nm)	d [nm]	n (633 nm)
dry	26.1	1.555	25.4	1.482
PBS 18 °C	26.3	1.510	25.6	1.505
PBS 40 °C	26.3	1.504	27.9	1.484
FIB/PBS 40 °C	26.9	1.500	28.2	1.481
PBS 40 °C	27.1	1.498	27.8	1.463
PBS 55 °C	32.5	1.477	36.4	1.446
FIB/PBS 55 °C	37.2	1.473	40.3	1.441
PBS 55 °C	36.6	1.476	46.1	1.437

Experiments at higher temperatures up to 55 °C, however, revealed some differences. In PBS the brush thickness determined with VIS ellipsometry increased several nanometers in accordance with a decreasing refractive index of the swollen layer, indicating a further swelling of the brush (see figure 5.17 and table 5.6). Addition of FIB to the solution at 55 °C resulted in a further increase in thickness (data not shown) and detection of adsorbed protein on the brushes. It was observed that FIB underwent denaturation and precipitated when it was added to the solution at 55 °C.

IR-SE spectra also revealed protein adsorption at 55 °C via the appearance of protein amide bands. Just as it was observed in VIS ellipsometry experiments, FIB precipitation took place in the flow cell. At first, it was suspected that FIB adsorbs more easily in its denatured state, which is the case above 48 °C. However, after a buffer rinse the IR-SE spectrum showed significant differences that cannot be explained solely by FIB adsorption, as can be seen in the lower panel of figure 5.25.

Combined evaluation of VIS and IR results showed that the observed swelling of the PNIPAAm-*b*-PGMA brushes in PBS at temperatures above 40 °C was followed by a detachment of the brushes from the substrate. The detachment was verified by an in situ IR-SE switching experiment of another sample in plain PBS at 25 and 55 °C (figure 5.25,

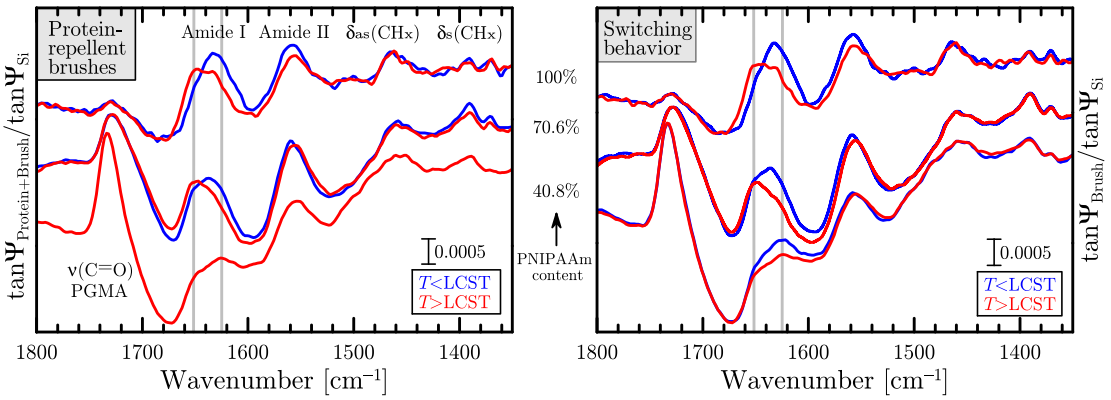

FIGURE 5.24: In situ IR-SE spectra of protein adsorption experiments on PNIPAAm-containing polymer brushes at temperatures above (max. 43 °C) and below PNIPAAm's LCST. Left panel: Pure PNIPAAm brush (100%) immersed in HSA solution and PNIPAAm-*b*-PGMA brushes (70.6% and 40.8%) immersed in FIB solution. Right panel: Spectra of the same brushes recorded in plain buffer solution—but otherwise identical conditions—before the protein experiment. Spectra are referenced to tan Ψ_{Si} of bare silicon substrate in protein-free buffer. Comparing the spectra on the left to the switching signatures in protein-free buffer on the right, no differences are observed, that is, no protein adsorption takes place.

lower panel) and inspection of the wedge directly after the experiment (figure 5.26). The brush seems to have detached like a sheet from the surface, probably in the convective flow during the buffer rinse. Only at the edges of the wedge some polymer remained, because these parts were protected by the teflon seal of the in situ cell frame. Note that detachment only took place in buffer solution. During an identical switching experiment of a PNI-70 brush in plain water the brushes were stable, even at 55 °C (figure 5.25, upper panel).

Ex situ VIS ellipsometric measurements of the samples, that were used for FIB adsorption at 55 °C, were done after the adsorption experiments and revealed a much lower and inhomogeneous 'brush' thickness than before (8–12 nm instead of the initially determined ~25 nm). This supports the hypothesis of partial detachment of the brushes and subsequent protein adsorption on the exposed silicon surface. The measured organic layer thickness of ≤ 12 nm on the samples fits these assumptions, taking into account how long the samples were immersed in protein solution at 55 °C (~2 h) and the estimated adsorbed FIB layer thickness on silicon after this time (see section 5.3.1).

The reason to why the covalent PNIPAAm-*b*-PGMA brushes detached from the silicon substrate around 55 °C is currently unknown. Interestingly, before the switching experiments in PBS solution were performed, all samples had been measured the same way in water where they resisted detachment. We assume the buffer ions that penetrate the brush influence brush stability at this point.

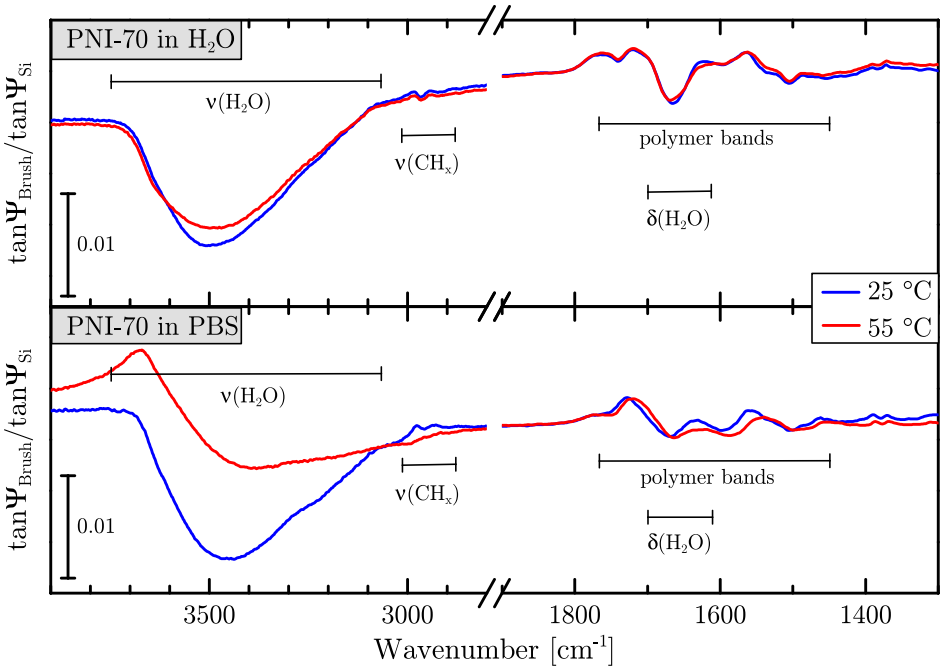

FIGURE 5.25: In situ IR-SE $\tan\Psi_{Brush}$ spectra of PNI-70 at 25 and 55 °C. Upper panel: Brush in water. Lower panel: Brush in PBS. Spectra are referenced to $\tan\Psi_{Si}$ of bare silicon substrate under the same conditions. Note the reduced amplitudes of the polymer bands in the spectrum in PBS at 55 °C, indicating a loss of polymer on the surface.

FIGURE 5.26: Photograph of an intact PNI-70 sample (left) and the damaged sample (right). On the intact sample on the left, one can see the darker and less reflective area of the brush layer, with the edge of the layer visible that results from the dip-coating process. The sample on the right is the one from the experiments shown in figure 5.25, photographed after the in situ experiment at 55 °C. It is clearly damaged, with only parts of the brush layer remaining around the edges, where the layer was protected by the teflon seal of the in situ cell frame.

Summary

In this work, temperature-responsive functional polymer layers have been studied, which are promising in the field of biomedical research, for example as coating material for substrates used in tissue engineering. The behavior of such polymer brushes was characterized in the physiological temperature range, since there is great potential for biomedical applications. One example is the control of attachment and detachment of cells, given that the chosen polymer shows the desired interaction with biomolecules without affecting the function of the biomolecule. A difficult task is to properly characterize the functional behavior of the brushes in situ, especially mixed layers that consist of two or more different polymers and are aimed at combining certain characteristics in one brush. This work took part in a DFG-NSF funded project that aimed at creating polymer brushes, particularly temperature-responsive ones, with the ability to control protein or cell adhesion and detachment. A long term goal is the idea to immobilize growth factors within the brush, that can be presented at the surface in a controlled manner via the functional behavior.

In situ VIS and IR ellipsometry are powerful methods to probe the ultrathin brushes in solution. Results obtained from the two methods complement each other and provide a good understanding of the chemical and physical characteristics of the brushes. In IR-SE, the interactions between functional groups of the polymer and water can be studied via their vibrational modes. In this work special focus was put on the amide I vibration containing mainly the C=O stretching mode. VIS ellipsometry provided complementatry information about swollen thickness and water content of the brushes.

Two different temperature-responsive brush systems, containing either POx or PNIPAAm as the responsive polymer, were studied. Both are biocompatible, non-toxic polymers showing a change from water-soluble to water-insoluble at increasing temperature.

The investigated POx system was composed of a random copolymer of a temperature-responsive POx (*c*PrOx) and a non-responsive, hydrophilic one (MeOx). The copolymer with 25% MeOx content showed nearly the same LCST as PNIPAAm, which is around 32 °C. Additionally, brushes of the pure P*c*PrOx and PMeOx were studied. In IR-SE spectra three different forms of interaction of the C=O vibrational band could be identified: Free C=O and two hydrated states, either hydrogen-bonded to one water molecule (weakly hydrated) or two water molecules (strongly hydrated). In situ spectra of the temperature-responsive pure P*c*PrOx brush revealed that in water only a small fraction of C=O groups remains in the non-interacting state, both below and above the LCST. The strongly hydrated state was found to be the most abundant below the LCST and the interactions changed to an equal abundance of weakly and strongly hydrated states when the temperature was raised to above the LCST. For the copolymer25 brush, similar observations were made but with less prominent changes in the vibrational spectra, because the incorporation of 25% MeOx leads to a higher hydrophilicity and therefore less intense switching behavior of the copolymer brush. A contrary result was obtained from VIS ellipsometry, showing stronger changes in brush thickness during the transition of copolymer25. Combining the resutlts, we conclude that there are

additional water molecules present in the swollen brush. These do not directly interact with polymer chains but contribute to the swelling and collapse of the brush.

Due to the missing N−H group in POx there is no other possibility for C=O groups to form hydrogen bonds, making POx brushes a simple example for the simulation of mixed polymer brushes. In dry state IR-SE spectra, the copolymer composition was successfully simulated using previously determined optical constants of the pure POx brushes. In aqueous environment it was possible to simulate the pure P*c*PrOx and PMeOx spectra in the range of the C=O stretching mode via three oscillator contributions representing the three forms of interaction. However, the PMeOx brush revealed incomplete swelling, that was identified by a lower redshift of the C=O frequency in swollen state compared to the other POx samples and was probably caused by the low molecular weight of PMeOx chains in the pure brush. The C=O moieties in the copolymer25 sample on the other hand—both in *c*PrOx and MeOx sections—were fully hydrated. Using the optical constants from the pure PMeOx brush lead to a bad representation of the MeOx fraction in copolymer25 and consequently to an unsuccessful simulation. To be able to properly simulate the mixed brushes, pure POx brushes with similar molecular weights need to be studied, that show the same hydration in water as the desired mixed brush.

The PNIPAAm-containing brushes were prepared from a block-copolymer of PNIPAAm and the anchoring polymer PGMA. These PNIPAAm-*b*-PGMA brushes were studied as alternative to the well-known traditional PNIPAAm brushes, with focus on the switching behavior and the interaction with proteins below and above PNIPAAm's LCST. The first IR-SE experiments in dry state proved the difficulty to simulate mixed brushes when interactions between the polymers are present. A simulation trial of the mixed PNIPAAm-*b*-PGMA brushes by using optical constants of PNIPAAm and PGMA was not successful. It revealed that the brushes can not be represented by data of the pure polymers, because the PNIPAAm and PGMA blocks are intertwined in the layer where they form additional interactions between their functional groups. Further evaluation was therefore focused on qualitative characterization of the switching behavior, using in situ IR and VIS ellipsometry as well as in situ AFM. Both VIS ellipsometry and AFM experiments showed only a small swelling of the ∼30 nm PNIPAAm-*b*-PGMA layers in cold water and hardly any collapse upon increasing temperature. The results stood in contrast to the strong swelling and deswelling behavior of traditional PNIPAAm brushes. Nevertheless, in situ IR-SE spectra revealed changes of interactions of the amide groups in the PNIPAAm blocks. The changes were less intense than in traditional PNIPAAm brushes, which can be correlated with a decrease of PNIPAAm content in the layer. It was concluded that there is a small amount of water present in the brushes interacting with the PNIPAAm blocks. Changes in temperature result in a change from amide–water to amide–amide interactions but the water molecules remain trapped in the brush. This is caused by the cross-linked hydrophobic PGMA network throughout the brush layer, restricting the mobility of water and PNIPAAm chains and consequently preventing the swelling and collapse of the brush. In situ AFM images revealed a smooth surface of the brushes, both at low and higher temperatures. This lead to the conclusion that only the topmost part of the layer can swell in water, as it is dominated by PNIPAAm blocks.

In the last part, protein adsorption experiments on PNIPAAm-*b*-PGMA brushes were performed to evaluate the presence of PGMA segments at the brush–solution interface. PGMA has a high protein affinity due to its hydrophobicity while PNIPAAm is hydrophilic and mostly protein-repellent. The chosen protein FIB was also adsorbed to

a plain silicon substrate and a thin PGMA layer. On Si the adsorption took much longer and the resulting FIB layer was much thicker than on PGMA. It was concluded that the interaction between silicon and FIB is less strong, enabling reorientation of the elongated protein molecules to form a thicker layer. On PGMA however, hydrophobic interactions lead to strong adsorption and partial unfolding of the protein. On PNIPAAm-*b*-PGMA brushes no FIB adsorption took place. In situ IR-SE spectra only showed the switching behavior in the amide bands. This proves the immediate brush–solution interface to be dominated by PNIPAAm blocks, that sufficiently cover underlying PGMA and prevent any interaction between PGMA and FIB. At this point, IR-SE was advantageous, as it is very sensitive to small amounts of adsorbed biomolecules. Hence, it is an optimal method to study antifouling properties.

Overall, POx brushes can be a suitable alternative to PNIPAAm brushes. The most prominent difference is the missing $\mathrm{N{-}H}$ group in POx. This leads to the impossibility of amide–amide hydrogen-bond interactions and consequently to a slower switching process compared to the abrupt transition of PNIPAAm brushes. Additionally, it can be useful when growth factors are immobilized within a brush. Growth factors are proteins that stimulate cellular growth or proliferation. In IR-SE, using POx brushes can help differentiate between spectral signals of brush and growth factor, which is difficult for PNIPAAm brushes due to their structural similarity to proteins. IR-SE is a valuable tool to distinguish these different vibrational modes and study their interactions with the environment.

The technique also helped to gain insight into the interactions of the mixed PNIPAAm-*b*-PGMA system with water, even though the layers showed no collapse. In future studies involving growth factors, the sensitivity for changes of interactions within the brush can help to identify the influence of the growth factor on the functional brush behavior. IR-SE is an ideal method in this case, because the spectral signals of biomolecules are directly visible and the method is very sensitive to changes of interactions. Complementary (in situ) AFM measurements can provide surface topography images, e. g. to evaluate if the growth factor molecules are sufficiently hidden within the brush layer.

Bibliography

[1] S. Sharma, R. W. Johnson, T. A. Desai, *Langmuir* **2004**, *20*, 348–356, DOI 10.1021/la0347531.

[2] F. Zhang, E. T. Kang, K. G. Neoh, P. Wang, K. L. Tan, *Journal of Biomedical Materials Research: Part A* **2001**, *56*, 324–332, DOI 10.1002/1097-4636(20010905)56:3<324::AID-JBM1100>3.0.CO;2-P.

[3] M. Krishnamoorthy, S. Hakobyan, M. Ramstedt, J. E. Gautrot, *Chemical Reviews* **2014**, *114*, 10976–11026, DOI 10.1021/cr500252u.

[4] P. M. Mendes, *Chemical Society Reviews* **2008**, *37*, 2512–2529, DOI 10.1039/B714635N.

[5] M. Mrksich, *Chemical Society Reviews* **2000**, *29*, 267–273, DOI 10.1039/A705397E.

[6] D. L. Huber, R. P. Manginell, M. A. Samara, B.-I. Kim, B. C. Bunker, *Science* **2003**, *301*, 352–354, DOI 10.1126/science.1080759.

[7] Q. Yu, Y. Zhang, H. Chen, F. Zhou, Z. Wu, H. Huang, J. L. Brash, *Langmuir* **2010**, *26*, 8582–8588, DOI 10.1021/la904663m.

[8] C. Xue, B.-C. Choi, S. Choi, P. V. Braun, D. E. Leckband, *Advanced Functional Materials* **2012**, *22*, 2394–2401, DOI 10.1002/adfm.201103056.

[9] N. Joseph, T. Prasad, V. Raj, P. R. Anil-Kumar, K. Sreenivasan, T. V. Kumary, *Journal of Bioactive and Compatible Polymers* **2010**, *25*, 58–74, DOI 10.1177/0883911509353481.

[10] D. Aulich, O. Hoy, I. Luzinov, M. Brücher, R. Hergenröder, E. Bittrich, K.-J. Eichhorn, P. Uhlmann, M. Stamm, N. Esser, K. Hinrichs, *Langmuir* **2010**, *26*, 12926–12932, DOI 10.1021/la101762f.

[11] O. Hoy, B. Zdyrko, R. Lupitskyy, R. Sheparovych, D. Aulich, J. Wang, E. Bittrich, K.-J. Eichhorn, P. Uhlmann, K. Hinrichs, M. Müller, M. Stamm, S. Minko, I. Luzinov, *Advanced Functional Materials* **2010**, *20*, 2240–2247, DOI 10.1002/adfm.201000170.

[12] T. Wu, P. Gong, I. Szleifer, P. Vlček, V. Šubr, J. Genzer, *Macromolecules* **2007**, *40*, 8756–8764, DOI 10.1021/ma0710176.

[13] E. Bittrich, M. Kuntzsch, K.-J. Eichhorn, P. Uhlmann, *Journal of Polymer Science: Part B: Polymer Physics* **2010**, *48*, 1606–1615, DOI 10.1002/polb.22021.

[14] T. Okano, N. Yamada, H. Sakai, Y. Sakurai, *Journal of Biomedical Materials Research* **1993**, *27*, 1243–1251, DOI 10.1002/jbm.820271005.

[15] S. Balamurugan, S. Mendez, S. S. Balamurugan, M. J. O'Brien-II, G. P. López, *Langmuir* **2003**, *19*, 2545–2549, DOI 10.1021/la026787j.

[16] A. Furchner, E. Bittrich, P. Uhlmann, K.-J. Eichhorn, K. Hinrichs, *Thin Solid Films* **2013**, *541*, 41–45, DOI 10.1016/j.tsf.2012.10.135.

[17] A. Dworak, A. Utrata-Wesołek, N. Oleszko, W. Wałach, B. Trzebicka, J. Anioł, A. L. Sieroń, A. Klama-Baryła, M. Kawecki, *Journal of Materials Science: Materials in Medicine* **2014**, *25*, 1149–1163, DOI 10.1007/s10856-013-5135-7.

[18] M. R. Islam, Y. Gao, X. Li, Q. M. Zhang, M. Wei, M. J. Serpe, *Chinese Science Bulletin* **2014**, *59*, 4237–4255, DOI 10.1007/s11434-014-0545-6.

[19] J. Thévenot, H. Oliveira, O. Sandre, S. Lecommandoux, *Chemical Society Reviews* **2013**, *42*, 7099–7116, DOI 10.1039/C3CS60058K.

[20] E. Wischerhoff, N. Badi, J.-F. Lutz, A. Laschewsky, *Soft Matter* **2010**, *6*, 705–713, DOI 10.1039/B913594D.

[21] P. G. deGennes, *Macromolecules* **1980**, *13*, 1069–1075, DOI 10.1021/ma60077a009.

[22] S. T. Milner, *Science* **1991**, *251*, 905–914, DOI 10.1126/science.251.4996.905.

[23] W. J. Brittain, S. Minko, *Journal of Polymer Science: Part A: Polymer Chemistry* **2007**, *45*, 3505–3512, DOI 10.1002/pola.22180.

[24] M. Heskins, J. E. Guillet, *Journal of Macromolecular Science Part A: Chemistry* **1968**, *8*, 1441–1455, DOI 10.1080/10601326808051910.

[25] Y. Katsumoto, T. Tanaka, H. Sato, Y. Ozaki, *Journal of Physical Chemistry A* **2002**, *106*, 3429–3435, DOI 10.1021/jp0124903.

[26] T. Chen, R. Ferris, J. Zhang, R. Ducker, S. Zauscher, *Progress in Polymer Science* **2010**, *35*, 94–112, DOI 10.1016/j.progpolymsci.2009.11.004.

[27] M. Nakayama, T. Okano, F. M. Winnik, *Material Matters* **2010**, *5.3*, 56, http://www.sigmaaldrich.com/technical-documents/articles/material-matters/poly-n-isopropylacrylamide.html.

[28] E. Bittrich, S. Burkert, M. Müller, K.-J. Eichhorn, M. Stamm, P. Uhlmann, *Langmuir* **2012**, *28*, 3439–3448, DOI 10.1021/la204230a.

[29] C. Hashimoto, A. Nagamoto, T. Maruyama, N. Kariyama, Y. Irisa, A. Ikehata, Y. Ozaki, *Macromolecules* **2013**, *46*, 1041–1053, DOI 10.1021/ma302317m.

[30] R. Hoogenboom, H. M. L. Thijs, M. J.H. C. Jochems, B. M. van Lankvelt, M. W. M. Fijten, U. S. Schubert, *Chemical Communications* **2008**, *1*, 5758–5760, DOI 10.1039/b813140f.

[31] M. M. Bloksma, C. Weber, I. Y. Perevyazko, A. Kuse, A. Baumgärtel, A. Vollrath, R. Hoogenboom, U. S. Schubert, *Macromolecules* **2011**, *44*, 4057–4064, DOI 10.1021/ma200514n.

[32] Y. Katsumoto, A. Tsuchiizu, X. Qiu, F. M. Winnik, *Macromolecules* **2012**, *45*, 3531–3541, DOI 10.1021/ma300252e.

[33] N. Zhang, R. Luxenhofer, R. Jordan, *Macromolecular Chemistry and Physics* **2012**, *213*, 1963–1969, DOI 10.1002/macp.201200261.

[34] R. M. A. Azzam in *Handbook of Optics*, (Ed.: M. Bass), McGraw Hill, New York, **2010**, pp. 16.1–16.25.

[35] H. G. Tompkins, E. A. Irene, *Handbook of Ellipsometry*, Springer, Heidelberg, **2005**.

[36] H. Fujiwara, *Spectroscopic Ellipsometry, Principles and Applications*, John Wiley & Sons, Ltd, Chichester, **2007**.

[37] K. Hinrichs, K.-J. Eichhorn, *Ellipsometry of Functional Organic Surfaces and Films*, Springer Series in Surface Sciences, Volume 52, Heidelberg, **2014**.

[38] H. Arwin, *Thin Solid Films* **2000**, *377–378*, 48–56, DOI 10.1016/S0040-6090(00)01385-7.

[39] A. Röseler, *Infrared Spectroscopic Ellipsometry*, Akademie-Verlag, Berlin, **1990**.

[40] E. H. Korte, A. Röseler, *Analyst* **1998**, *123*, 647–651, DOI 10.1039/A707112D.

[41] A. Röseler, E.-H. Korte in *Handbook of Vibrational Spectroscopy*, *Vol. 2*, (Eds.: J. Chalmers, P. Griffiths), John Wiley & Sons, Ltd, **2002**.

[42] Y. Mikhaylova, L. Ionov, J. Rappich, M. Gensch, N. Esser, S. Minko, K.-J. Eichhorn, M. Stamm, K. Hinrichs, *Analytical Chemistry* **2007**, *79*, 7676–7682, DOI 10.1021/ac070853a.

[43] S. Burkert, E. Bittrich, M. Kuntzsch, M. Müller, K.-J. Eichhorn, C. Bellmann, P. Uhlmann, M. Stamm, *Langmuir* **2010**, *26*, 1786–1795, DOI 10.1021/la902505q.

[44] Q. Yu, Y. Zhang, H. Chen, Z. Wu, H. Huang, C. Cheng, *Colloids and Surfaces B: Biointerfaces* **2010**, *76*, 468–474, DOI 10.1016/j.colsurfb.2009.12.006.

[45] C. Xue, N. Yonet-Tanyeri, N. Brouette, M. Sferrazza, P. V. Braun, D. E. Leckband, *Langmuir* **2011**, *27*, 8810–8818, DOI 10.1021/la2001909.

[46] N. Brouette, C. Xue, M. Haertlein, M. Moulin, G. Fragneto, D. E. Leckband, A. Halperin, M. Sferrazza, *The European Physical Journal Special Topics* **2012**, *213*, 343–353, DOI 10.1140/epjst/e2012-01681-4.

[47] A. Furchner, PhD thesis, Technische Universität Berlin, **2014**, http://nbn-resolving.de/urn:nbn:de:kobv:83-opus4-50904.

[48] B. Zdyrko, O. Hoy, I. Luzinov, *Biointerphases* **2009**, *4*, FA17–FA21, DOI 10.1116/1.3101907.

[49] V. R. de-la Rosa, *Journal of Materials Science: Materials in Medicine* **2014**, *25*, 1211–1225, DOI 10.1007/s10856-013-5034-y.

[50] H. Chen, L. Yuan, W. Song, Z. Wu, D. Li, *Progress in Polymer Science* **2008**, *33*, 1059–1087, DOI 10.1016/j.progpolymsci.2008.07.006.

[51] J. E. Raynor, J. R. Capadona, D. M. Collard, T. A. Petrie, A. J. García, *Biointerphases* **2009**, *4*, FA3–FA16, DOI 10.1116/1.3089252.

[52] M. Nakayama, N. Yamada, Y. Kumashiro, H. Kanazawa, M. Yamato, T. Okano, *Macromolecular Bioscience* **2012**, *12*, 751–760, DOI 10.1002/mabi.201200018.

[53] S. Fujishige, K. Kubota, I. Ando, *ACS The Journal of Physical Chemistry* **1989**, *93*, 3311–3313, DOI 10.1021/j100345a085.

[54] G. Karlström, O. Engkvist in *Poly(ethylene glycol) - Chemistry and Biological Applications*, (Eds.: J. Harris, S. Zalipsky), American Chemical Society, **1997**.

[55] C. Weber, R. Hoogenboom, U. S. Schubert, *Progress in Polymer Science* **2012**, *37*, 686–714, DOI 10.1016/j.progpolymsci.2011.10.002.

[56] M. Agrawal, J. C. Rueda, P. Uhlmann, M. Müller, F. Simon, M. Stamm, *ACS Applied Materials and Interfaces* **2012**, *4*, 1357–1364, DOI 10.1021/am2016188.

[57] B. Pidhatika, M. Rodenstein, Y. Chen, E. Rakhmatullina, A. Mühlebach, C. Acikgoz, M. Textor, R. Konradi, *Biointerphases* **2012**, *7*, 1–15, DOI 10.1007/s13758-011-0001-y.

[58] J. Ulbricht, R. Jordan, R. Luxenhofer, *Biomaterials* **2014**, *35*, 4848–4861, DOI 10.1016/j.biomaterials.2014.02.029.

[59] C. W. McGary, *Journal of Polymer Science* **1960**, *46*, 51–57, DOI 10.1002/pol.1960.1204614705.

[60] K. S. Iyer, B. Zdyrko, H. Malz, J. Pionteck, I. Luzinov, *Macromolecules* **2003**, *36*, 6519–6526, DOI 10.1021/ma034460z.

[61] B. Zdyrko, I. Luzinov, *Macromolecular Rapid Communications* **2011**, *32*, 859–869, DOI 10.1002/marc.201100162.

[62] S. Minko, *Journal of Macromolecular Science Part C: Polymer Reviews* **2006**, *46*, 397–420, DOI 10.1080/15583720600945402.

[63] M. Seeber, PhD thesis, Clemson University, **2013**, http://tigerprints.clemson.edu/all\textbackslash_dissertations/1138.

[64] B. S. Lokitz, J. Wei, J. P. Hinestrosa, I. Ivanov, J. F. Browning, J. F. Ankner, S. M. Kilbey-II, J. M. Messman, *Macromolecules* **2012**, *45*, 6438–6449, DOI 10.1021/ma300991p.

[65] R. Hoogenboom, *Angewandte Chemie International Edition* **2009**, *48*, 7978–7994, DOI 10.1002/anie.200901607.

[66] V. P. Tolstoy, I. V. Chernyshova, V. A. Skryshevsky, *Handbook of Infrared Spectroscopy of Ultrathin Films*, John Wiley & Sons, Ltd, Hoboken, New Jersey, **2003**.

[67] Y. Katsumoto, T. Tanaka, K. Ihara, M. Koyama, Y. Ozaki, *Journal of Physical Chemistry B* **2007**, *111*, 12730–12737, DOI 10.1021/jp0750452.

[68] G. Eaton, P. P. Rastogi, M. C. R. Symons, *Journal of the Chemical Society Faraday Transactions 1: Physical Chemistry in Condensed Phases* **1989**, *85*, 3257–3271, DOI 10.1039/F19898503257.

[69] G. A. Petsko, D. Ringe, *Protein Structure and Function*, New Science Press Ltd, London, **2004**.

[70] E. V. Anslyn, D. A. Dougherty, *Modern Physical Organic Chemistry*, University Science Books, Sausalito, **2006**.

[71] Y. Maeda, T. Nakamura, I. Ikeda, *Macromolecules* **2001**, *34*, 1391–1399, DOI 10.1021/ma001306t.

[72] O. Ramon, E. Kesselman, R. Berkovici, Y. Cohen, Y. Paz, *Journal of Polymer Science: Part B: Polymer Physics* **2001**, *39*, 1665–1677, DOI 10.1002/polb.1138.

[73] Y. Katsumoto, T. Tanaka, Y. Ozaki, *Macromolecular Symposia* **2004**, *205*, 209–223, DOI 10.1002/masy.200450120.

[74] M. R. Islam, A. Ahiabu, X. Li, M. J. Serpe, *Sensors* **2014**, *14*, 8984–8995, DOI 10.3390/s140508984.

[75] A. Furchner, A. Kroning, S. Rauch, P. Uhlmann, K.-J. Eichhorn, K. Hinrichs, *Analytical Chemistry* **2017**, *89*, 3240–3244, DOI 10.1021/acs.analchem.7b00208.

[76] T. G. Bassiri, A. Levy, M. Litt, *Polymer Letters* **1967**, *5*, 871–879, DOI 10.1002/pol.1967.110050927.

[77] T. Kagiya, S. Narisawa, T. Maeda, K. Fukui, *Polymer Letters* **1966**, *4*, 257–260, DOI 10.1002/pol.1966.110040405.

[78] W. Seeliger, E. Aufderhaar, W. Diepers, R. Feinauer, R. Nehring, W. Thier, H. Hellmann, *Angewandte Chemie International Edition* **1966**, *5*, 875–888, DOI 10.1002/anie.196608751.

[79] D. A. Tomalia, D. P. Sheetz, *Journal of Polymer Science: Part A-1* **1966**, *4*, 2253–2265, DOI 10.1002/pol.1966.150040919.

[80] F. Rehfeldt, M. Tanaka, *Langmuir* **2002**, *18*, 4908–4914, DOI 10.1021/la0112559.

[81] B.-J. Chang, O. Prucker, E. Groh, A. Wallrath, M. Dahm, J. Rühe, *Colloids and Surfaces A: Physicochemical and Engineering Aspects* **2002**, *198–200*, 519–526, DOI 10.1016/S0927-7757(01)00952-9.

[82] R. Konradi, B. Pidhatika, A. Mühlebach, M. Textor, *Langmuir* **2008**, *24*, 613–616, DOI 10.1021/la702917z.

[83] R. Konradi, C. Acikgoz, M. Textor, *Macromolecular Rapid Communications* **2012**, *33*, 1663–1676, DOI 10.1002/marc.201200422.

[84] B. Pidhatika, J. Möller, E. M. Benetti, R. Konradi, E. Rakhmatullina, A. Mühlebach, R. Zimmermann, C. Werner, V. Vogel, M. Textor, *Biomaterials* **2010**, *31*, 9462–9472, DOI 10.1016/j.biomaterials.2010.08.033.

[85] M. Glassner, K. Lava, V. R. de-la Rosa, R. Hoogenboom, *Journal of Polymer Science Part A: Polymer Chemistry* **2014**, *52*, 3118–3122, DOI 10.1002/pola.27364.

[86] C. Diehl, P. Cernoch, I. Zenke, H. Runge, R. Pitschke, J. Hartmann, B. Tiersch, H. Schlaad, *Soft Matter* **2010**, *6*, 3784–3788, DOI 10.1039/C0SM00114G.

[87] T. Li, H. Tang, P. Wu, *Langmuir* **2015**, *31*, 6870–6878, DOI 10.1021/acs.langmuir.5b01009.

[88] N. Zhang, T. Pompe, I. Amin, R. Luxenhofer, C. Werner, R. Jordan, *Macromolecular Bioscience* **2012**, *12*, 926–936, DOI 10.1002/mabi.201200026.

[89] H. Ma, D. Li, X. Sheng, B. Zhao, A. Chilkoti, *Langmuir* **2006**, *22*, 3751–3756, DOI 10.1021/la052796r.

[90] X. Chen, H. E. Canavan, D. J. Graham, D. G. Castner, B. D. Ratner, *Biointerphases* **2006**, *1*, 61–72, DOI 10.1116/1.2187980.

[91] D. W. Ball, *The Basics of Spectroscopy*, SPIE Press, Bellingham, **2001**.

[92] A. Röseler in *Analytiker Taschenbuch*, *Vol. 14*, (Eds.: H. Günzler, A. Bahadir, R. Borsdorf, K. Danzer, W. Fresenius, R. Galensa, W. Huber, I. Lüderwald, G. Schwedt, G. Tölg, H. Wisser), Springer, **1996**.

[93] J. L. Keddie, *Current Opinion in Colloid & Interface Science* **2001**, *6*, 102–110, DOI 10.1016/S1359-0294(01)00070-X.

[94] H. Günzler, H.-M. Heise, *IR Spektroskopie - Eine Einführung*, Wiley-VCH, Weinheim, **1996**.

[95] R. M. A. Azzam, *Surface Science* **1976**, *56*, 6–18, DOI 10.1016/0039-6028(76)90430-1.

[96] G. E. Jellison-Jr, *Thin Solid Films* **1993**, *234*, 416–422, DOI 10.1016/0040-6090(93)90298-4.

[97] E. H. Korte, K. Hinrichs, A. Röseler, *Spectrochimica Acta Part B* **2002**, *57*, 1625–1634, DOI 10.1016/S0584-8547(02)00100-3.

[98] J. N. Hilfiker, N. Singh, T. Tiwald, D. Convey, S. M. Smith, J. H. Baker, H. G. Tompkins, *Thin Solid Films* **2008**, *516*, 7979–7989, DOI 10.1016/j.tsf.2008.04.060.

[99] M. Losurdo, M. Bergmair, G. Bruno, D. Cattelan, C. Cobet, A. deMartino, K. Fleischer, Z. Dohcevic-Mitrovic, N. Esser, M. Galliet, R. Gajic, D. Hemzal, K. Hingerl, J. Humlicek, R. Ossikovski, Z. V. Popovic, O. Saxl, *Journal of Nanoparticle Research* **2009**, *11*, 1521–1554, DOI 10.1007/s11051-009-9662-6.

[100] L. D. Landau, E. M. Lifshitz, *Electrodynamics of Continuous Media*, Pergamon Press, Oxford, **1984**.

[101] J. M. Bennett in *Handbook of Optics*, (Ed.: M. Bass), McGraw Hill, New York, **2010**, pp. 12.1–12.31.

[102] R. M. A. Azzam, N. M. Bashara, *Ellipsometry and Polarized Light*, Elsevier, Amsterdam, **1987**.

[103] B. Voigtländer, *Scanning Probe Microscopy*, Springer, Heidelberg, **2015**.

[104] P. Eaton, P. West, *Atomic Force Microscopy*, Oxford University Press, Oxford, **2010**.

[105] C. R. Blanchard, *The Chemical Educator* **1996**, *1*, 1–8, DOI 10.1007/s00897960059a.

[106] R. García, R. Pérez, *Surface Science Reports* **2002**, *47*, 197–301, DOI 10.1016/S0167-5729(02)00077-8.

[107] B. Pittenger, N. Erina, C. Su, Quantitative Mechanical Property Mapping at the Nanoscale with PeakForce QNM, AN128, application note, Veeco Instruments Inc., **2010**, https://www.analytic-news.com/papers/pdf/scienceanalyticse1.pdf.

[108] S. Adam, PhD thesis, Technische Universität Dresden, **2016**, http://www.qucosa.de/fileadmin/data/qucosa/documents/21156/Thesis_Stefan_Adam_PDFA-2b.pdf.

[109] M. T. Zarka, O. Nuyken, R. Weberskirch, *Chemistry – A European Journal* **2003**, *9*, 3228–3234, DOI 10.1002/chem.200304729.

[110] J. C. Rueda, S. Zschoche, H. Komber, F. Krahl, K.-F. Arndt, B. Voit, *Macromolecular Chemistry and Physics* **2010**, *211*, 706–716, DOI 10.1002/macp.200900437.

[111] S. Adam, K.-J. Eichhorn, U. Oertel, M. Stamm, P. Uhlmann, "The thermo-responsive behavior of novel Poly(2-oxazolines) in solution and as polymer brushes", in preparation.

[112] M. Litt, F. Rahl, L. G. Roldan, *Journal of Polymer Science: Part A-2* **1969**, *7*, 463–473, DOI 10.1002/pol.1969.160070302.

[113] K. N. Plunkett, X. Zhu, J. S. Moore, D. E. Leckband, *Langmuir* **2006**, *22*, 4259–4266, DOI 10.1021/la0531502.

[114] K. Hinrichs, M. Gensch, N. Nikonenko, J. Pionteck, K.-J. Eichhorn, *Macromolecular Symposia* **2005**, *230*, 26–32, DOI 10.1002/masy.200551138.

[115] Cauchy and related Empirical Dispersion Formulae for Transparent Materials, TN14, technical note, Horiba, **2006**, http://www.horiba.com/fileadmin/uploads/Scientific/Downloads/OpticalSchool_CN/TN/ellipsometer/Cauchy_and_related_empirical_dispersion_Formulae_for_Transparent_Materials.pdf.

[116] U. Richter, G. Dittmar, H. Ketelsen, SpectraRay/3 Software manual, SENTECH Instruments GmbH, **2012**.

[117] D. A. G. Bruggeman, *Annalen der Physik* **1935**, *24*, 636–664, DOI 10.1002/andp.19354160705.

[118] K. Hinrichs, K. Roodenko, J. Rappich, *Electrochemistry Communications* **2008**, *10*, 315–318, DOI 10.1016/j.elecom.2007.12.014.

[119] D. J. Sutor, *Journal of the Chemical Society* **1963**, 1105–1110, DOI 10.1039/JR9630001105.

[120] G. R. Desiraju, *Accounts of Chemical Research* **1996**, *29*, 441–449, DOI 10.1021/ar950135n.

[121] J. J. Turner in *Handbook of Vibrational Spectroscopy*, *Vol. 1*, (Eds.: J. Chalmers, P. Griffiths), John Wiley & Sons, Ltd, Chichester, **2002**.

[122] H. E. Simmons, E. P. Blanchard, H. E. Hartzler, *The Journal of Organic Chemistry* **1966**, *31*, 295–301, DOI 10.1021/jo01339a066.

[123] E. Pretsch, P. Bühlmann, C. Affolter, *Structure Determination of Organic Compounds, Tables of Spectral Data*, 3rd ed., Springer, Berlin Heidelberg, **2000**.

[124] J. B. Lambert, *Introduction to Organic Spectroscopy*, Macmillan, New York, **1987**.

[125] J. Coates in *Encyclopedia of Analytical Chemistry*, (Ed.: R. Meyers), John Wiley & Sons, Ltd, Chichester, **2000**, pp. 10815–10837.

[126] B. H. Stuart, *Infrared Spectroscopy: Fundamentals and Applications*, John Wiley & Sons, Ltd, Chichester, **2004**.

[127] A. D. Rakić, A. B. Djurišic, J. M. Elazar, M. L. Majewski, *Applied Optics* **1998**, *37*, 5271–5283, DOI 10.1364/AO.37.005271.

[128] D. N. Sathyanarayana, *Vibrational Spectroscopy: Theory and Applications*, New Age International, New Delhi, **2004**.

[129] *Handbook of Optical Constants of Solids*, (Ed.: E. D. Palik), Academic Press, San Diego, **1985**.

[130] I. Luzinov, D. Julthongpiput, H. Malz, J. Pionteck, V. V. Tsukruk, *Macromolecules* **2000**, *33*, 1043–1048, DOI 10.1021/ma990926v.

[131] J. Draper, S. Minko, I. Tokarev, M. Stamm, I. Luzinov, *Langmuir* **2004**, *20*, 4064–4075, DOI 10.1021/la0361316.

[132] K. Hinrichs, A. Röseler, M. Gensch, E. H. Korte, *Thin Solid Films* **2004**, *455–456*, 266–271, DOI 10.1016/j.tsf.2004.01.011.

[133] F. Meeussen, E. Nies, H. Berghmans, S. Verbrugghe, E. Goethals, F. DuPrez, *Polymer* **2000**, *41*, 8597–8602, DOI 10.1016/S0032-3861(00)00255-X.

[134] A. Kroning, A. Furchner, S. Adam, P. Uhlmann, K. Hinrichs, *Biointerphases* **2016**, *11*, 019005, DOI 10.1116/1.4939249.

[135] Y. Maréchal, *Journal of Chemical Physics* **1991**, *95*, 5565–5573, DOI 10.1063/1.461630.

[136] Y. Katsumoto, T. Tanaka, Y. Ozaki, *Journal of Physical Chemistry B* **2005**, *109*, 20690–20696, DOI 10.1021/jp052263r.

[137] I. A. Paun, V. Ion, C.-R. Luculescu, M. Dinescu, S. Canulescu, J. Schou, *Applied Physics A* **2012**, *109*, 223–232, DOI 10.1007/s00339-012-7038-8.

[138] A. Barth, *Biochimica et Biophysica Acta–Bioenergetics* **2007**, *1767*, 1073–1101, DOI 10.1016/j.bbabio.2007.06.004.

[139] H. B. Henbest, G. D. Meakins, B. Nicholls, K. J. Taylor, *Journal of the Chemical Society* **1957**, *1*, 1459–1462, DOI 10.1039/JR9570001459.

[140] Y. Maeda, T. Higuchi, I. Ikeda, *Langmuir* **2000**, *16*, 7503–7509, DOI 10.1021/la0001575.

[141] A. Kroning, A. Furchner, D. Aulich, E. Bittrich, S. Rauch, P. Uhlmann, K.-J. Eichhorn, M. Seeber, I. Luzinov, S. M. Kilbey-II, B. S. Lokitz, S. Minko, K. Hinrichs, *ACS Applied Materials and Interfaces* **2015**, *7*, 12430–12439, DOI 10.1021/am5075997.

[142] T. Fukuda, N. Kohara, Y. Onogi, H. Inagaki, *Journal of Applied Polymer Science* **1991**, *43*, 2201–2205, DOI 10.1002/app.1991.070431207.

[143] G. Walsh, *Proteins. Biochemistry and Biotechnology*, John Wiley & Sons, Ltd, Chichester, **2002**.

[144] V. M. Balcão, M. M.D. C. Vila, *Advanced Drug Delivery Reviews* **2015**, *93*, 25–41, DOI 10.1016/j.addr.2014.10.005.

[145] W. Norde, *Macromolecular Symposia* **1996**, *103*, 5–18, DOI 10.1002/masy.19961030104.

[146] K. Atacan, B. Çakıroğlu, M. Özacar, *Food Chemistry* **2016**, *212*, 460–468, DOI 10.1016/j.foodchem.2016.06.011.

[147] L. S. Wong, F. Khan, J. Micklefield, *Chemical Reviews* **2009**, *109*, 4025–4053, DOI 10.1021/cr8004668.

[148] L. Vroman, *Annals of the New York Academy of Sciences* **1987**, *516*, 300–305, DOI 10.1111/j.1749-6632.1987.tb33050.x.

[149] B. D. Ratner, S. J. Bryant, *Annual Review of Biomedical Engineering* **2004**, *6*, 41–75, DOI 10.1146/annurev.bioeng.6.040803.140027.

[150] M. Malmsten, *Journal of Colloid and Interface Science* **1998**, *207*, 186–199, DOI 10.1006/jcis.1998.5763.

[151] P. Uhlmann, N. Houbenov, N. Brenner, K. Grundke, S. Burkert, M. Stamm, *Langmuir* **2007**, *23*, 57–64, DOI 10.1021/la061557g.

[152] E. P. K. Currie, W. Norde, M. A. Cohen-Stuart, *Advances in Colloid and Interface Science* **2003**, *100–102*, 205–265, DOI 10.1016/S0001-8686(02)00061-1.

[153] R. S. Kane, P. Deschatelets, G. M. Whitesides, *Langmuir* **2003**, *19*, 2388–2391, DOI 10.1021/la020737x.

[154] L. E. Averett, M. H. Schoenfisch, *Analyst* **2010**, *135*, 1201–1209, DOI 10.1039/b924814e.

[155] E. A. Caspary, R. A. Kekwick, *Biochemical Journal* **1957**, *67*, 41–48, https://www.ncbi.nlm.nih.gov/pmc/articles/PMC1200105/.

[156] D. A. D. Parry, J. M. Squire in *Advances in Protein Chemistry*, *Vol. 70*, (Eds.: F. Richards, D. Eisenberg, J. Kuriyan), Elsevier Academic Press, **2005**.

[157] J. Kim, G. A. Somorjai, *Journal of the American Chemical Society* **2003**, *125*, 3150–3158, DOI 10.1021/ja028987n.

[158] G. Marx, X. Mou, A. Hotovely-Salomon, L. Levdansky, E. Gaberman, D. Belenky, R. Gorodetsky, *Journal of Biomedical Materials Research Part B: Applied Biomaterials* **2008**, *84B*, 49–57, DOI 10.1002/jbm.b.30842.

[159] Y. Chen, H. Mao, X. Zhang, Y. Gong, N. Zhao, *International Journal of Biological Macromolecules* **1999**, *26*, 129–134, DOI 10.1016/S0141-8130(99)00073-2.

[160] H. Arwin, *Thin Solid Films* **2011**, *519*, 2589–2592, DOI 10.1016/j.tsf.2010.11.082.

[161] S. Tunc, M. F. Maitz, G. Steiner, L. Vázquez, M. T. Pham, R. Salzer, *Colloids and Surfaces B: Biointerfaces* **2005**, *42*, 219–225, DOI 10.1016/j.colsurfb.2005.03.004.

[162] M. L. Clarke, J. Wang, Z. Chen, *Journal of Physical Chemistry B* **2005**, *109*, 22027–22035, DOI 10.1021/jp054456k.

[163] M.-J. Desroches, S. Omanovic, *Physical Chemistry Chemical Physics* **2008**, *10*, 2502–2512, DOI 10.1039/B719371H.

[164] A. Toscano, M. M. Santore, *Langmuir* **2006**, *22*, 2588–2597, DOI 10.1021/la051641g.

[165] E. Bittrich, PhD thesis, Technische Universität Dresden, **2010**, http://www.qucosa.de/fileadmin/data/qucosa/documents/6266/Dissertation-Eva-Bittrich.pdf.

Acknowledgements

First, I would like to express my sincere gratitude and thanks to my supervisor, PD Dr. Karsten Hinrichs for his continuous support of my Ph.D. study. His guidance and patience helped me throughout the long and exhausting experience of my research and writing the thesis. I am truly grateful for the opportunity he has given me and the faith he had in me to get insight into ellipsometry, a technique unknown to me at the beginning of my graduate studies.

I would like to thank Prof. Dr. Norbert Esser for the possibility to conduct my research at ISAS Berlin and for reviewing this work. Thanks also go to Prof. Dr. Klaus Rademann from the chemistry department of Humboldt-Universität zu Berlin, who gratefully agreed to review this thesis as my external consultant.

Many thanks go to the Deutsche Forschungsgemeinschaft (DFG) for financial support and our cooperation partners within the DFG-NSF project: Dr. Petra Uhlmann, Dr. Klaus-Jochen Eichhorn, Dr. Meike König, Dr. Stefan Adam, and Dr. Eva Bittrich from the Leibniz-Institut für Polymerforschung Dresden, Prof. Dr. Igor Luzinov and Dr. Michael Seeber from Clemson University, Prof. Dr. Sergiy Minko, Dr. Oleksandr Trotsenko and Timothy Enright from the University of Georgia, Athens, and Prof. Dr. Marcus Müller and Dr. Fabien Leonforte from the Universität Göttingen. Especially I would like to thank Meike, Stefan, Eva, Michael, and Oleksandr for sample preparation and many interesting discussions, as well as Stefan and Eva for the in situ VIS ellipsometry measurements and valuable insights into understanding the behavior of polymer brushes.

Great thanks go to the In situ IR spectroscopy group at ISAS. Most of all, I would like to thank my roommate and co-mentor, Dr. Andreas Furchner, for introducing me into ellipsometry and the in situ setup as well as endless interesting discussions. His patience and knowledge are truly inspiring and took a great part in making this work possible. Thanks also go to Özgür Savaş, Timur Shaykhutdinov, Christoph Kratz, Dimitra Gkogkou, Kristina Lovrek, and Ilona Engler for a great working atmosphere, helpful discussions, technical support in the laboratory, as well as making lunch and coffee breaks truly enjoyable. At this point I would also like to thank the technical staff and all colleagues at ISAS Berlin for a nice atmosphere.

I deeply thank my family and close friends for support and kindness throughout the entire journey of my studies with all its ups and downs. And last but not least, my deepest thanks go to my beloved running shoes and my crew, the adidas Runners Berlin. Running together through the streets of Berlin, to the beat of good music, always cleared my head in the evenings. I believe I would not have been able to finish this thesis without the refreshing and energized feeling that the exercise gave me.

Declaration of Authorship

I hereby declare that this thesis titled 'Infrared ellipsometry on mixed functional polymer brushes designed to control surface characteristics' and the work presented in it are my own. I confirm that I am the sole author of the present work unless otherwise stated. Where I have consulted the published work of others, this is always clearly attributed. All sources of information have been acknowledged. This thesis or parts of it have not been submitted for a degree or any other qualification at this University or any other institution. I have prepared this thesis for the degree of Dr.rer. nat. between September 2012 and March 2017 under supervision at the Leibniz-Institut für Analytische Wissenschaften – ISAS – e. V. in Berlin.

Signed: _____

Date: _____